Rochester Institute of Technology

RIT Digital Institutional Repository

10-2019

Three Dimensional Digital Alloying with Reactive Metal Inks

Chaitanya G. Mahajan
cgm5952@rit.edu

Follow this and additional works at: https://repository.rit.edu/theses

RIT

Three Dimensional Digital Alloying with Reactive Metal Inks

by

Chaitanya G. Mahajan

A dissertation submitted in partial fulfilment of the requirements for the

degree of Doctor of Philosophy in Engineering

Engineering (PhD Program)

Kate Gleason College of Engineering

Rochester Institute of Technology,

Rochester, New York

October 2019

Three Dimensional Digital Alloying with Reactive Metal Inks

by

Chaitanya G. Mahajan

Committee Approval:

We, the undersigned committee members, certify that we have advised and/or supervised the candidate on the work described in this dissertation. We further certify that we have reviewed the dissertation manuscript and approve it in partial fulfillment of the requirements of the degree of Doctor of Philosophy in Engineering.

Dr. Denis R. Cormier (Advisor)   Date:
Earl W. Brinkman Professor, AMPrint Center Director, Industrial & Systems Engineering

---

Dr. Scott A. Williams   Date:
Professor, School of Chemistry & Materials Science

Dr. Mark E. Irving   Date:
Research Faculty, Industrial & Systems Engineering

Dr. David A. Borkholder   Date:
Bausch & Lomb Professor, Microsystems Engineering

Certified by:

Dr. Edward Hensel   Date:
Director, PhD in Engineering

Abstract

Kate Gleason College of Engineering
Rochester Institute of Technology

Degree: Doctor of Philosophy   **Program:** Engineering PhD
Author: Chaitanya G. Mahajan   **Advisor:** Dr. Denis R. Cormier
Dissertation Title: Three Dimensional Digital Alloying with Reactive Metal Inks

3D printing of multifunctional components using two or more materials is a rapidly growing area of research. Metallic alloy inks have been used with various 3D printing techniques to create functional components such as antennas, inductors, resistors, and biocompatible implants. Most of these printing techniques use premixed metallic alloy inks or nanoalloy particles with a fixed composition to fabricate the functional part. Since the properties of alloys vary with changes in the elemental composition, a printing process which could digitally dispense alloy inks having specific desired compositions would enable different functionalities and be highly desirable.

Using the binary copper-nickel system as an example, the formation of alloy with metal precursor inks is presented. Since copper and nickel both have a face centered cubic (FCC) structure and show complete miscibility in each other, formation of their nanoalloy is, in theory, relatively easy. By printing metal precursor inks rather than nanoparticle suspensions, problems associated with the nanoparticle inks such as ink stability and nozzle clogging can be avoided. Copper and nickel precursor inks were formulated having rheological properties suitable for inkjet printing. Reduction of metal inks was studied under various conditions. The sintered metal and alloy structures were characterized using thermal analysis, infrared spectroscopy, energy-dispersive x-ray spectroscopy (EDS), and x-ray diffraction. Nickel, a ferromagnetic metal, showed novel microstructures such as aligned nanowires and nanowire grids when reduced in the presence of a magnetic field. These microstructures had enhanced anisotropic electrical and magnetic properties along the direction of the nanowire.

The reduction of combined ink solutions (copper and nickel) showed formation of a two phase with copper as one phase and a nickel rich alloy as other. These structures demonstrated no change in electrical resistivity when exposed to an oxidation rich environment. To achieve a homogeneous alloy formation, the copper phase and the nickel rich phase were diffused together at high temperatures. Copper nickel alloy inks with ratios $Cu_{30}Ni_{70}$, $Cu_{50}Ni_{50}$, and $Cu_{70}Ni_{30}$ were formulated and reduced at 230 °C and later high temperature diffusion was achieved at 800 °C. The lattice parameter of the alloy phase for the inks with ratio $Cu_{30}Ni_{70}$ was 3.5533Å, $Cu_{50}Ni50$ was 3.5658 Å, and $Cu_{70}Ni_{30}$ was 3.5921 Å. Using Vegard's law, the composition of the alloy phases for the three samples were estimated to be $Cu_{32}Ni_{68}$, $Cu_{46}Ni_{54}$, and $Cu_{75}Ni_{25}$. This formation of the desired alloy composition can open the door to numerous applications in biomedical and electronics sectors, among others

Acknowledgement

There are several people whose help and support were important in the completion of this dissertation. I would like to express my deepest appreciation to my advisor Dr. Denis Cormier for giving me the opportunity to do my doctoral study under his guidance. I would like to thank him for all the help and advice beyond this dissertation that will be part of my skills set for my future career endeavors. I feel very fortunate to be part of his research lab and learn interesting ideas in the field of additive manufacturing.

I would also like to extend my gratitude to Dr. Scott Williams, Dr. Mark Irving, and Dr. Bruce Kahn for their valuable inputs related to concepts in chemistry and material science. Their deep knowledge in the field both theoretical and experimental was very helpful in the completion of my dissertation. Many thanks to Dr. Borkholder and his research group for all the feedback and encouragement in publishing papers and writing this dissertation.

Additionally, sincere thanks to Dr. Edward Hensel for all his guidance and support throughout the course of my graduate school. I would also like to thank Dr. Surendra Gupta for helping me with material characterization and determining the alloy composition using XRD plots. A special thank you for the faculty of the Industrial & Systems Engineering department for their help and support. I would like to acknowledge the assistance of all the lab members at AMPrint Center, Brinkman lab, Dr. Borkholder's lab and Dr. Scott William's research group.

Finally, I would like to express my gratitude to my parents, sister for their love and support as always. Thank you to my better half Prachi for her love, support, and motivation. This dissertation stands as a testament to your unconditional love and encouragement.

Table of Contents

List of Figures

List of Tables

Chapter 1 Introduction

1.1. Introduction

Digital printing is a technique to provide the output of digital information from an electronic file onto a substrate of some kind [1]. The substrate can be in the form of printing paper, polymer, fabric, or metal. In recent years, researchers have begun to use different digital printing techniques to print functional devices such as actuators, microcontrollers, and sensors which are difficult to fabricate using traditional printing techniques. Conventional pattern-based printing processes such as flexography, gravure, and screen printing involve several steps to create the desired pattern to be printed which increases the production time and cost, particularly in situations where the production volumes are low. In comparison with traditional pattern-based printing techniques, on-demand digital printing techniques involve fewer processing steps, reduced material wastage, and are capable of depositing material onto both planar and non-planar substrates. Some examples of on-demand digital printing involve inkjet printing, aerosol jet printing, and micro-extrusion printing. The printable materials are in the form of inks or pastes which require specific rheology or flow properties to allow printing on different substrates. A wide variety of ceramic, metal, and polymer inks have been used with digital printing techniques. Typical thicknesses of the deposited films range from hundreds of nanometers to a few microns per printing pass. In order to print a part with the desired thickness, multiple layers are printed on top of each other until the thickness is achieved. On-demand digital printing of one or more inks that provide mechanical, thermal, electrical, optical, magnetic, biological or other types of functionalities can be classified as a branch of 3D printing. Different pattern-based and on-demand

digital printing techniques, their advantages, limitations and functional applications are discussed further in Chapter 2.

Metals are suitable for conducting heat and electricity. As a result, they are used in the field of printed electronics to fabricate 2D and 3D conductive structures. The market for printed electronics was valued at $6.8 billion in 2018 and is forecast to reach $13.6 billion by 2023 [2]. Different applications in printed electronics involve wearable devices, smart packaging systems, and healthcare monitoring devices. Digital printing of metal inks on solid and flexible substrates has been demonstrated in the literature. These metal inks are commonly divided into nanoparticle inks or precursor (Metal-Organic Decomposition- MOD) inks. These inks are explained in detail in Chapter 2. Mixing several metal inks together to create a nanoalloy provides an opportunity for tuning the physical and chemical properties at the nanoscale.

A nanoalloy is defined as a nanocluster alloy containing atoms or molecules of two or more metals [3]. Nanoalloys are generally multimetallic nanoparticles fused together to create properties that differ from those of the individual bulk metals. The physical and chemical properties of nanoalloys can be enhanced by varying their composition and particle sizes to provide properties with applications in biomedical, electronics, engineering and catalysis. There are over 80 metallic elements in the periodic table resulting in the potential for more than 3000 possible binary combinations [4]. Elements which are immiscible in the bulk form or have a large miscibility gap can be mixed at the nanoscale to form nanoalloys with properties different from their individual bulk matters [5, 6].

1.2. Theory of nanoalloys

1.2.1. Types of nanoalloys

Nanoalloys can be classified according to the mixing pattern of the metal atoms. The four main types of mixing patterns can be identified as follows:

1.2.1.1. Core-shell nanoalloys:

Core-shell alloys consist of a shell of atoms of one metal surrounding a core of atoms of another metal. Fig. 1-1(a) shows the schematic representation of a core-shell structure. These patterns find their applications in many biomedical devices where the shell can serve as a biocompatible protective layer to the core which may or may not be biocompatible. A wide variety of bimetallic combination of elements such as FeAu [7], AgPd [8], FePt [9, 10], PtAu [11] have been formulated.

1.2.1.2. Subcluster nanoalloys:

Subcluster alloys share an interface or have a small number of atoms at a segregation interface. Fig. 1-1(c) shows a schematic representation of the subcluster alloy structure. Alloys such as AlFe [12], AgNi and AgFe [13] have been fabricated with such a structure.

1.2.1.3. Mixed nanoalloys:

Mixed nanoalloys have either random atomic structure (Fig. 1-1(d)) or ordered atomic structure (Fig. 1-1(e)). The intermixing pattern with random atomic structure is more common than ordered atomic structures. CoAg [14], PdAu [11], AgCu [15], MnAu [16], and CuAg [17] show mixed nanoalloys structures.

1.2.1.4. Multishell nanoalloys:

Multishell nanoalloys have alternating shells of different metals (Fig. 1-1(b)). These types of nanoalloys are observed more in molecular dynamic simulations and are infrequently used experimentally [18, 19]. Alloys of CuAu [19], CuAg [11], PdAg, and NiAg have shown this type of mixing pattern in molecular dynamics simulation [20].

(a)
Core-shell

(b)
Multi-shell

(c)
Subcluster

(d)
Mixed (random)

(e)
Mixed (ordered)
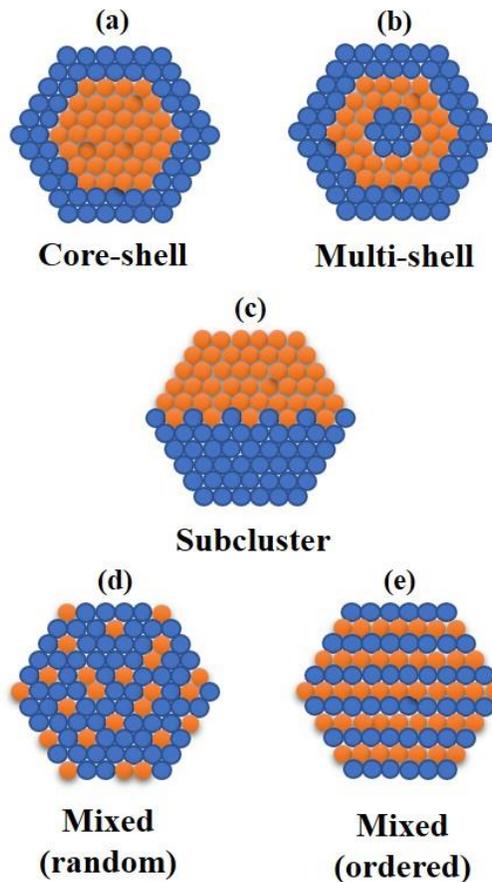
Figure 1-1: Schematic representation of structural patterns (cross section) in nanoalloys. Adapted from [4]

1.2.2. Factors influencing the structure of nanoalloys

For an alloy with elements A and B, the type of nanoalloy structure formed depends upon several factors including the preparation method and experimental procedure. The following list indicates factors that help determine the atomic ordering of the nanoalloy [4].

1. Relative strength of atomic bonding within a metal type (A-A or B-B) as well as between metals (A-B). When the A-B bonds are the strongest, mixing is favored. Otherwise, segregation is preferred with metal atoms having the strongest bond appearing in the center of the core-shell type nanoalloy.

2. Surface energies of bulk elements favor segregation where the element with lowest surface energy tends to separate out at the surface of the cluster.

3. Smaller atomic size elements tend to occupy the core in the core-shell type nanoalloy.

4. Electron transfer from less electronegative elements to more electronegative elements favors mixing.

5. Elements which bind strongly to the ligands tend to get segregated during reduction.

1.2.3. Synthesis of nanoalloy particles

Wide ranges of nanoalloys have been produced using chemical (bottom-up) and physical (top-down) methods. In top-down approaches, bulk metal is broken into nanosized particles whereas in bottom-up approaches, atoms and molecules are assembled to construct the nanoparticles. The main advantage of the top-down approaches is that bulk quantities of nanoparticles can be produced within a short span of time. However, the bottom-up approaches have the advantage of a more homogenous structure with more ordered crystallography within the nanoparticle [21]. Figure 1-2 shows the top-down and bottom-up approaches for the synthesis of nanoparticles.
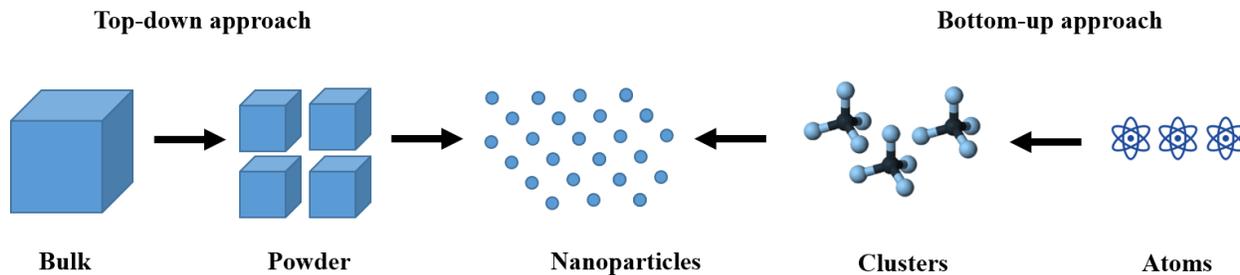
Figure 1-2: Top-down and bottom-up approaches for the synthesis of nanoparticles

Microwave irradiation (MWI) synthesis is one of the bottom-up synthesis techniques used to produce nanoalloys. Metal precursors of the constituent elements that have large microwave absorptions are used as reactants. The absorbed microwave radiation is converted to heat which enhances the reaction rate. This allows rapid decomposition of the precursors to produce alloys of the desired composition. However, this technique requires careful choice of metal precursors with almost identical decomposition profiles to ensure the formation of nanoalloys [3, 22, 23]. Nanoalloys of CuAg [24], CuNi, AuAg, AgCu, and AuCu have been synthesized using MWI technique [25].

Another bottom-up synthesis technique involves reduction of metal salts and mixed metal hydroxide. The metal salts of different elements are dissolved in a solvent along with a capping agent to control the growth of the nanoparticles. A reducing agent is then added to the solution to reduce the mixed metal ions to form nanoparticles. The nanoparticles produced are then extracted from the solution by centrifuging followed by washing and later drying under vacuum [3]. Thermal decomposition of organometallic precursors has been used for creating monometallic nanoparticles as well as nanoalloys. All metal atoms generated from the decomposition of the precursor are transformed into polynuclear clusters where the metallic nanocrystals grow [26]. Nanoalloys of FePt [27] and CoPt [28] have been formulated using this process.

Physical preparation (top-down approach) of nanoalloy particles includes techniques such as gas aggregation source, laser ablation of metal/alloy plate, and ion sputtering. In gas aggregation source, the alloy clusters are formed by vaporizing the bulk metals of different elements and allowing them to aggregate in the presence of an inert cooling gas. A high temperature furnace (> 2000 °C) is used to generate alloys of refractory metals such as Ni, Cu, and Ag [29].

Laser ablation is the most common technique to synthesize nanoalloys. A basic experimental setup for laser ablation includes a laser and target material. A liquid or a carrier gas is used as a medium in which ablation is performed. Alloys of FeAg [6], AgNi and AgFe [13] have been formulated using the laser ablation process. In ion sputtering, alloy particles are produced by bombarding high energy inert gas ions onto the metal target. Ions of Ar^+, Kr^+, and Xe^+ are used with bombardment energies ranging from 10-30 keV [4]. NiTi subcluster nanoalloy has been formulated using this technique [30]. It is generally easier to control the structure of the nanoalloys with bottom-up synthesis techniques than it is with top-down synthesis techniques [26]. If the decomposition profiles are identical, then a well-mixed structure is possible. If the decomposition profiles are different, it is possible to synthesize the core first and then increase the temperature to generate a metallic shell on top of the core.

1.2.4. Characterization of nanoalloys

To characterize and study the properties of these nanoalloys, a wide variety of experimental techniques are used. One technique is Auger electron spectroscopy (AES) in which the alloy composition is determined from the top few layers of the nanoparticle surface. Electron and X-ray diffraction techniques are used to study the structure, crystallinity and lattice spacing. Transmission and scanning electron microscopy (TEM, SEM) are useful for studying the nanoparticle structure as well as the atomic arrangement.

1.2.5. Applications of nanoalloys

1.2.5.1. Biomedical

Nanoalloys with core-shell structures are often used in biomedical applications involving drug delivery and hyperthermia treatment. Hyperthermia is a therapeutic technique used to treat malignant tumors by raising the temperature of a specific region of the body where the tumor is growing. It has been observed that cancer cells are more sensitive to heat than normal cells. An alternating magnetic field is applied to heat up and destroy the tumor [31, 32]. Nanoalloys used in these applications typically have a magnetic element positioned at the core and protective biocompatible elements positioned at the shell [33, 34]. Other alloys such as FePt have been used to detect overdoses of L-ascorbic acid or vitamin C in food, biological fluids, and pharmaceutical products [10]. The CuAg nanoalloy has shown better antibacterial activity in comparison with pure silver [17]. AuCu alloy has been used to fabricate biosensors to detect volatile organic compounds [35]

Most biomedical applications use alloy nanoparticles for *in vivo* and *in vitro* studies. There are very few functional biomedical components made using nanoalloys reported in the literature. Nanoalloys having shape memory effect (SME) will be helpful to fabricate biomedical devices using a wide range of printing techniques. Alloys exhibiting SME are materials which can be formed into one shape before regaining their original shapes when heated. They have many applications in medicine such as self-expandable endovascular and urinary stents, catheters, and retrieval baskets [36]. Nitinol, which is an alloy of nickel and titanium, is an example of a material that exhibits the SME. However, the effect of nanoparticle size on shape memory and biocompatibility is still not well understood [3].

1.2.5.2. Catalysis

Nanoalloys are most commonly used in catalytic reactions because the reactions occur on the surface of the material. The core is not in contact with the reactants. Hence, nanoalloys with core-shell structures are preferred with expensive noble metals such as palladium or platinum at the shell and less expensive metal such as copper or nickel at the core [37, 38]. A classic example of a core shell structure is the use of platinum and palladium elements as shells in automotive catalytic converters to reduce pollutants such as nitrogen oxides, carbon monoxide and hydrocarbon emissions which are termed as unburned fuels [39].

1.2.5.3. Other applications

FeAu nanoalloys have higher magnetic anisotropy than the individual bulk element values and are used in ultrahigh density magnetic recording media applications [40]. In the printed electronics sector, CuAg nanoparticles alloys having Ag shells and Cu cores can be used in printed electronics applications to reduce the cost of the printed ink. Resistivities as low as 8.2 μΩ-cm have been reported in the literature for CuAg nanoalloys [41]. NiZn ferrite nanopowder has been used to increase the inductance of a coil [42].

1.3. Motivation

The printing of functional components using nanoalloy particles is still at a relatively primitive stage. Inks with nanoalloy particles can serve as building blocks to create complex parts for any specific application using a wide range of digital printing techniques. The physical and chemical properties of the nanoalloys can be locally controlled by varying the composition via digital printing methods. An example in which material properties may be tuned by variations in composition can be seen in NiTi shape memory alloys. The shape transformation temperature can be tuned between a range of -30 °C to +80 °C by changing the atomic proportion of nickel from

47% to 51% [43, 44]. Other properties such as hysteresis width and mechanical strength can also be modified through addition of other elements such as copper, iron, silver, and vanadium to the NiTi alloy systems [43, 45].

However, printing of alloy structures requires ink preparation with nanoalloy particles of that specific composition. Synthesis of these nanoalloy particles requires multiple steps which include washing, filtering and drying. This increases the time and cost of synthesizing the nanoalloy particles with desired composition. Therefore, a need exists for tuning the alloy composition *in-situ* while printing a functional part.

Other challenges of 3D printing with nanoalloy particle inks include the problems associated with aggregation of particles, nozzle clogging, and high sintering temperatures. Printing individual metal solution inks that are mixed *in-situ* during printing to create a specific alloy composition will improve the time of printing and reduce some of the problems encountered with particle based inks.

1.4. Structure of dissertation

This chapter focuses on different types of nanoalloy particles, factors influencing the structure of the nanoalloy particles, different synthesizing techniques, and their applications. The motivation for changing the alloy composition on the fly while printing a functional part is also presented. The remainder of this document is organized as follows. Chapter 2 describes different types of metal inks, and different printing and post-processing techniques used to fabricate a functional part. Chapter 2 also highlights some of the research related to 3D printing of functional alloy inks and different combinatorial material synthesis techniques. Chapter 3 describes the formulation and characterization of copper and nickel ink. A feasibility study to produce CuNi

nanoalloy film is also presented in this chapter. Chapter 4 highlights the results of printing and sintering techniques to achieve an alloy of the desired ratio. Chapter 5 describes the reduction of nickel ink in the presence of a magnetic field to achieve enhanced electrical and magnetic properties. A summary of the research with key contributions and future directions are presented in Chapter 6.

1.5. References

[1]   N. Jeffrey, *Digital Printing: A Guide to the New World of Graphic Communications*. Micro Publishing Press, Inc., 1996.

[2]   marketsandmarkets.com. "Printed electronics Market by Material (Inks and Substrates), Technology (Inkjet, Screen, Gravure, and Flexographic), Device (Sensors, Displays, Batteries, RFID tags, Lighting solutions/panels, and PV Cells), Industry, and Geography - Global Forecast to 2023." https://www.marketsandmarkets.com/Market-Reports/printed-electronics-market-197.html (accessed.

[3]   F. Calvo, *Nanoalloys: from fundamentals to emergent applications*. Newnes, 2013.

[4]   R. Ferrando, J. Jellinek, and R. L. Johnston, "Nanoalloys: from theory to applications of alloy clusters and nanoparticles," *Chemical reviews,* vol. 108, no. 3, pp. 845-910, 2008.

[5]   Z. Peng and H. Yang, "Ag–Pt alloy nanoparticles with the compositions in the miscibility gap," *Journal of Solid State Chemistry,* vol. 181, no. 7, pp. 1546-1551, 2008.

[6]   M. P. Andrews and S. C. O'Brien, "Gas-phase" molecular alloys" of bulk immiscible elements: iron-silver (FexAgy)," *The Journal of Physical Chemistry,* vol. 96, no. 21, pp. 8233-8241, 1992.

[7]   J. Zhang *et al.*, "Laser-assisted synthesis of superparamagnetic Fe@ Au core– shell nanoparticles," *The Journal of Physical Chemistry B,* vol. 110, no. 14, pp. 7122-7128, 2006.

[8]   J. He, I. Ichinose, T. Kunitake, A. Nakao, Y. Shiraishi, and N. Toshima, "Facile Fabrication of Ag– Pd Bimetallic Nanoparticles in Ultrathin TiO2-Gel Films: Nanoparticle Morphology and Catalytic Activity," *Journal of the American Chemical Society,* vol. 125, no. 36, pp. 11034-11040, 2003.

[9]   S. Sun, C. B. Murray, D. Weller, L. Folks, and A. Moser, "Monodisperse FePt nanoparticles and ferromagnetic FePt nanocrystal superlattices," *science,* vol. 287, no. 5460, pp. 1989-1992, 2000.

[10]   N. Moghimi and K. Leung, "FePt alloy nanoparticles for biosensing: enhancement of vitamin C sensor performance and selectivity by nanoalloying," *Analytical chemistry,* vol. 85, no. 12, pp. 5974-5980, 2013.

[11]   M. M. Mariscal, S. A. Dassie, and E. P. Leiva, "Collision as a way of forming bimetallic nanoclusters of various structures and chemical compositions," *The Journal of chemical physics,* vol. 123, no. 18, p. 184505, 2005.

[12]   Z. Jiao *et al.*, "Nanostructure evolution in joining of Al and Fe nanoparticles with femtosecond laser irradiation," *Journal of Applied Physics,* vol. 115, no. 13, p. 134305, 2014.

[13]   Z. Jiao, M. Sivayoganathan, W. W. Duley, P. He, and Y. N. Zhou, "Formation and characterization of femtosecond-laser-induced subcluster segregated nanoalloys," *The Journal of Physical Chemistry C,* vol. 118, no. 42, pp. 24746-24751, 2014.

[14]   Z. Yang, J. Wei, and M.-P. Pileni, "Metal–Metal binary nanoparticle superlattices: a case study of mixing Co and Ag nanoparticles," *Chemistry of Materials,* vol. 27, no. 6, pp. 2152-2157, 2015.

[15]   E. Choi, S. Lee, and Y. Piao, "A solventless mix–bake–wash approach to the facile controlled synthesis of core–shell and alloy Ag–Cu bimetallic nanoparticles," *CrystEngComm,* vol. 17, no. 31, pp. 5940-5946, 2015.

[16]   X. Wei *et al.*, "Structural and magnetic evolution of bimetallic MnAu clusters driven by asymmetric atomic migration," *Nano letters,* vol. 14, no. 3, pp. 1362-1368, 2014.

[17]   M. Taner, N. Sayar, I. G. Yulug, and S. Suzer, "Synthesis, characterization and antibacterial investigation of silver–copper nanoalloys," *Journal of Materials Chemistry,* vol. 21, no. 35, pp. 13150-13154, 2011.

[18]   D. Ferrer, A. Torres-Castro, X. Gao, S. Sepulveda-Guzman, U. Ortiz-Mendez, and M. Jose-Yacaman, "Three-layer core/shell structure in Au− Pd bimetallic nanoparticles," *Nano letters,* vol. 7, no. 6, pp. 1701-1705, 2007.

[19]   D. Cheng, S. Huang, and W. Wang, "Thermal behavior of core-shell and three-shell layered clusters: melting of Cu 1 Au 54 and Cu 12 Au 43," *Physical Review B,* vol. 74, no. 6, p. 064117, 2006.

[20]   F. Baletto, C. Mottet, and R. Ferrando, "Growth of three-shell onionlike bimetallic nanoparticles," *Physical review letters,* vol. 90, no. 13, p. 135504, 2003.

[21]   V. Pareek, A. Bhargava, R. Gupta, N. Jain, and J. Panwar, "Synthesis and applications of noble metal nanoparticles: a review," *Advanced Science, Engineering and Medicine,* vol. 9, no. 7, pp. 527-544, 2017.

[22]   D. L. Boxall and C. Lukehart, "Rapid synthesis of Pt or Pd/carbon nanocomposites using microwave irradiation," *Chemistry of materials,* vol. 13, no. 3, pp. 806-810, 2001.

[23]   T. Yamauchi *et al.*, "Magnetic Cu–Ni (core–shell) nanoparticles in a one-pot reaction under microwave irradiation," *Nanoscale,* vol. 2, no. 4, pp. 515-523, 2010.

[24]   M. Valodkar, S. Modi, A. Pal, and S. Thakore, "Synthesis and anti-bacterial activity of Cu, Ag and Cu–Ag alloy nanoparticles: a green approach," *Materials Research Bulletin,* vol. 46, no. 3, pp. 384-389, 2011.

[25]   V. Abdelsayed, A. Aljarash, M. S. El-Shall, Z. A. Al Othman, and A. H. Alghamdi, "Microwave synthesis of bimetallic nanoalloys and CO oxidation on ceria-supported nanoalloys," *Chemistry of Materials,* vol. 21, no. 13, pp. 2825-2834, 2009.

[26]   D. Alloyeau, C. Mottet, and C. Ricolleau, *Nanoalloys: Synthesis, Structure and Properties*. Springer Science & Business Media, 2012.

[27]   S. Sun, "Recent advances in chemical synthesis, self-assembly, and applications of FePt nanoparticles," *Advanced Materials,* vol. 18, no. 4, pp. 393-403, 2006.

[28]   J. Park, J. Joo, S. G. Kwon, Y. Jang, and T. Hyeon, "Synthesis of monodisperse spherical nanocrystals," *Angewandte Chemie International Edition,* vol. 46, no. 25, pp. 4630-4660, 2007.

[29]   S. Riley, E. Parks, C. Mao, L. Pobo, and S. Wexler, "Generation of continuous beams of refractory metal clusters," *The Journal of Physical Chemistry,* vol. 86, no. 20, pp. 3911-3913, 1982.

[30]   S. Petrović *et al.*, "Formation of intermetallic phase in Ni/Ti multilayer structure by ion implantation and thermal annealing," *Intermetallics,* vol. 25, pp. 27-33, 2012.

[31] R. Gilchrist, R. Medal, W. D. Shorey, R. C. Hanselman, J. C. Parrott, and C. B. Taylor, "Selective inductive heating of lymph nodes," *Annals of surgery,* vol. 146, no. 4, p. 596, 1957.

[32] R. Gilchrist, W. Shorey, R. C. Hanselman, F. A. DePeyster, J. Yang, and R. Medal, "Effects of electromagnetic heating on internal viscera a preliminary to the treatment of human tumors," *Annals of surgery,* vol. 161, no. 6, p. 890, 1965.

[33] T. L. Kline, Y.-H. Xu, Y. Jing, and J.-P. Wang, "Biocompatible high-moment FeCo-Au magnetic nanoparticles for magnetic hyperthermia treatment optimization," *Journal of Magnetism and Magnetic Materials,* vol. 321, no. 10, pp. 1525-1528, 2009.

[34] S. A. Shah, A. Majeed, K. Rashid, and S.-U. Awan, "PEG-coated folic acid-modified superparamagnetic MnFe 2 O 4 nanoparticles for hyperthermia therapy and drug delivery," *Materials Chemistry and Physics,* vol. 138, no. 2, pp. 703-708, 2013.

[35] W. Zhao *et al.*, "Nanoalloy Printed and Pulse-Laser Sintered Flexible Sensor Devices with Enhanced Stability and Materials Compatibility," *ACS nano,* vol. 9, no. 6, pp. 6168-6177, 2015.

[36] T. Duerig, A. Pelton, and D. Stöckel, "An overview of nitinol medical applications," *Materials Science and Engineering: A,* vol. 273, pp. 149-160, 1999.

[37] S. U. Son *et al.*, "Designed synthesis of atom-economical Pd/Ni bimetallic nanoparticle-based catalysts for sonogashira coupling reactions," *J. Am. Chem. Soc,* vol. 126, no. 16, pp. 5026-5027, 2004.

[38] C. I. Odenbrand, J. Blanco, P. Avila, and C. Knapp, "Lean NO x reduction in real diesel exhaust with copper and platinum titania based monolithic catalysts," *Applied Catalysis B: Environmental,* vol. 23, no. 1, pp. 37-44, 1999.

[39] M. Palacios, M. Moldovan, and M. Gomez, "The automobile catalyst as an important source of PGE in the environment," in *Anthropogenic Platinum-Group Element Emissions*: Springer, 2000, pp. 3-14.

[40] P. Paulus, H. Bönnemann, A. Van der Kraan, F. Luis, J. Sinzig, and L. De Jongh, "Magnetic properties of nanosized transition metal colloids: the influence of noble metal coating," *The European Physical Journal D-Atomic, Molecular, Optical and Plasma Physics,* vol. 9, no. 1, pp. 501-504, 1999.

[41] C. K. Kim, G.-J. Lee, M. K. Lee, and C. K. Rhee, "A novel method to prepare Cu@ Ag core–shell nanoparticles for printed flexible electronics," *Powder Technology,* vol. 263, pp. 1-6, 2014.

[42] B. J. Kang, C. K. Lee, and J. H. Oh, "All-inkjet-printed electrical components and circuit fabrication on a plastic substrate," *Microelectronic Engineering,* vol. 97, pp. 251-254, 2012.

[43] J. G. Fuentes, P. Gumpel, and J. Strittmatter, "Phase change behavior of nitinol shape memory alloys," *Advanced engineering materials,* vol. 4, no. 7, pp. 437-452, 2002.

[44] "Pocket Dentistry. Chapter 28: More Metals." https://pocketdentistry.com/28-more-metals/ (accessed.

[45] M. Zarinejad and Y. Liu, "Dependence of Transformation Temperatures of NiTi-based Shape-Memory Alloys on the Number and Concentration of Valence Electrons," *Advanced Functional Materials,* vol. 18, no. 18, pp. 2789-2794, 2008.

Chapter 2 Literature Review

2.1. Introduction

This chapter focuses on different types of metal and alloy inks which are typically used to fabricate 2D and 3D structures. These inks are dispensed using a wide variety of printing techniques onto a substrate and are later sintered or cured to attain the desired functionality. In recent years, alloy inks with different elemental compositions have been used to provide functions such as electrical conductivity, electrical resistivity, and biocompatibility. The alloy composition and printing techniques used to create the functional components are highlighted below.

2.2. Types of metal inks

Metal inks used in functional printing are broadly categorized as being either nanoparticle (NP) metal ink suspensions or metal organic decomposition (MOD) precursor inks. The nanoparticles in the NP metal ink can be synthesized using top-down or bottom-up approaches as highlighted in Chapter 1. The MOD precursor inks produce nanoparticles directly onto a substrate using a bottom-up approach. The printing inks principally consist of an active material, a carrier solvent, vehicles, and additives. The active material for the nanoparticle inks consists of metal nanoparticles suspended in the carrier solvent. In the MOD precursor inks, the active material is an organic salt dissolved in the carrier solvent. The vehicle in both forms of the inks are the binder agents which improve the adhesion between the inks and the substrate. Additives such as surfactants are added to modify the surface tension of the ink, whereas dispersants are added to avoid agglomeration of the nanoparticles in the carrier solvent. To get rid of the carrier solvent, the printed pattern is thermally sintered to form a metallic layer. Figure 2-1 shows the schematic overview of different approaches to form a metallic layer on a substrate.

17
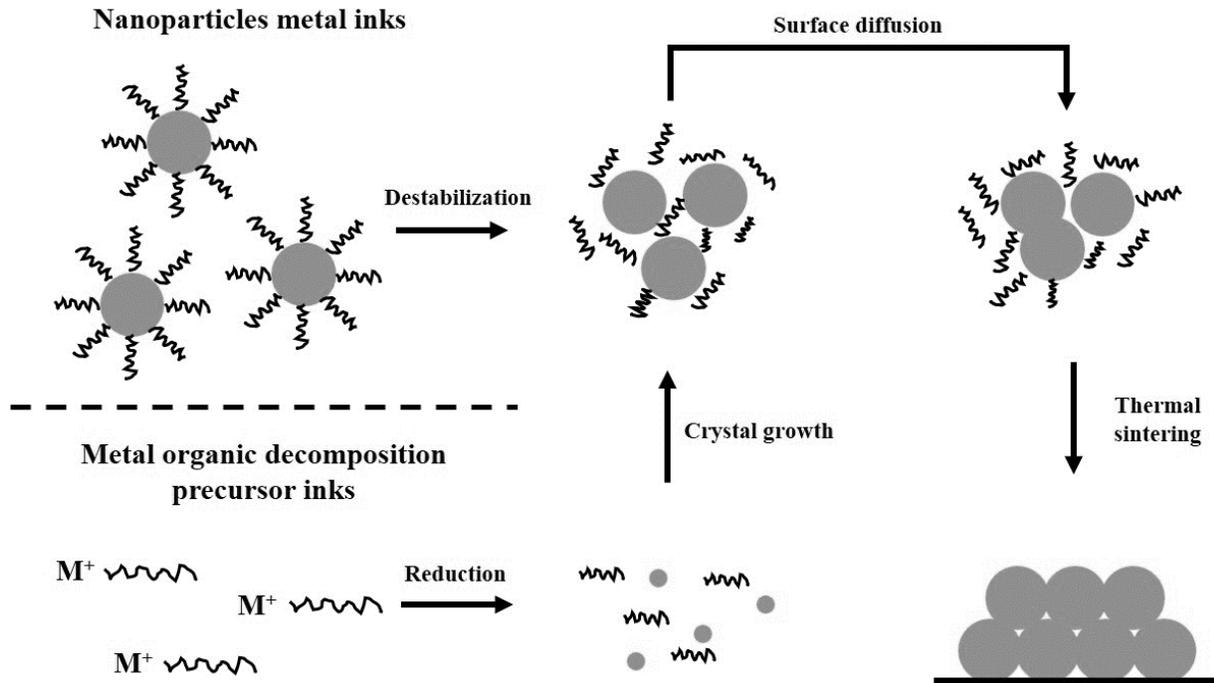
Figure 2-1: Schematic overview of different approaches to form a metallic structure onto a substrate. Adapted from [1]

2.2.1. Nanoparticle metal inks

Nanoparticle metal inks are extensively used in the electronic and biomedical industries. In these inks, metal nanoparticles are typically coated with either low molecular weight carboxyl, amines, or polymers. The coating helps to stabilize the particles in the carrier solvent. The coating is removed in the sintering stage to allow for metal-metal contact between the particles. Nanoparticle metal inks of copper [2-8], nickel [9] and silver [10-14] have been used to provide the conductive function in printed electronics. The stability of nanoparticle inks is affected by factors such as agglomeration of the particles and evaporation of the carrier solvent. The nanoparticles tend to agglomerate over time which affects the printing parameters and causes uneven distribution of the material on the substrate. Evaporation of carrier solvent while printing

or during storage may lead to a change in the solid loading content which alters the ink rheological properties [15].

2.2.2. MOD precursor inks

MOD precursor inks are formulated by dissolving an organic metal salt in an appropriate solvent to form a homogeneous solution. The homogenous solution is used as the ink and is dispensed using a suitable printing technique. Other additives and film forming agents are added to the solution to improve the printability and film forming onto the substrate. In the solution, the metal ions accept an electron pair from a ligand to form metal coordinate complex ions. The metal complex is reduced to form nanoparticles and eventually a conductive film using a suitable sintering technique. MOD precursor inks of metals such as copper [16-24], gold [25], nickel [26] and silver [25, 27-30] have been formulated. Formation of AuAg nanoalloy MOD precursor inks has also been reported in the literature [25]. The stability problems observed in the nanoparticle inks are lessened in the MOD precursor inks because the ink is a homogenous solution. However, the solid loading content for the MOD precursor inks is typically less than that of the nanoparticle inks. For instance, Rosen et al. formulated a copper precursor ink with a loading of 5.2 wt % [21]. This is compared with a copper nanoparticle ink formulated by Fan et al. with a loading of 35.15 wt % [31].

2.3. Printing processes

A wide variety of printing techniques may be used to deposit functional inks onto the desired substrate. These techniques are divided into two groups: master pattern printing processes, and digital printing processes. In master pattern printing processes, the same pattern is printed over and over via a fixed pattern (e.g. engraved drum, screen, etc.). Typical examples of master pattern printing processes include flexography, gravure, and screen printing. These are generally very high

speed printing processes that are well suited for high volume printing of the same patterns. Digital printing techniques do not use fixed master patterns and are instead able to vary the print pattern within a printing run directly from a digital image file. Although digital printing techniques eliminate the expense and changeover time associated with fixed master patterns, the trade-off is that these processes are not generally as fast. Digital printing processes include inkjet printing, aerosol jet printing, and micro extrusion. Descriptions of the primary printing processes in each category are explained below.

2.3.1. Gravure printing

Gravure printing is preferred where long print runs with very high print quality are required. Figure 2-2 shows a schematic illustration of gravure printing. A gravure cylinder is a critical component on which the image to be printed is engraved. It is generally made from metals such as copper or steel plated with copper. The gravure cylinder consists of recessed cells of varying depth and area on the surface to deliver the desired volume of ink onto the substrate. The surplus ink is scraped from the cylinder using a doctor blade. When the ink in the cells is in contact with the substrate, the surface energy forces on the substrate pull the ink out of the cells. The resolution of the print pattern is dependent on the ink viscosity, cell width and depth ratio and the surface properties of the substrate [32]. A print resolution of 10-75 µm with a wet film thickness of 0.1-5 µm can be obtained using this printing process [33, 34].
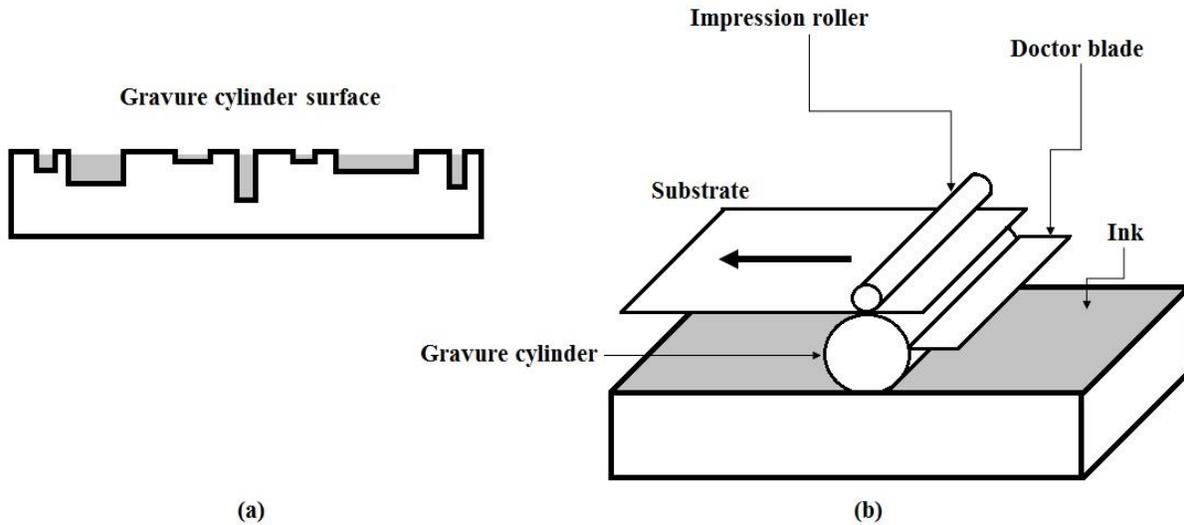
Figure 2-2: The gravure process: (a) cylinder surface with cells; (b) printing unit. Adapted from [35]

Gravure printing has been used for printing functional devices such as antennas [36, 37], capacitors [36], solar cells [38], and OLEDs [39]. Since contact between the substrate and the cells is necessary for ink transfer, the substrate needs to be flat to maintain the pattern fidelity [35]. The ink used for gravure printing should have low viscosity and must dry quickly. If the ink properties change during the printing process, the cells tend to clog thereby affecting the print quality. The cost to make a new cylinder of the desired pattern or to replace the old cylinder after continuous use increases the overall cost of production.

2.3.2. Flexographic printing

Flexographic printing, or flexography, has similarities to gravure printing except that it uses a flexible photopolymer printing plate wrapped around a cylinder. The ink is collected from the ink reservoir by a rubber fountain roller. The ink is later transferred to the anilox roller which is made of metal or ceramic and is engraved with small cells. These cells collect ink from the fountain roller and then transfer ink to the plate cylinder. The amount of ink printed can be controlled by varying the depth of engraved cells on the anilox roller. The substrate is placed

21

between the impression cylinder and plate cylinder. A print resolution of 30-75 µm can be obtained with the print thickness of 0.5-8 µm [33]. Figure 2-3 shows a schematic illustration of the flexography process.
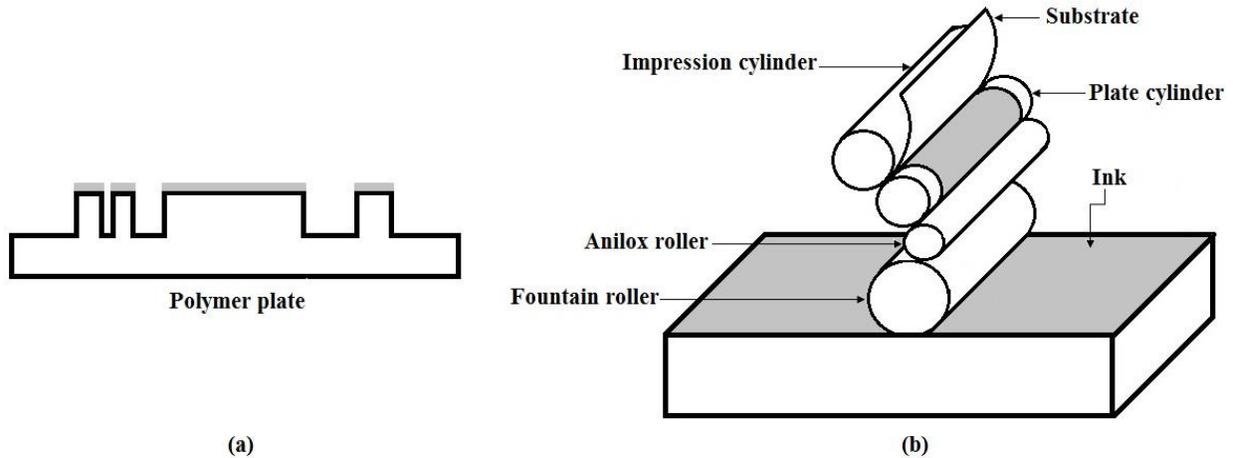
Figure 2-3: The flexography process: (a) flexible polymer/rubber plate; (b) printing unit. Adapted from [35]

Flexography printing has been used to fabricate organic thin film transistors [40] and antennas for RFID tags [41]. The resolution of flexography is restricted by the stiffness of the material from which the polymer plate is fabricated. High stiffness plates have less compression which can sometimes create pinholes in the printed pattern. Low stiffness plates can sometimes lead to over compression of fine features resulting in open lines, overlapped lines, and wavy edges [32, 42].

2.3.3. Screen printing

Screen printing is preferred where thick layers of functional inks need to be deposited on a flat surface. It consists of a screen with the desired patterned mesh. The ink is pushed through the mesh openings using a squeegee and is transferred onto the substrate. Two different types of screen printing units may be used in manufacturing as shown in Figure 2-4 (a-b). Flatbed screen printing

22

is used for small scale production, while rotary screen printing is used in roll to roll manufacturing. A print resolution of 30-100 µm can be obtained with print thicknesses of 3-100 µm [32, 33].
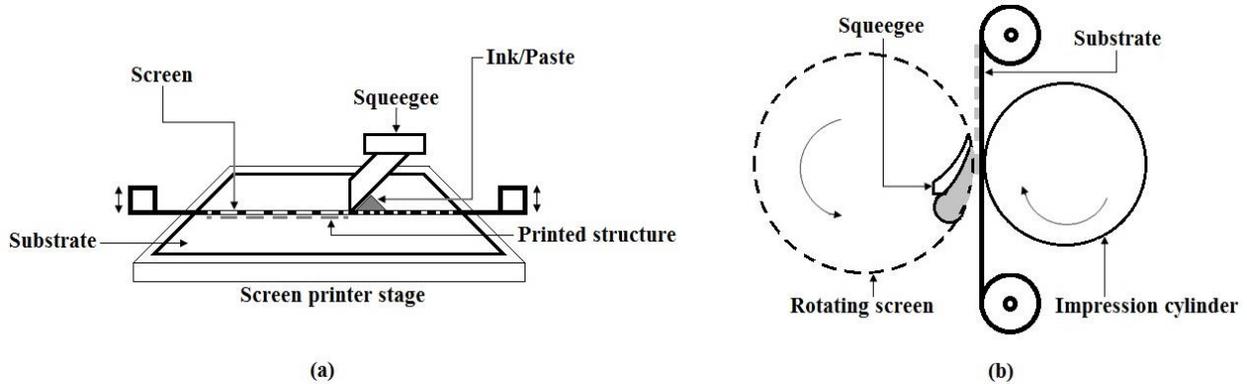
Figure 2-4: Screen printing process (a) flatbed unit; (b) rotary unit. Adapted from [32]

Screen printing has been used to print functional devices such as thin film transistors [43], pressure sensors [44], temperature sensors [45], and organic light emitting devices [46]. The print quality is determined by various factors such as paste viscosity, screen mesh size, speed, angle, geometry of the squeegee, material of the screen and substrate. Small feature sizes require smaller openings in the mesh to print fine features. This limits the amount of ink that can be transferred onto the substrate which affects the print quality [34].

2.3.4. Micro extrusion printing

The micro extrusion printing process is used to print highly viscous functional materials. Narrow lines with high aspect ratios can be printed using this printing technique. The process uses air pressure and a valve mechanism to push the material out of a nozzle. Figure 2-5 shows a schematic illustration of a micro extrusion printing process commercialized by nScrypt. A 3.c.c. syringe is loaded with the functional material to be printed. Air pressure pushes the ink through a ceramic nozzle which controls the size of the extruded material. Nozzle diameters ranging from

12.5 µm to 125 µm are used to extrude material. A valve needle controls the flow of material through the nozzle. When the valve needle is moved down, the seal is opened allowing the ink to flow out of the ceramic nozzle. To stop the flow of material, the valve moves upward which produces negative pressure that sucks the ink back into the nozzle [47]. The minimum line width is approximately 10 times larger than largest particle in the ink, hence line widths between 25 µm and 3000 µm are generally considered feasible [48].
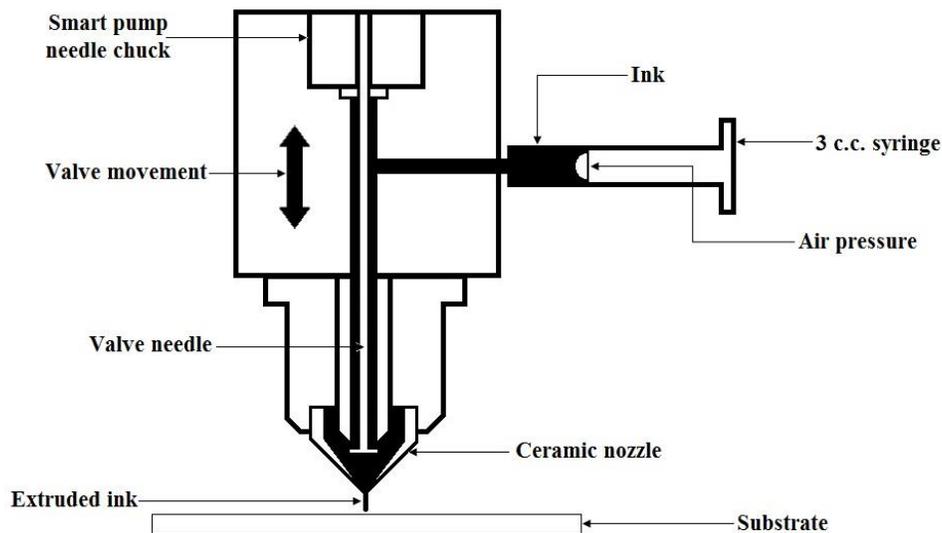
Figure 2-5: nScrypt micro extrusion system. Adapted from [49]

This process has been used to print solid oxide fuel cell materials [49], antennas [50], and strain gauges [51]. This technique is capable of printing functional ink on planar as well on non-planar substrates. Since low viscosity inks can ooze out of the nozzle, printing very low viscosity inks with inkjet or aerosol jet techniques is recommended.

2.3.5. Inkjet printing

Inkjet printing is widely used to print functional materials on planar surfaces. Inkjet printing techniques can be classified as either continuous mode or drop-on-demand (DOD) based

on the form in which liquid ink exits the nozzle. Figure 2-6 shows a schematic illustration of continuous inkjet and DOD inkjet systems. The continuous mode has a steady stream of electrically charged ink droplets which are deflected electrostatically. The electrical potential of a charging electrode induces charge on each drop as it exits the nozzle head. The drop then passes through electric field plates which deflect the charged droplets. Uncharged drops pass into the catcher, allowing them to be recycled. The DOD inkjet system ejects ink drops only when they are required to be printed. The liquid is ejected using thermal or piezoelectric actuation. The thermal actuator DOD inkjet printer creates a short-lived bubble of vapor which pushes the ink droplets out of the nozzle. After the bubbles collapse, the cavity is refilled with ink from the reservoir. Piezoelectric actuated DOD uses a piezoelectric element which changes the internal volume of the ink cavity on the application of electric field and thereby pushes ink from the nozzle. The cavity then refills with ink from the reservoir. Feature sizes obtained using these processes typically range from 20-50 µm with a wet film thickness of 0.3-20 µm [33].
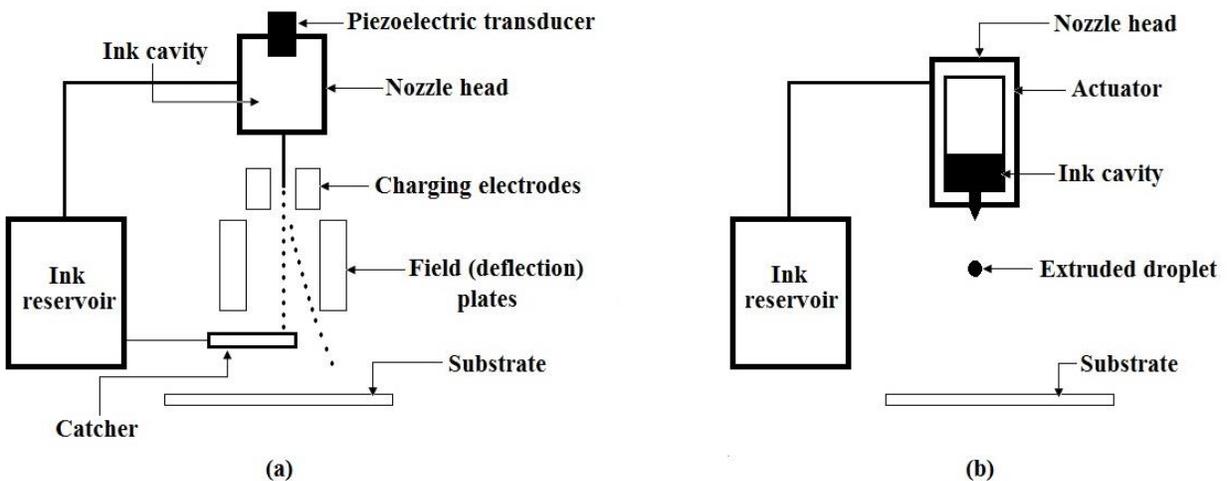
Figure 2-6: Inkjet printing process (a) continuous mode; (b) drop on demand mode. Adapted from [48]

Inkjet printing has been used to fabricate antennas [52], capacitors [36], and resistors [36]. MOD precursor inks of different elements such as silver [53] and copper [22] have been printing using inkjet printing technique. To achieve high throughput, multiple print heads or large numbers of nozzles must be used which increases the risk of nozzle clogging and thereby affecting the print quality. Since inkjet printing is non-contact, the ink fired from the nozzle may tend to miss the target and affect the print dimensions if the droplet trajectory is not perpendicular to the face plate. Uneven drying of the functional ink after printing can also affect print quality for this printing technique. Inkjet printing processes are generally used to print on flat surfaces as printing on non-planar surfaces is difficult and requires complex calculations to compensate for non-uniform droplet travel times to reach the substrate [54].

2.3.6. Aerosol jet printing

Aerosol-Jet printing focusses an aerosol mist of the functional material to be printed onto planar or non-planar surfaces. The functional ink can be atomized using pneumatic or ultrasonic energy to create an aerosol mist. Figure 2-7 shows a schematic illustration of the pneumatic atomizing aerosol jet process. The aerosol jet printing process uses nitrogen gas to atomize ink and to transport the aerosol mist from the atomizer to the deposition head. The deposition head has a sheath gas inlet which surrounds the aerosol stream as it exits the nozzle. Process parameters such as ink flow rate, cup and tube temperature, translation speed, and stand-off distance can be varied to deposit material with desired thickness and height. Feature sizes as small as 5 µm have been achieved using aerosol jet printing [55].
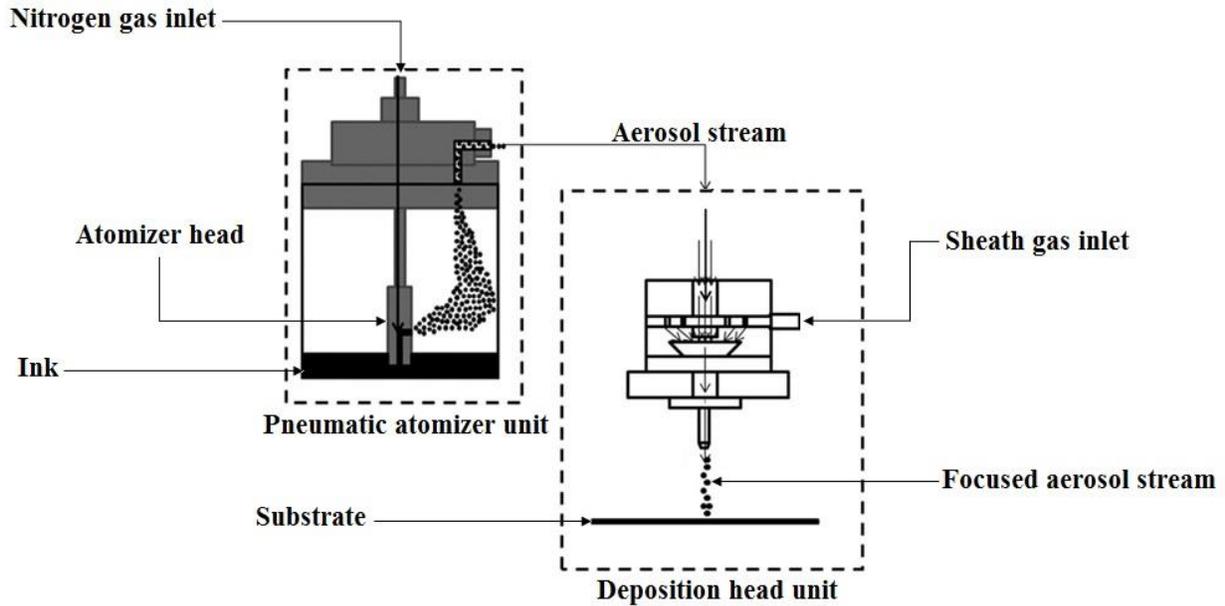
Figure 2-7: Aerosol jet system. Adapted from [56]

Aerosol jet printing has been used to fabricate transistors on flexible polyimide substrates [57], sensors [58, 59], and strain gauges [59]. The main advantage of the aerosol jet process is its capability to print fine features on planar and non-planar surfaces. However, the aerosol mist coming out of the nozzle is carried by a high flow carrier gas (e.g. nitrogen) which fans out as it approaches the substrate. Sub-micron droplets in the aerosol stream can be swept out with the carrier gas, thus generating satellite droplets near the printed features which affects the print quality [60].

As mentioned before, different additives and stabilizing agents are added to the functional inks to facilitate the printing process. These inks often require post processing to remove the additives and create necking between the nanoparticles. Different post processing methods used are discussed in the next section.

2.4. Post processing

Sintering techniques such as thermal [22, 53], plasma [61], and photonic [24, 53] sintering have been used for post processing of printed functional inks. The ink printed on a substrate has a large volume of carrier solvent and much lower volume of functional material. The carrier solvent must be evaporated to initiate sintering. The dynamics of evaporation influence the functionality of the deposited ink as significant shrinkage in the volume can result in cracks developed at the surface of the printed material. Other challenges include removing the capping layer of polymer from the surface of the nanomaterials, breaking down the metal complex to reduce the metals to their elemental forms and ink adhesion to the substrate. Thermal and photonic sintering processes are explained in detail below.

2.4.1. Thermal sintering

Thermal sintering involves heating the printed pattern to an elevated temperature using a hot plate, furnace or vacuum oven. To get rid of additives and other nonfunctional components from the ink, the printed patterns are often sintered at a temperature higher than 200 ℃. This limits the choice of substrate materials since common polymer substrates such as PET has a glass transition temperatures less than 200 ℃. Another major drawback of thermal sintering is the time duration of sintering which is significantly high in comparison with the other sintering methods such as photonic sintering. This complicates its integration with roll to roll manufacturing and requires long complex winding feed paths [62]. Due to these shortcomings, sintering techniques such as photonic sintering are sometimes used.

2.4.2. Photonic sintering

Photonic sintering uses intense pulses of broad spectrum light from ultraviolet to the infrared region (200 nm - 1200 nm). The energy generated with these lamps in each short pulse of light creates extremely high temperature within a micro to millisecond time frame [63]. At these temperatures, evaporation of solvent and other organics along with rapid sintering of the nanoparticles takes place. The high temperature is achieved in a short time frame during which the substrate remains relatively cool. The process parameters need to be carefully adjusted to avoid damaging the printed pattern and underlying polymer. If too much energy is supplied, it can ablate the deposited ink from the substrate. If not enough energy is supplied, it may lead to an unsintered film [64]. Since the sintering of the ink takes place in milliseconds, this process can be integrated with roll to roll manufacturing process.

Alloy inks with different elemental compositions have been used to create functional devices using different printing techniques. Some of the printing process, their advantages and limitations are described below.

2.5. 3D printing of functional alloy inks

Low melting point alloys with high conductivity have been used in the printed electronics industry for a very long time. Gallium (Ga) and indium (In) liquid alloys (GaIn) have moderate conductivity and can be printed at room temperature using 3D printing techniques. Zheng *et al.* [65, 66] printed GaIn alloy using a custom-made micro-extrusion 3D printer. Room-temperature-vulcanization (RTV) silicone rubber was printed as an encapsulation material to maintain functional stability of the alloy ink (Figure 2-8 (A) & 2-8 (B)). Zhang *et al.* [67] demonstrated atomized spraying of GaIn alloy onto a micro machined mask to create printed circuits on various substrates (Figure 2-8 (C)). The ink was atomized to create droplets ranging from 700 nm to 50

μm in diameter. A thin oxide layer on the droplet surfaces improved adhesion to the substrate. A limitation of using GaIn ink includes spontaneous contraction to droplets because of high surface tension [66]. Also, the ink remains liquid at room temperature which may cause leakage and affect the functionality of the device.
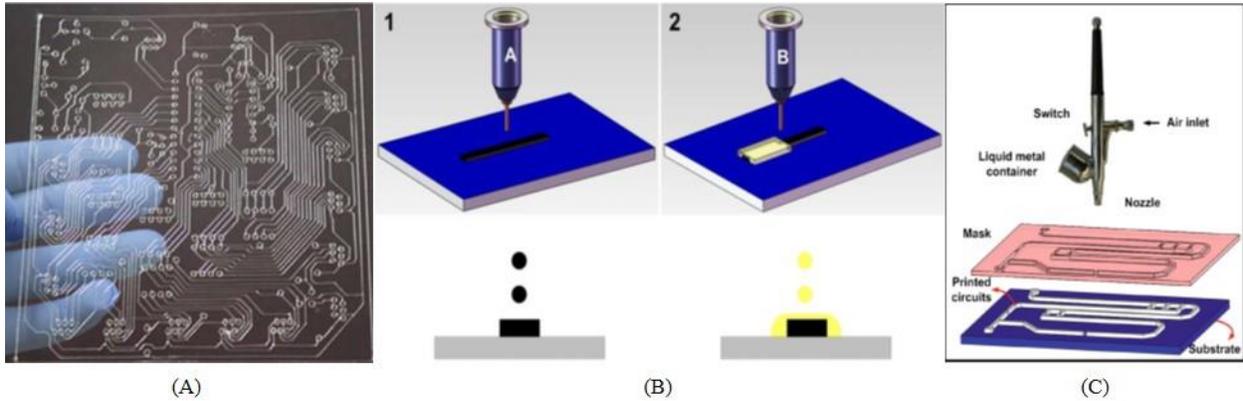
Figure 2-8: (A) Printed conductive circuit using GaIn as functional ink (Used with permission [66]); (B) Step 1: GaIn ink printed on substrate. Step 2: RTV silicone rubber printed as encapsulated material (Used with permission [65]); (C) Schematic illustration of atomized spraying of GaIn ink on mask to create printed circuits (Used with permission [67])

Other options for 3D printing low melting point alloy inks with applications in the healthcare sector have been reported in the literature. Liu et al. [68] created a 3D printer as seen in Figure 2-9 (A) to dispense pure metals or alloys with melting points less than 300 °C. The alloy ink is loaded into a syringe which is wrapped by an aluminum alloy cylinder that is heated via constantan resistance wire. The syringe needle is immersed in cooling fluid such as water or ethanol to avoid oxidation of the ink while dispensing. The same research group demonstrated the use of functional alloy ink in medical electronics [69]. Alloy $Ga_{67}In_{20.5}Sn_{12.5}$ with a melting point of 9.85 °C was used to create electrodes to measure electrocardiography (ECG) signals and impedance for deep brain stimulation. The alloy was injected in gelatin which acted like a

packaging material for the electrode as seen in Figure 2-9 (B). Yi et al. [70] proposed an alloy $Bi_{35}In_{48.6}Sn_{16}Zn_{0.4}$ with a melting point of 57.5°C which could be used as bone cement for fixing total joint arthroplasty as seen in Figure 2-9 (C). The fabrication process is carried out inside a cooling fluid which limits the use of substrate materials.
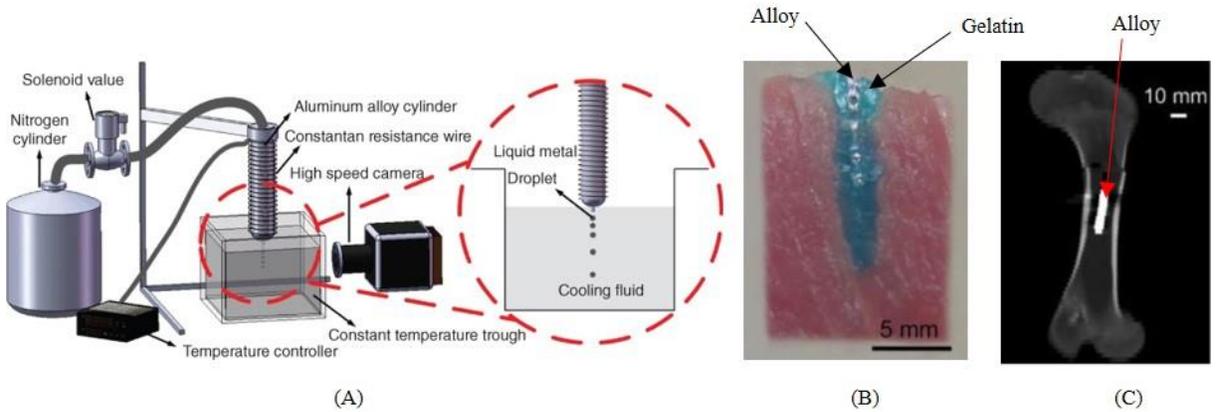
Figure 2-9: (A) Schematic illustration of liquid phase 3D printing (Used with permission [68]); (B) Injectable alloy electrode in porcine tissue (Used with permission [69]); (C) CT scan of porcine femur with alloy cement (Used with permission [70])

A very recent development has been the liquid metal 3D printer by Vader et al. [71]. The solid metal wire is fed into the nozzle chamber where it is melted to form a reservoir of liquid metal. A pulsed magnetic field is applied using the coil surrounding the reservoir to produce magnetohydrodynamic pressure which pushes a droplet of liquid metal out of the nozzle. The ejected liquid droplet lands on the substrate where it solidifies. Alloys of aluminum such as 4043 and 7075 have been printed using this technique [72]. The starting material in this process is in the form of wire with fixed alloy composition.

3D printing of nanoalloys to create functional devices is still in its early stage. Pal et al. [73] formulated a CuNiMn nanoparticle alloy ink which can be sintered under reducing

atmosphere at 800 °C. The ink was made with nanoalloy particles suspended in isopropanol. The ink was dispensed using aerosol jet printing and was used to print conductive structures for printed electronics applications. However, because of the high sintering temperature, this alloy ink is not suitable for use with low melting point substrates. Zhao et al. [74] printed a nanoalloy ink of AuCu on a flexible substrate using a doctor blade printing technique to fabricate a sensor that detects volatile organic compounds. Figure 2-11 shows a schematic representation of the fabrication process. To sinter the ink and form a conductive pattern, a laser is scanned in the desired pattern onto the printed sample. Since the final functional pattern is determined by the sintered area exposed under the laser path, the unsintered ink needs to be cleared from the substrate which increases the cost of fabrication.
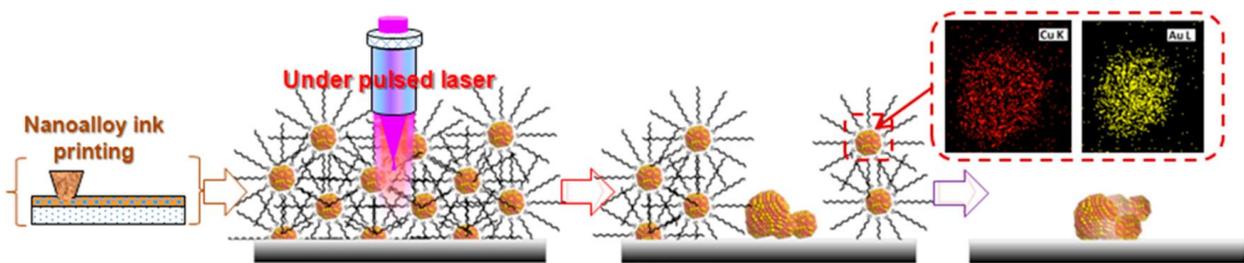
Figure 2-10: Nanoalloy printing followed by pulse laser sintering (Used with permission [74])

The 3D printing techniques of alloy inks highlighted above are capable of printing premixed alloy inks or nanoalloy particles with a fixed composition. However, the creation of functionally graded alloy structures or structures in which the alloy composition is changed on the fly while printing has not been widely explored to date. A printing technique analogous to combinatorial material synthesis would have a number of advantages in controlling the elemental ratio of the final printed alloy part. Printing techniques used in combinatorial material synthesis are highlighted in the following section.

2.6. Combinatorial materials synthesis

Combinatorial materials synthesis is a high throughput synthesis technique that combines a small number of elements or chemical reagents in specific proportions to achieve the desired reaction schemes and to develop a combinatory library of well-defined materials or products [75]. This synthesis technique was highly exploited in the pharmaceutical industry in the early 1990's to make discovery of new drugs faster and more efficient. The traditional method to create combinatorial libraries includes pulsed laser deposition, chemical vapor deposition [76] and multigun sputtering systems [77].

Inkjet printing techniques have also been used to create libraries of mixed oxide catalysts [78], liquid crystals [79], and ferroelectric thin films [80]. The main advantage of inkjet printing over traditional methods is digital control over the small amount of material dispensed. Complete mixing of individual inks is critical to form a compound of desired stoichiometry. The mixing of the individual material takes place either inside a dispensing tool [81, 82] or on the substrate by dispensing individual droplets of each material ink on top of each other [78-80, 83, 84].

Mohebi et al. [81] designed and built a printer to dispense ceramic suspension inks onto a substrate. Figure 2-12 (A) shows a schematic illustration of the printer. The inks are mixed behind the nozzle and printed at precise locations using the XY motion controller. The mixing chamber is a solenoid micropump providing distributive mixing by circulation of the inks.
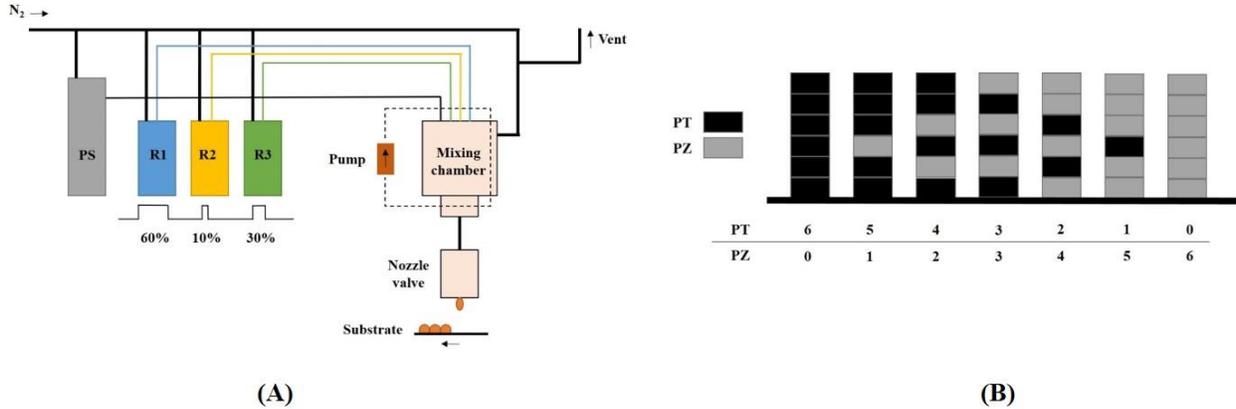
Figure 2-11 (A) Schematic illustration printer where printing ceramic inks are mixed before printing (Used with permission [81]) (B) Mixing producer for formation of PZT thin films with different Ti/Zr ratio (Used with permission [80])

Figure 2-12 (B) shows the mixing procedure reported by Okamura et al. [80] to fabricate lead zirconate titanate (PZT) thin films with different Zr/Ti ratios. Alcohol sol gel precursor solutions of PT and PZ were used as the inks. A similar mixing technique was reported by Reichenbach et al. [83] and Murray et al. [84]. Reichenbach et al. [78] generated combinatorial libraries of complex metal oxide catalyst by dispensing metal precursor solutions using inkjet printheads in a stainless steel microwell plate. Murray el al. [84] used inkjet printing to dispense and allow *in situ* mixing of colloidal suspension of nonoaluminum and nanocopper oxide to create thermite on a flexible substrate.

Most of the research related to combinatorial material synthesis using inkjet printing focuses on creating libraries by printing dots on a substrate or printing in microwell/microtiter plates. The challenges in printing a functional part directly onto a substrate includes poor print quality due to overlapping print regions [80] and the removal of byproducts during synthesis [85]. However, combinatorial material synthesize shows some potential in creating a functional alloy by controlling its elemental composition of individual metal inks. The research needs to generate

34

a functional part with desired alloy composition by printing metal inks are described in the next section.

2.7. Research needs

A review of some of the different types of metal inks, different printing processes, and different sintering techniques along with the recent progress in printing functional alloy ink have been highlighted in this chapter. Most of these printing techniques use premixed alloy inks or nanoalloy particles with a fixed composition to fabricate a functional part. The current printing processes are not capable of printing different alloy composition within the printed part. Combinatorial material synthesis shows potential in mixing individual inks, but the research is more focused on creating mixed metal oxides with different stoichiometric ratios instead of creating metallic alloys with specific compositions.

Since the properties of an alloy change as a function of elemental composition, a printing process which could dispense alloy inks with specific compositions to provide desired functions is required. 3D printing has evolved from a single material approaches to include multi-material deposition techniques. This enables creation of multi-material parts in which each material can serve a different function. Printing individual metal inks in desired proportions to form an alloy with selective composition will help in printing multifunctional components without changing the functional ink every time. This will also improve the time of printing and reduce the overall cost of the fabrication.

Inkjet printing shows potential for dispensing more than one ink at a time. The print time with multi nozzle inkjet is relatively low compared with single nozzle dispensing techniques. Despite the large body of work on printing metallic inks with inkjet printing, mixing two or more

elemental inks to form an alloy has not been well explored. An extensive study is required, in order to understand the degree of mixing following jetting of individual metal inks from different nozzles. Printing and sintering strategies could be developed to produce alloys having desired compositions. This printing and sintering of the desired composition of alloy ink can open the door to different applications in biomedical, electronics and other sectors. The next chapter focuses on the research approach to form digital nanoalloys by mixing individual metal inks in desired proportions.

2.8. References

[1] I. Reinhold, "Inkjet Printing of Functional Materials and Post-Processing," *Nanomaterials for 2D and 3D Printing,* 2017.

[2] D. Deng, Y. Jin, Y. Cheng, T. Qi, and F. Xiao, "Copper nanoparticles: aqueous phase synthesis and conductive films fabrication at low sintering temperature," *ACS applied materials & interfaces,* vol. 5, no. 9, pp. 3839-3846, 2013.

[3] S.-J. Joo, H.-J. Hwang, and H.-S. Kim, "Highly conductive copper nano/microparticles ink via flash light sintering for printed electronics," *Nanotechnology,* vol. 25, no. 26, p. 265601, 2014.

[4] T. Öhlund, A. K. Schuppert, M. Hummelgård, J. Bäckström, H.-E. Nilsson, and H. k. Olin, "Inkjet Fabrication of Copper Patterns for Flexible Electronics: Using Paper with Active Precoatings," *ACS applied materials & interfaces,* vol. 7, no. 33, pp. 18273-18282, 2015.

[5] H.-S. Kim, S. R. Dhage, D.-E. Shim, and H. T. Hahn, "Intense pulsed light sintering of copper nanoink for printed electronics," *Applied Physics A,* vol. 97, no. 4, pp. 791-798, 2009.

[6]   Y.-T. Hwang, W.-H. Chung, Y.-R. Jang, and H.-S. Kim, "Intensive Plasmonic Flash

Light Sintering of Copper Nanoinks Using a Band-Pass Light Filter for Highly

Electrically Conductive Electrodes in Printed Electronics," *ACS applied materials &*

interfaces, vol. 8, no. 13, pp. 8591-8599, 2016.

[7]   Y. Lee, J.-r. Choi, K. J. Lee, N. E. Stott, and D. Kim, "Large-scale synthesis of copper

nanoparticles by chemically controlled reduction for applications of inkjet-printed

electronics," *Nanotechnology,* vol. 19, no. 41, p. 415604, 2008.

[8]   C. Paquet *et al.*, "Photosintering and electrical performance of CuO nanoparticle inks,"

Organic Electronics, vol. 15, no. 8, pp. 1836-1842, 2014.

[9]   S.-H. Park and H.-S. Kim, "Flash light sintering of nickel nanoparticles for printed

electronics," *Thin Solid Films,* vol. 550, pp. 575-581, 2014.

[10]   Y. Li, Y. Wu, and B. S. Ong, "Facile synthesis of silver nanoparticles useful for

fabrication of high-conductivity elements for printed electronics," *Journal of the*

American Chemical Society, vol. 127, no. 10, pp. 3266-3267, 2005.

[11]   H.-H. Lee, K.-S. Chou, and K.-C. Huang, "Inkjet printing of nanosized silver colloids,"

Nanotechnology, vol. 16, no. 10, p. 2436, 2005.

[12]   Z. Zhang, X. Zhang, Z. Xin, M. Deng, Y. Wen, and Y. Song, "Synthesis of monodisperse

silver nanoparticles for ink-jet printed flexible electronics," *Nanotechnology,* vol. 22, no.

42, p. 425601, 2011.

[13]   C. Chen *et al.*, "Using nanoparticles as direct-injection printing ink to fabricate

conductive silver features on a transparent flexible PET substrate at room temperature,"

Acta Materialia, vol. 60, no. 16, pp. 5914-5924, 2012.

[14]   S. Jeong, H. C. Song, W. W. Lee, Y. Choi, S. S. Lee, and B.-H. Ryu, "Combined role of well-dispersed aqueous Ag ink and the molecular adhesive layer in inkjet printing the narrow and highly conductive Ag features on a glass substrate," *The Journal of Physical Chemistry C,* vol. 114, no. 50, pp. 22277-22283, 2010.

[15]   A. Wadhwa, D. Cormier, and S. Williams, "Improving run-time stability with aerosol jet printing using a solvent add-back bubbler," *Journal of Print and Media Technology Research,* vol. 5, no. 3, pp. 207-214, 2016-09-10 2016, doi: 10.14622/JPMTR-1610.

[16]   D.-H. Shin *et al.*, "A self-reducible and alcohol-soluble copper-based metal–organic decomposition ink for printed electronics," *ACS applied materials & interfaces,* vol. 6, no. 5, pp. 3312-3319, 2014.

[17]   S. J. Kim, J. Lee, Y.-H. Choi, D.-H. Yeon, and Y. Byun, "Effect of copper concentration in printable copper inks on film fabrication," *Thin Solid Films,* vol. 520, no. 7, pp. 2731-2734, 2012.

[18]   Y.-H. Choi and S.-H. Hong, "Effect of the Amine Concentration on Phase Evolution and Densification in Printed Films Using Cu (II) Complex Ink," *Langmuir,* vol. 31, no. 29, pp. 8101-8110, 2015.

[19]   A. Yabuki and S. Tanaka, "Electrically conductive copper film prepared at low temperature by thermal decomposition of copper amine complexes with various amines," *Materials Research Bulletin,* vol. 47, no. 12, pp. 4107-4111, 2012.

[20]   W.-d. Yang, C.-h. Wang, V. Arrighi, C.-y. Liu, and D. Watson, "Microstructure and electrical property of copper films on a flexible substrate formed by an organic ink with 9.6% of Cu content," *Journal of Materials Science: Materials in Electronics,* vol. 26, no. 11, pp. 8973-8982, 2015.

[21] Y. Rosen, M. Grouchko, and S. Magdassi, "Printing a Self-Reducing Copper Precursor on 2D and 3D Objects to Yield Copper Patterns with 50% Copper's Bulk Conductivity," *Advanced Materials Interfaces,* vol. 2, no. 3, 2015.

[22] Y. Farraj, M. Grouchko, and S. Magdassi, "Self-reduction of a copper complex MOD ink for inkjet printing conductive patterns on plastics," *Chemical Communications,* vol. 51, no. 9, pp. 1587-1590, 2015.

[23] B.-Y. Wang, T.-H. Yoo, Y.-W. Song, D.-S. Lim, and Y.-J. Oh, "Cu ion ink for a flexible substrate and highly conductive patterning by intensive pulsed light sintering," *ACS applied materials & interfaces,* vol. 5, no. 10, pp. 4113-4119, 2013.

[24] T. Araki *et al.*, "Cu salt ink formulation for printed electronics using photonic sintering," *Langmuir,* vol. 29, no. 35, pp. 11192-11197, 2013.

[25] R. D. McCullough, J. Belot, and R. Potash, "Metal alloys from molecular inks," ed: Google Patents, 2016.

[26] D. S. Ginley, C. J. Curtis, A. Miedaner, M. F. A. M. Van Hest, and T. Kaydanova, "Metal inks," ed: Google Patents, 2014.

[27] Y. Dong, X. Li, S. Liu, Q. Zhu, J.-G. Li, and X. Sun, "Facile synthesis of high silver content MOD ink by using silver oxalate precursor for inkjet printing applications," *Thin Solid Films,* vol. 589, pp. 381-387, 2015.

[28] S. B. Walker and J. A. Lewis, "Reactive silver inks for patterning high-conductivity features at mild temperatures," *Journal of the American Chemical Society,* vol. 134, no. 3, pp. 1419-1421, 2012.

[29]   Y. Chang, D.-Y. Wang, Y.-L. Tai, and Z.-G. Yang, "Preparation, characterization and reaction mechanism of a novel silver-organic conductive ink," *Journal of Materials Chemistry,* vol. 22, no. 48, pp. 25296-25301, 2012.

[30]   Y. Tao, Y. Tao, B. Wang, L. Wang, and Y. Tai, "A facile approach to a silver conductive ink with high performance for macroelectronics," *Nanoscale research letters,* vol. 8, no. 1, p. 296, 2013.

[31]   X. Fan *et al.*, "Synthesis of nano-copper particles for conductive ink in gravure printing," in *The 8th Annual IEEE International Conference on Nano/Micro Engineered and Molecular Systems*, 2013: IEEE, pp. 775-778.

[32]   S. Khan, L. Lorenzelli, and R. S. Dahiya, "Technologies for printing sensors and electronics over large flexible substrates: a review," *IEEE Sensors Journal,* vol. 15, no. 6, pp. 3164-3185, 2015.

[33]   D. Tobjörk and R. Österbacka, "Paper electronics," *Advanced Materials,* vol. 23, no. 17, pp. 1935-1961, 2011.

[34]   G. Grau, J. Cen, H. Kang, R. Kitsomboonloha, W. J. Scheideler, and V. Subramanian, "Gravure-printed electronics: recent progress in tooling development, understanding of printing physics, and realization of printed devices," *Flexible and Printed Electronics,* vol. 1, no. 2, p. 023002, 2016.

[35]   B. Thompson, *Printing materials: Science and technology*. Pira International, 1998.

[36]   M. Jung *et al.*, "All-printed and roll-to-roll-printable 13.56-MHz-operated 1-bit RF tag on plastic foils," *IEEE Transactions on Electron Devices,* vol. 57, no. 3, pp. 571-580, 2010.

[37]   M. Pudas, N. Halonen, P. Granat, and J. Vähäkangas, "Gravure printing of conductive particulate polymer inks on flexible substrates," *Progress in Organic Coatings,* vol. 54, no. 4, pp. 310-316, 2005.

[38]   P. Kopola *et al.*, "High efficient plastic solar cells fabricated with a high-throughput gravure printing method," *Solar Energy Materials and Solar Cells,* vol. 94, no. 10, pp. 1673-1680, 2010.

[39]   P. Kopola, M. Tuomikoski, R. Suhonen, and A. Maaninen, "Gravure printed organic light emitting diodes for lighting applications," *Thin Solid Films,* vol. 517, no. 19, pp. 5757-5762, 2009.

[40]   J. Jo, J.-S. Yu, T.-M. Lee, and D.-S. Kim, "Fabrication of printed organic thin-film transistors using roll printing," *Japanese Journal of Applied Physics,* vol. 48, no. 4S, p. 04C181, 2009.

[41]   R. Sangoi *et al.*, "Printing radio frequency identification (RFID) tag antennas using inks containing silver dispersions," *Journal of dispersion science and technology,* vol. 25, no. 4, pp. 513-521, 2005.

[42]   M. J. Joyce *et al.*, "Contribution of Flexo Process Variables to Fine Line Ag Electrode Performance," in *International Journal of Engineering Research and Technology*, 2014, vol. 3, no. 8 (August-2014): ESRSA Publications.

[43]   Y. Noguchi, T. Sekitani, and T. Someya, "Printed shadow masks for organic transistors," *Applied physics letters,* vol. 91, no. 13, p. 3502, 2007.

[44]   S. Khan, L. Lorenzelli, and R. Dahiya, "Screen printed flexible pressure sensors skin," in *25th Annual SEMI Advanced Semiconductor Manufacturing Conference (ASMC 2014)*, 2014: IEEE, pp. 219-224.

[45] C. Shi, X. Shan, G. Tarapata, R. Jachowicz, J. Weremczuk, and H. Hui, "Fabrication of wireless sensors on flexible film using screen printing and via filling," *Microsystem technologies,* vol. 17, no. 4, pp. 661-667, 2011.

[46] G. E. Jabbour, R. Radspinner, and N. Peyghambarian, "Screen printing for the fabrication of organic light-emitting devices," *IEEE Journal of selected topics in quantum electronics,* vol. 7, no. 5, pp. 769-773, 2001.

[47] B. Li, P. Clark, and K. Church, "Robust direct-write dispensing tool and solutions for micro/meso-scale manufacturing and packaging," in *ASME 2007 International Manufacturing Science And Engineering Conference*, 2007: American Society of Mechanical Engineers, pp. 715-721.

[48] K. Hon, L. Li, and I. Hutchings, "Direct writing technology—advances and developments," *CIRP Annals-Manufacturing Technology,* vol. 57, no. 2, pp. 601-620, 2008.

[49] A. Datar, "Micro-extrusion process parameter modeling," 2012.

[50] T. P. Montoya and K. J. Kirshchenmann, "Antennas with discrete resistive loading built by direct-write fabrication," in *Antennas and Propagation Society International Symposium, 2007 IEEE*, 2007: IEEE, pp. 4080-4083.

[51] L.-J. Wei and C. H. Oxley, "Carbon based resistive strain gauge sensor fabricated on titanium using micro-dispensing direct write technology," *Sensors and Actuators A: Physical,* vol. 247, pp. 389-392, 2016.

[52] L. Yang, A. Rida, R. Vyas, and M. M. Tentzeris, "RFID tag and RF structures on a paper substrate using inkjet-printing technology," *IEEE Transactions on Microwave Theory and Techniques,* vol. 55, no. 12, pp. 2894-2901, 2007.

[53] K. R. Zope, D. Cormier, and S. Williams, "Reactive Silver Oxalate Ink Composition with Enhanced Curing Conditions for Flexible Substrates," *ACS applied materials & interfaces,* 2018.

[54] S. D. Hoath, *Fundamentals of Inkjet Printing: The Science of Inkjet and Droplets*. John Wiley & Sons, 2016.

[55] I. Gibson, D. W. Rosen, and B. Stucker, *Additive manufacturing technologies*. Springer, 2010.

[56] A. Wadhwa, "Run-time Ink Stability in Pneumatic Aerosol Jet Printing Using a Split Stream Solvent Add Back System," 2015.

[57] J. Vaillancourt *et al.*, "All ink-jet-printed carbon nanotube thin-film transistor on a polyimide substrate with an ultrahigh operating frequency of over 5 GHz," *Applied Physics Letters,* vol. 93, no. 24, p. 243301, 2008.

[58] R. Liu, H. Ding, J. Lin, F. Shen, Z. Cui, and T. Zhang, "Fabrication of platinum-decorated single-walled carbon nanotube based hydrogen sensors by aerosol jet printing," *Nanotechnology,* vol. 23, no. 50, p. 505301, 2012.

[59] M. Hedges and A. B. Marin, "3D Aerosol Jet® Printing-Adding Electronics Functionality to RP/RM," in *DDMC 2012 conference*, 2012, pp. 14-15.3. 12.

[60] H. Tan, "Numerical study on splashing of high-speed microdroplet impact on dry microstructured surfaces," *Computers & Fluids,* 2017.

[61] Y. Farraj, A. Smooha, A. Kamyshny, and S. Magdassi, "Plasma-Induced Decomposition of Copper Complex Ink for the Formation of Highly Conductive Copper Tracks on Heat-Sensitive Substrates," *ACS Applied Materials & Interfaces,* vol. 9, no. 10, pp. 8766-8773, 2017.

[62]   J. Perelaer and U. S. Schubert, "Novel approaches for low temperature sintering of inkjet-printed inorganic nanoparticles for roll-to-roll (R2R) applications," *Journal of Materials Research,* vol. 28, no. 4, pp. 564-573, 2013.

[63]   K. A. Schroder, "Mechanisms of photonic curing™: Processing high temperature films on low temperature substrates," *Nanotechnology,* vol. 2, pp. 220-223, 2011.

[64]   W.-H. Chung, H.-J. Hwang, and H.-S. Kim, "Flash light sintered copper precursor/nanoparticle pattern with high electrical conductivity and low porosity for printed electronics," *Thin Solid Films,* vol. 580, pp. 61-70, 2015.

[65]   Y. Zheng, Z. He, Y. Gao, and J. Liu, "Direct desktop printed-circuits-on-paper flexible electronics," *Scientific reports,* vol. 3, 2013.

[66]   Y. Zheng, Z.-Z. He, J. Yang, and J. Liu, "Personal electronics printing via tapping mode composite liquid metal ink delivery and adhesion mechanism," *Scientific reports,* vol. 4, p. 4588, 2014.

[67]   Q. Zhang, Y. Gao, and J. Liu, "Atomized spraying of liquid metal droplets on desired substrate surfaces as a generalized way for ubiquitous printed electronics," *Applied Physics A,* vol. 116, no. 3, pp. 1091-1097, 2014.

[68]   L. Wang and J. Liu, "Liquid phase 3D printing for quickly manufacturing conductive metal objects with low melting point alloy ink," *Science China Technological Sciences,* vol. 57, no. 9, pp. 1721-1728, 2014.

[69]   C. Jin, J. Zhang, X. Li, X. Yang, J. Li, and J. Liu, "Injectable 3-D fabrication of medical electronics at the target biological tissues," *Scientific reports,* vol. 3, 2013.

[70]   L. Yi, C. Jin, L. Wang, and J. Liu, "Liquid-solid phase transition alloy as reversible and rapid molding bone cement," *Biomaterials,* vol. 35, no. 37, pp. 9789-9801, 2014.

[71] S. Vader and Z. Vader, "Conductive liquid three dimensional printer," ed: Google Patents, 2017.

[72] V. Systems, "Viktor Sukhotskiy Vader Systems SFF 2017 presentation," ed, 2017.

[73] E. Pál, V. Zöllmer, D. Lehmhus, and M. Busse, "Synthesis of Cu 0.55 Ni 0.44 Mn 0.01 alloy nanoparticles by solution combustion method and their application in aerosol printing," *Colloids and Surfaces A: Physicochemical and Engineering Aspects,* vol. 384, no. 1, pp. 661-667, 2011.

[74] W. Zhao *et al.*, "Nanoalloy Printed and Pulse-Laser Sintered Flexible Sensor Devices with Enhanced Stability and Materials Compatibility," *ACS nano,* vol. 9, no. 6, pp. 6168-6177, 2015.

[75] M. D. Porter, *Combinatorial materials science*. John Wiley & Sons, 2007.

[76] A. Freeman, K. Poeppelmeier, T. Mason, R. Chang, and T. Marks, "Chemical and thin-film strategies for new transparent conducting oxides," *MRS bulletin,* vol. 25, no. 8, pp. 45-51, 2000.

[77] J. Perkins *et al.*, "A Combinatorial Approach to TCO Synthesis and Characterization," *MRS Online Proceedings Library Archive,* vol. 666, 2001.

[78] H. Reichenbach and P. McGinn, "Combinatorial synthesis of oxide powders," *Journal of Materials Research,* vol. 16, no. 4, pp. 967-974, 2001.

[79] T. R. Cull, M. J. Goulding, and M. Bradley, "Liquid Crystal Libraries—Ink-jet Formulation and High-Throughput Analysis," *Advanced Materials,* vol. 19, no. 17, pp. 2355-2359, 2007.

[80] S. Okamura, R. Takeuchi, and T. Shiosaki, "Fabrication of ferroelectric Pb (Zr, Ti) O3 thin films with various Zr/Ti ratios by ink-jet printing," *Japanese journal of applied physics,* vol. 41, no. 11S, p. 6714, 2002.

[81] M. M. Mohebi and J. R. Evans, "A drop-on-demand ink-jet printer for combinatorial libraries and functionally graded ceramics," *Journal of combinatorial chemistry,* vol. 4, no. 4, pp. 267-274, 2002.

[82] M. M. Mohebi and J. R. Evans, "Combinatorial Ink-Jet Printer for Ceramics: Calibration," *Journal of the American Ceramic Society,* vol. 86, no. 10, pp. 1654-1661, 2003.

[83] H. M. Reichenbach and P. J. McGinn, "Combinatorial solution synthesis and characterization of complex oxide catalyst powders based on the LaMO 3 system," *Applied Catalysis A: General,* vol. 244, no. 1, pp. 101-114, 2003.

[84] A. K. Murray *et al.*, "Two-component additive manufacturing of nanothermite structures via reactive inkjet printing," *Journal of Applied Physics,* vol. 122, no. 18, p. 184901, 2017.

[85] P. J. Smith and A. Morrin, "Reactive inkjet printing," *Journal of Materials Chemistry,* vol. 22, no. 22, pp. 10965-10970, 2012.

Chapter 3 Ink Formulations

3.1. Introduction

As described in earlier chapters, nanoalloy particles show a wide range of properties which are useful in biomedical and electronic applications. 3D printing of nanoalloys is not yet scaled up in comparison with the printing of single metal elements. Most of the printing techniques use nanoalloy particles or alloy inks which have fixed elemental compositions. Printing multifunctional components with different alloy compositions requires changing the nanoalloy ink every time. This increases the time of printing as well as the fabrication cost. The process of controlling the alloy composition while printing is still not explored. Since the properties of alloys vary with changes in the elemental composition, a printing process which could digitally dispense alloy inks having specific desired compositions would enable different functionalities. This chapter focuses on the research approach to achieve formation of digital nanoalloys by mixing individual metal precursor inks in desired proportions. Ink formulation of copper and nickel MOD precursor inks along with their characterizations are explained in detail. An experiment confirming the basic feasibility of formation of nanoalloys by mixing individual elemental inks is also presented.

3.2. Overview

Inkjet printing has been used to print functional nanoparticle metal inks and MOD precursor inks of copper and silver onto different substrates. However, the inkjet printing of multi-element alloy inks is still in its early stages. Conventional inkjet printing prints a color image on the paper by tightly controlling the relative proportions of each ink (i.e. cyan, yellow, magenta, and black) at a given location in the image. A similar process can be used to print multi-element

nanoalloy inks onto the substrate. In this case, each element in the alloy is formulated into its own individual metal ink, and the "color" in the image maps to proportions of the individual elemental inks rather than cyan, yellow, magenta, and/or black. This approach allows for spatial control of the nanoalloy composition. Since inkjet printing is amongst the few printing processes which can jet a known volume of ink onto the substrate, the jetting parameters can be varied so that individual metal inks of defined volumes land on the same spot to produce an alloy of preferred composition. Printing of mixed metal oxides has been reported in the literature [1, 2], but printing of metallic alloys is a challenge because of issues such as formation of oxides and removal of carbon from the sintered sample.

This research work aims to gain insight into the printing of digital nanoalloy compositions by *ex-situ* mixing of individual elemental inks (i.e. mixing on the substrate after jetting) in appropriate proportions. Using the binary copper-nickel system as an example, the formation of nanoalloy with MOD precursor ink is reported. Since copper and nickel both have a face centered cubic (FCC) structure and show complete miscibility in each other, formation of their nanoalloy is, in theory, relatively straightforward. By printing MOD precursor inks, problems associated with nanoparticle inks such as ink stability and nozzle clogging can be avoided.

In recent years, copper nickel nanoalloys have gained considerable interest in the research community due to the conductivity of copper and the corrosion resistance of nickel. For this reason, they are potential candidates as electrodes in corrosive environments. CuNi alloys are used in marine applications [3], solid oxide fuel cells [4], glucose sensors [5], hydrogenation of refined soybean oil [6], photodegradation of organic dyes [7], and in hyperthermia therapy [8]. Different methods have been used to fabricate CuNi nanoalloy particles. Chemical methods include electrochemistry [5], hydrothermal reduction [7, 9], microemulsions [10, 11], mechanical alloying

[12, 13], reduction of polyols [13, 14] or salts [15, 16], and solution combustion [17, 18]. Synthesizing such nanoalloy particles is often accompanied by undesirable contamination in the final composition. For example, impurities from the metal salts may not be completely removed by repeated washing and drying of the nanoparticles. Oxidation is also a problem, requiring special care during washing, filtering, and drying of the nanoalloy particles. Printing individual copper and nickel precursor inks in desired proportions directly onto a substrate to form a nanoalloy film will eliminate some of the problems encountered in the synthesis and use of premade nanoparticles. The copper, nickel, and alloy ink formulations and characterizations are explained in detail below.

3.3. MOD ink formulations

To realize the formation of a nanoalloy using MOD precursor inks, individual inks of copper and nickel were formulated. The same ligand molecule (ethylene diamine: $NH_2CH_2CH_2NH_2$) and carrier solvent (ethylene glycol: $HOCH_2CH_2OH$) were used to prepare the individual inks to avoid immiscibility and solubility issues during mixing. Nickel formate dihydrate (molecular weight (MW): 184.77) and copper formate tetrahydrate (molecular weight (MW): 225.65) were purchased from Alfa Aesar, USA. Ethylene diamine was purchased from Fisher Scientific, USA and ethylene glycol was purchased from Sigma-Aldrich, USA. All chemicals used were analytical grade. These chemicals were used without further purification. Glass microscope slides (Thermo Scientific, USA), Kapton® film (DuPont USA, 5 mil thick) and single crystal quartz (MTI corporation, USA) were used as substrates and were cleaned with isopropyl alcohol before ink deposition.

To formulate copper MOD precursor ink, ethylene glycol (EG) (2 ml) was used as the solvent. Ethylene diamine (ED) (0.36 ml, 5.39 mmol) was used as the ligand and was added to the ethylene glycol. The mixture was stirred at room temperature for 15 minutes. Copper formate

tetrahydrate (0.61 g, 2.70 mmol) was added to the solution and stirred at room temperature for one hour. A dark blue color was formed indicating the formation of a copper amine complex. The ink was filtered through a 0.2 µm syringe filter. The nickel precursor (MOD) ink formulation was adapted from the patent published by Ginley *et al.* [19]. To formulate the nickel ink, ethylene glycol (2 ml) was used as the solvent. Ethylene diamine (0.36 ml, 5.39 mmol) was used as the ligand and added to the ethylene glycol. The mixture was stirred at room temperature for 15 minutes. Nickel formate (0.50 g, 2.70 mmol) was added to the solution and stirred at room temperature for one hour. The ink turned from green to purple indicating the formation of a nickel amine complex. The ink was filtered through a 0.2 µm syringe filter. Table 3-1 show the ink compositions for copper and nickel MOD precursor inks. To formulate the alloy inks, copper and nickel inks were mixed in the desired ratios and stirred at room temperature.

Table 3-1: MOD precursor ink composition

	Additive	Amount	Mole
Ni MOD ink	Nickel formate dihydrate	0.5 g	2.70 mmol
	Ethylenediamine	0.36 ml	5.39 mmol
	Ethylene glycol	2 ml	35.86 mmol
Cu MOD ink	Copper formate tetrahydrate	0.61 g	2.70 mmol
	Ethylenediamine	0.36 ml	5.39 mmol
	Ethylene glycol	2 ml	35.86 mmol

3.4. Ink characterization

The copper and nickel MOD precursor inks contain the metal formate salts complexed by ethylenediamine. The electron pair from the nitrogen of ethylenediamine forms a coordinate bond with the metal ions. Formate ions were used because of their low molecular weight and volatility [20]. Furthermore, the decomposition of formate is accompanied by the release of carbon dioxide

and molecular hydrogen, (Eq. 1 & Eq. 2), the latter of which generates a reducing atmosphere, thus limiting the amount of oxidation of the reduced metals [21].

$$2\ HCOO^- \rightarrow 2\ CO_2 + H_2 + 2e^- \qquad\qquad \text{Eq. 3.1}$$

$$M^{2+} + 2e^- \rightarrow M^0 (M = Cu\ or\ Ni) \qquad\qquad \text{Eq. 3.2}$$
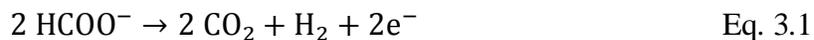
The bidentate ethylenediamine was used in the formation of the metal complex to enhance the reduction efficiency, achieve complex stability, and increase solubility in the solvent. Ethylene glycol was used as a solvent to obtain suitable solubility and rheological properties for inkjet printing. The high boiling point (~ 198 °C) of ethylene glycol also enables reduction of the complex to metal at elevated temperature. Other solvents such as water could be used as a solvent to reduce the viscosity of the MOD precursor ink.

In order to determine the structure of the complex, infrared spectroscopy (IR) was used for copper MOD ink, nickel MOD ink, ethylenediamine, and ethylene glycol. The IR spectroscopy measures the vibrations of atoms and determines functional groups in molecules. Figure 3-1 shows the primary IR absorbance for ethylene glycol, ethylenediamine, and the copper and nickel precursor (MOD) inks. As expected, all of the EG peaks in the ink spectra match those associated with neat EG. EG vibrational transitions in the ink do not exhibit any evidence of metal-EG interactions through vibrational peak damping or significant spectral band shifting. The IR spectra (Figure 3-1) also confirms that the ED is directly complexed to the metals as indicated by dampening of the IR frequencies assigned to amine transitions.
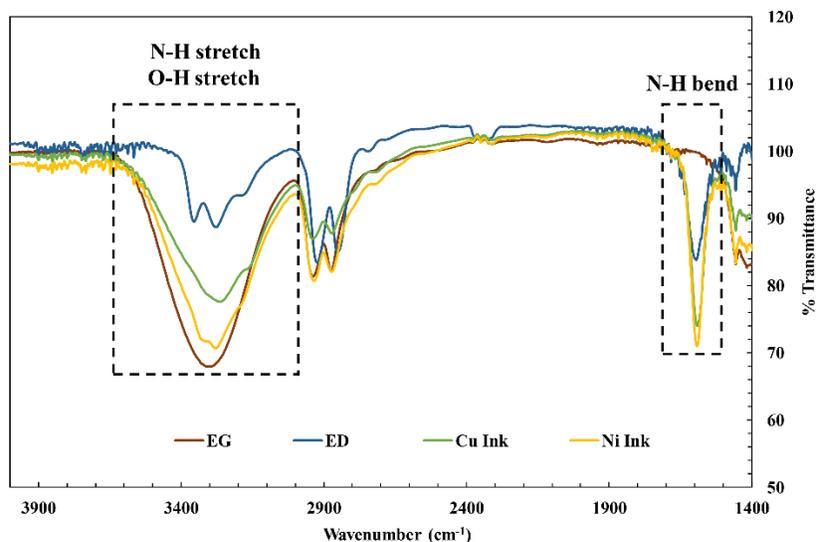
Figure 3-1: IR spectra of ethylene glycol (EG), ethylenediamine (ED), copper ink and nickel ink. Reproduced from [22] licensed under CC by 4.0

To determine the metal weight in the formulated ink and the temperature at which reducing atmosphere is generated, thermogravimetric analysis (TGA) and mass spectrometry (MS) were performed on the copper and nickel MOD inks. The TGA monitors the mass of the sample material while it is heated to give a plot of mass loss as a function of temperature. TGA was performed by heating the ink sample in a platinum pan from room temperature to 300 °C at 10 °C/min. The MS analyzes the gases that leave the sample as it is heated. For MS analysis, 4.0 µl of the ink was placed onto clean glass wool inside of a 0.25 inch OD glass tube. These were then placed into the autosampler tray (Gerstel TDSA, Germany) with the open ends blocked with Viton® O-rings. Each tube was individually loaded into the chamber which was heated to 30˚C while helium flowed through the tube at 100 ml/min. Effluent from the tube was split, with 1.0 ml/min directed into the mass spectrometer (Agilent 5973, USA) through a heated one meter transfer line. The remainder of the effluent was vented. The sample tube was heated from room temperature to 280 ˚C at a rate of 10 ˚C/min.

Figures 3-2(a) and 3-2(b) show the TGA–MS results for copper and nickel precursor inks respectively. For both the inks, the thermal decomposition occurs in two stages. The solvent evaporates first, followed by the metal reduction. In the first stage (< 130 °C), ethylene glycol and water are released leaving behind the metal complex. The reduction of the copper and nickel MOD precursor inks occur at ~ 155 °C and ~ 220 °C respectively. The metal complex decomposition evolves carbon dioxide, carbon monoxide and ethylenediamine, consistent with the reactions in Eq. 3.1 and Eq. 3.2. The final solid loadings of copper and nickel are 6.5 % and 4.5 % w/w respectively.
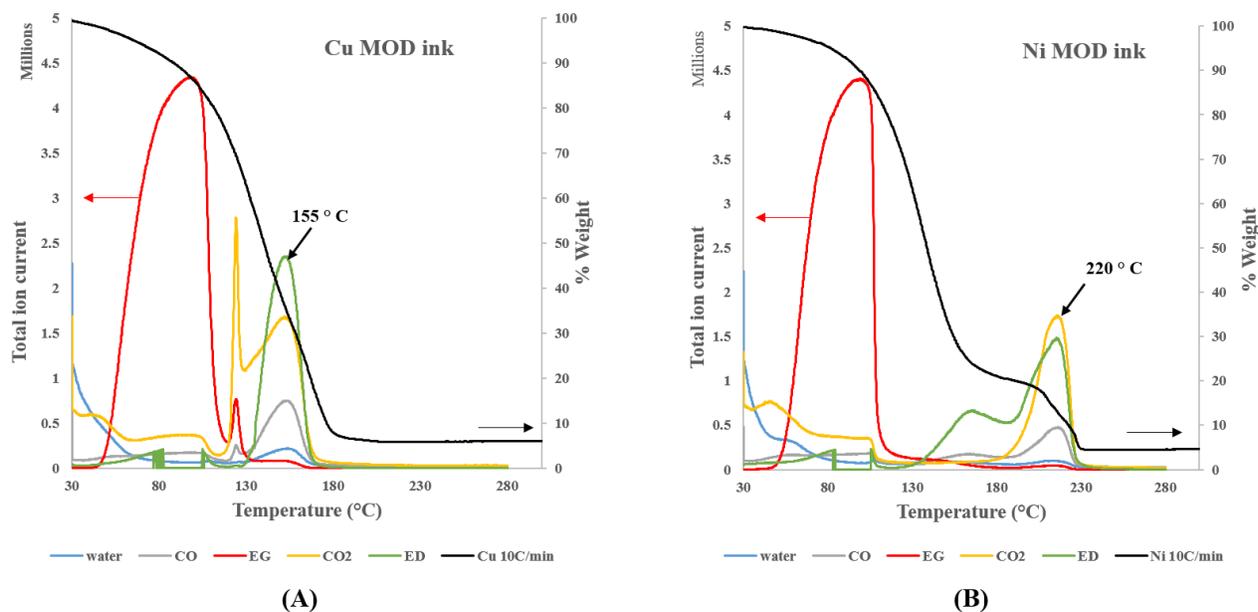
Figure 3-2: Thermal analysis mass spectrometry (TA - MS) of (A) Cu and (B) Ni precursor inks. Reproduced from [22] licensed under CC by 4.0

To observe the nanoparticles in the scanning electron microscope (SEM), the ink was drop casted on a glass substrate and was reduced in the furnace at 230 °C with a ramp up rate of 10 °C/ min. Figure 3-3 shows SEM images of the reduced copper and nickel from the precursor inks. The metal deposits are composed of sintered nanoparticles having an average particle size around 500

nm. The size of the particles are dependent on various factors such as the rates of reaction, nucleation and crystal growth [23]. Small particles can coalesce into larger particles. The XRD analysis also confirmed the reduction of the inks to elemental copper and nickel (Figure 3-4).

(A)   **(B)**
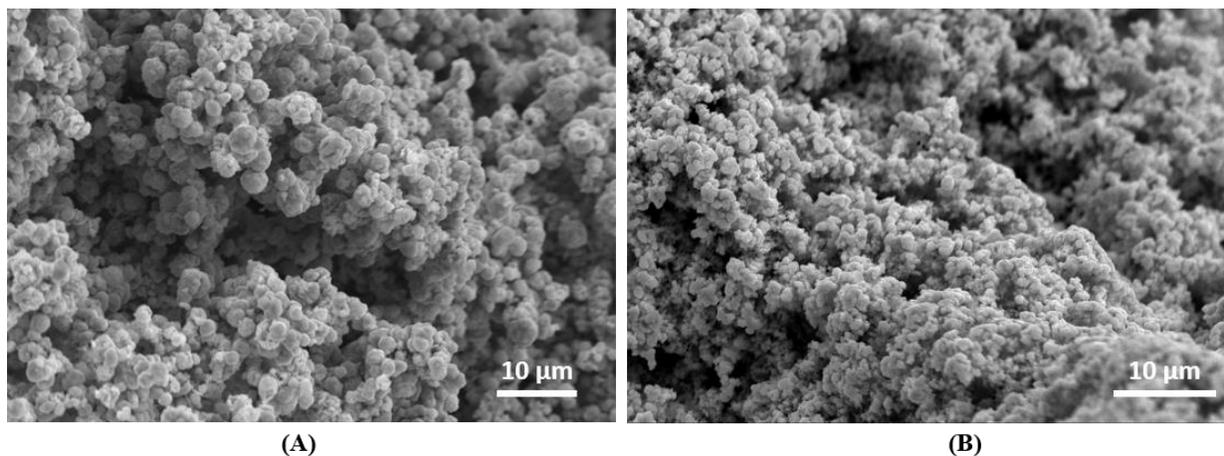
Figure 3-3: SEM image of (A) copper and (B) nickel film sintered in N$_2$ atmosphere. Reproduced from [22] licensed under CC by 4.0
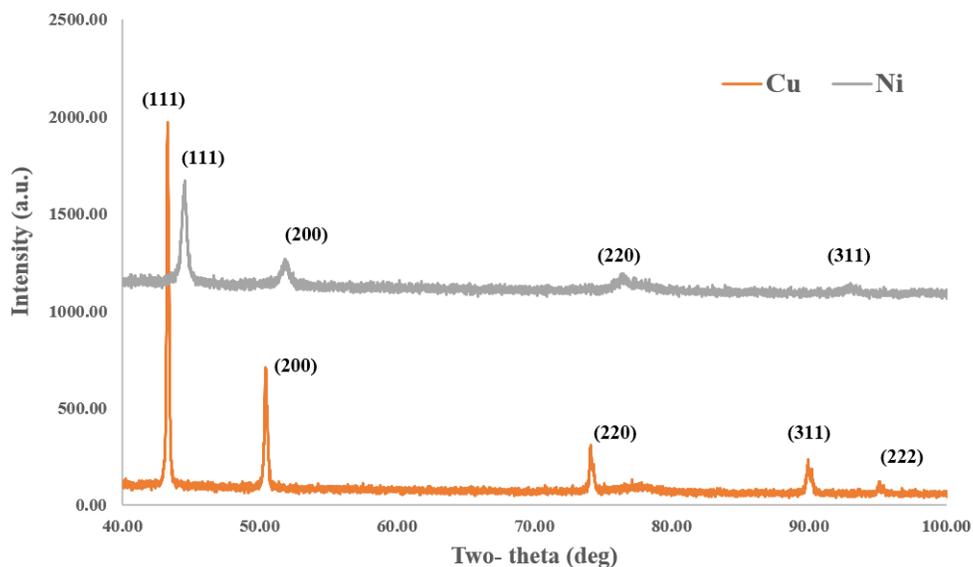
Figure 3-4: X-ray diffraction patterns for reduced copper and nickel films on quartz substrate. Reproduced from [22] licensed under CC by 4.0

To confirm the formation of copper and nickel crystal structure, XRD diffraction patterns of the inks were used to calculate the lattice parameter values and to compare them with values reported in the literature. The lattice parameter of a metal, alloy or a compound is the spacing between the adjacent unit cells in a crystal structure. The diffraction pattern obtained from the XRD determines the arrangement of atoms in a crystal structure via the Bragg condition as given in Eq. 3.3 [24].

$$\lambda = 2d_{hkl} \sin \theta \qquad \text{Eq. 3.3}$$

Where λ is the wavelength of the radiation, d_{hkl} is the distance between the hkl planes of the lattice where h, k, and l are the Miller indices and θ is the diffraction angle. For cubic crystals like copper and nickel with lattice parameter a, the spacing d between the hkl lattice planes is given by

$$d = \frac{a}{\sqrt{h^2+k^2+l^2}} \qquad \text{Eq. 3.4}$$

From the diffraction pattern of the sintered sample and the wavelength for Cu (Kα1) radiation, the lattice parameter 'a' for a crystal structure can be calculated using Eq. 3.3 and 3.4. Kα1 peak positions for the sintered inks were obtained from Pearson type VII peak decomposition [25]. The precise lattice parameter was determined from a plot of lattice parameter versus $\cos^2\theta/\sin\theta$ [26]. The experimental lattice parameters for copper and nickel were found to be 3.6144 Å and 3.5242 Å respectively. These values are in good agreement with the lattice parameters for pure copper (3.614 Å, PDF# 00-004-0836) and pure nickel (3.524 Å, PDF# 00-004-0850). The calculations to determine the lattice parameters is attached in APPENDIX-A.

Differential thermal analysis was performed on copper and nickel MOD precursor inks to determine the thermal events during the reduction process. The differential thermal analysis records the temperature difference between the sample pan and the reference pan during the heating process. The plot of temperature difference against temperature shows the thermal activity of the sample. The endothermic or exothermic event occurring in the ink is detected relative to the inert reference sample. Figure 3-5 shows the differential thermal analysis for inks when heated up to 300 °C at 10 °C/minute. The reduction of copper and nickel to their elemental states occurs in four stages. The first stage is the same for both the inks and includes evaporation of ethylene glycol and water as indicated by the endothermic region below 140 °C. The second stage includes reduction of the metal complex as indicated by the exothermic range up to 155 °C for copper and around 200 °C for nickel. The exothermic ranges for the metals match the TGA-MS (Figure 3.2). Nucleation takes place in the third stage. This is indicated by endothermic range from ~ 160-180 °C for Cu, and ~195-230 °C for Ni. Nucleation can be affected by impurities present in the ink and/or substrate. Impurities may inhibit or accelerate the rate of the reactions. The fourth stage is the crystal growth indicated by exothermic ranges > ~ 180 °C for Cu and ~ 230 °C for Ni.
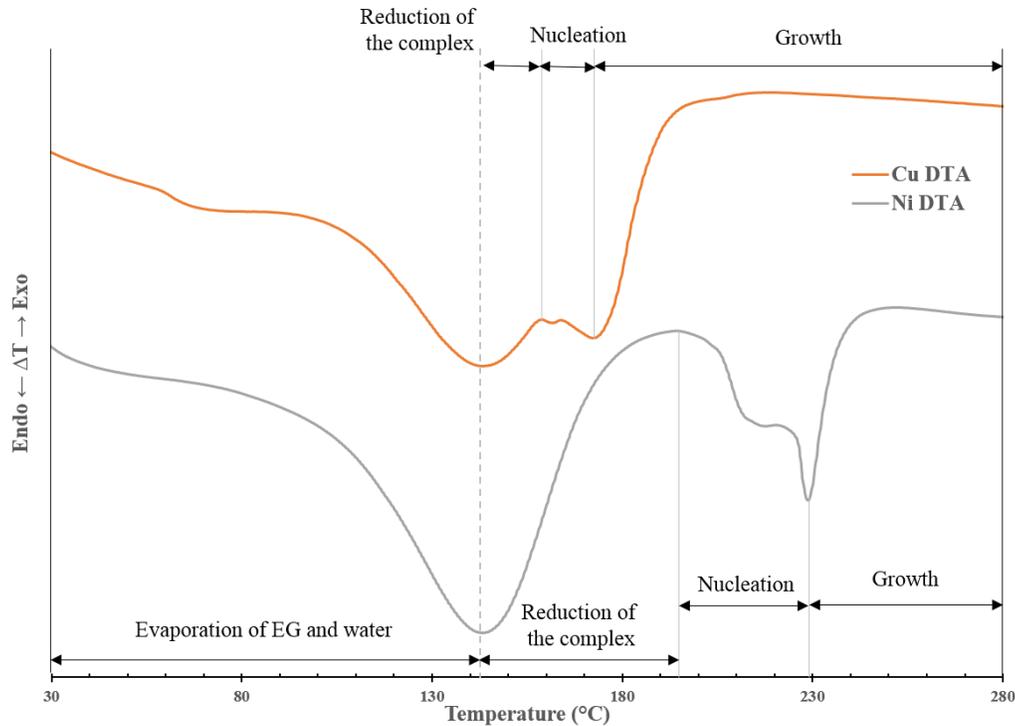
Figure 3-5: Differential thermal analysis for copper MOD ink and nickel MOD ink at 10 °C/minute. Reproduced from [22] licensed under CC by 4.0

The copper and nickel MOD precursor inks show formation of elemental copper and nickel upon reduction. To determine the formation of nanoalloy by mixing individual metal precursor inks, an alloy ink was formulated by mixing copper and nickel MOD ink in ratio of (1:1). The alloy ink characterization and different sintering conditions are explained below.

3.5. Alloy ink characterization

Figure 3-6 shows a proposed schematic overview of the nanoalloy formation process using copper and nickel precursor inks. The copper and nickel nuclei formed after the reduction reaction result in copper-nickel nanoalloy particles. The nanoalloy particles formed have inhomogeneous concentrations of copper and nickel atoms. These nanoalloy particles subsequently sinter into a continuous film due to surface diffusion.

57
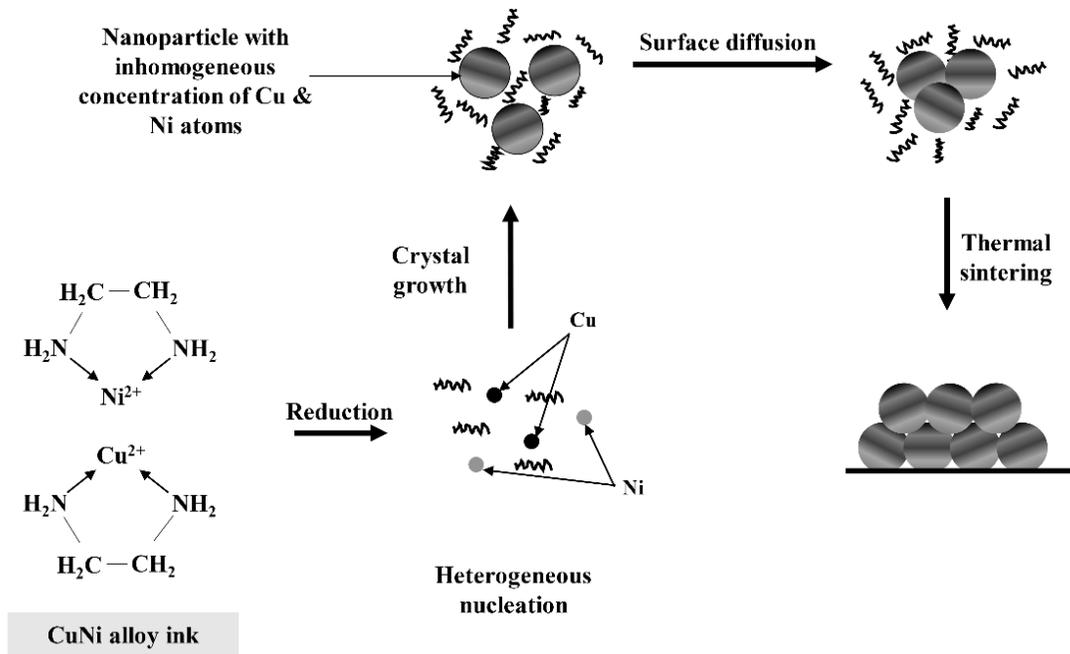
Figure 3-6: Schematic overview of formation of nanoalloy structure onto a substrate. Reproduced from [22] licensed under CC by 4.0

To observe the formation of alloy in different sintering conditions, the copper and nickel MOD inks were mixed together in the ratio of 1:1 and stirred at room temperature for 1 hr. The ink was printed using the drop casting technique and sintered in one of three different ways – on a hotplate, or in an oven with either vacuum or inert atmosphere (N_2) conditions. The distribution of copper and nickel in the sintered film was observed using Scanning Electron Microscopy with Energy-Dispersive X-Ray Spectroscopy (EDS) elemental mapping. The elemental map shows the spatial distribution and relative intensities of elements present over the scanned area. The relative intensities associated with different elements in the sample are color coded in a 2D image. Different locations of the film were scanned in order to see the distribution throughout the sintered sample.

Sintering on hot plate: The printed alloy ink was sintered on a magnetic hotplate at 230 °C for 30 min. The EDS elemental mapping (Fig. 3-7) shows clear segregation between reduced copper and nickel. The reason for the segregation is presumed to be related to the magnet present underneath the hotplate which was used to mix the solutions using a magnetic stir bars. Since nickel is a ferromagnetic material, it is attracted to a magnet. In the process of reduction of the alloy ink, the nickel particles formed were attracted to each other in presence of magnetic field. This caused segregation between the reduced copper and nickel nanoparticles. A hot plate with no magnet underneath showed no such segregation (Fig. 3-8). The phenomena of reduction of nickel MOD precursor ink in presence of magnetic field shows potential for aligning nickel nanoparticles in direction of the magnetic field. Different types of microstructures can be fabricated onto a substrate by changing the direction of the magnetic field. The effect of aligned nickel particles on electric and magnetic properties of sintered film is explained in detail in Chapter 5.
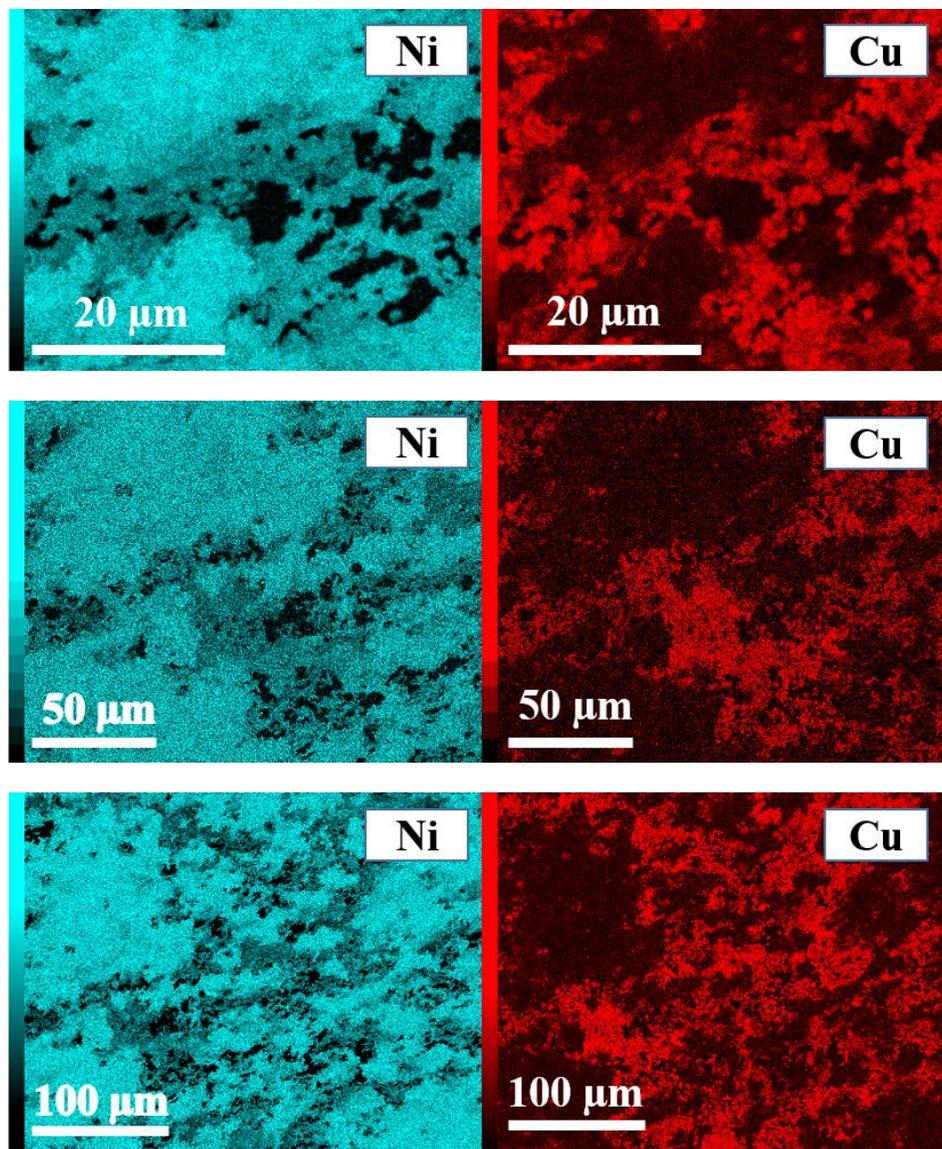
Figure 3-7: EDS elemental mapping plots on samples sintered on a magnetic hotplate
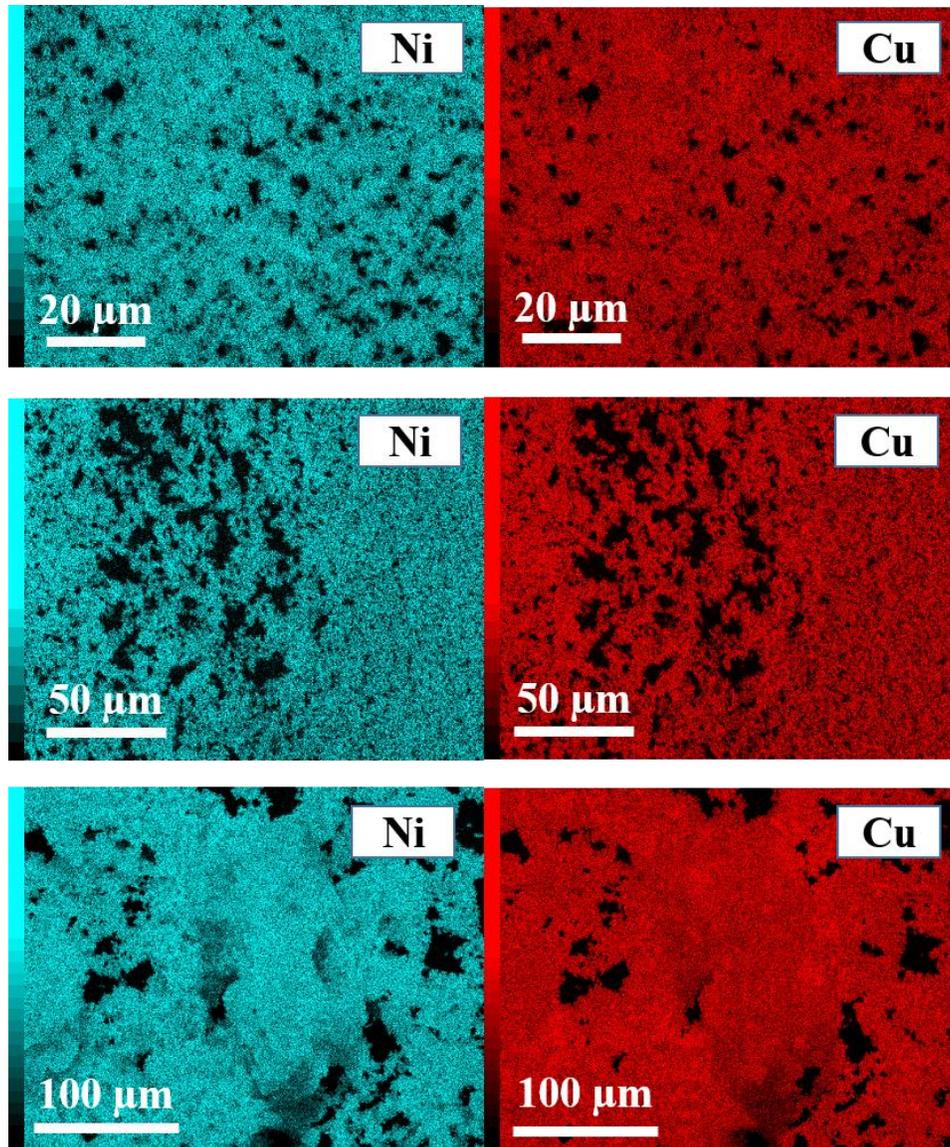
Figure 3-8: EDS elemental mapping plots on samples sintered on a nonmagnetic hotplate.

Sintering in inert atmosphere: The printed alloy ink was sintered in an inert atmosphere (N_2) at 230 ℃ for 30 min with ramp up rate of 10 ℃/min. The elemental mapping (Fig. 3-9) shows much more uniform mixing of copper and nickel. The elemental composition shows approximately 1:1 ratio of copper and nickel with some trace amount of carbon, oxygen, and nitrogen.
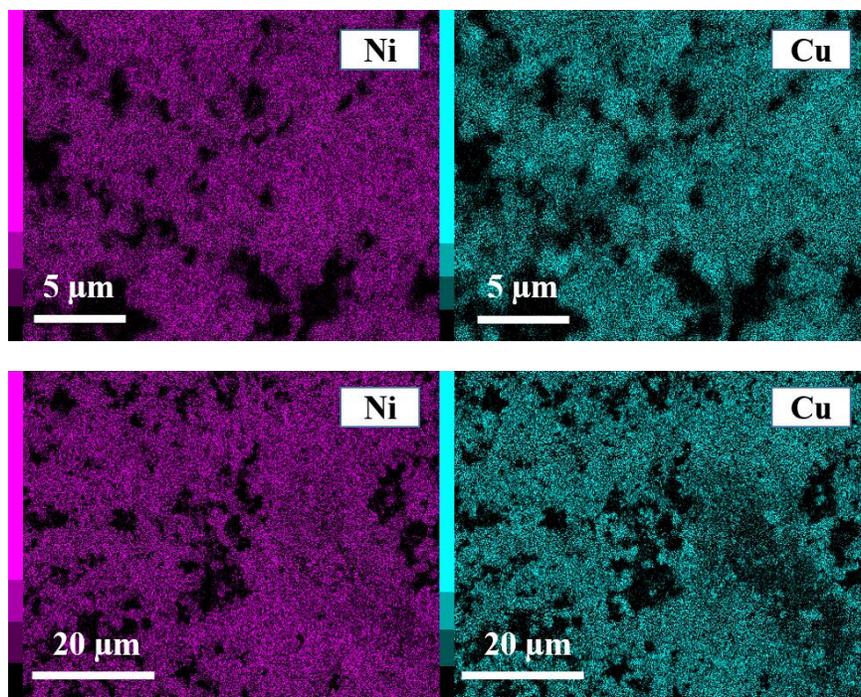
Figure 3-9: EDS elemental mapping plots on samples sintered in an inert atmosphere

Sintering in vacuum: The printed alloy ink was sintered in a vacuum furnace at 230 °C for 30 min with ramp up rate of 10 °C/min. The elemental mapping (Fig. 3-10) shows similar mixing patterns as seen in samples sintered under inert atmosphere. Much more uniform mixing of copper and nickel were observed. The elemental composition shows approximately 1:1 ratio of copper and nickel with some trace amount of carbon and oxygen. The percentage of carbon and oxygen in the samples sintered in vacuum furnace were less in comparison with the ones sintered in an inert atmosphere.
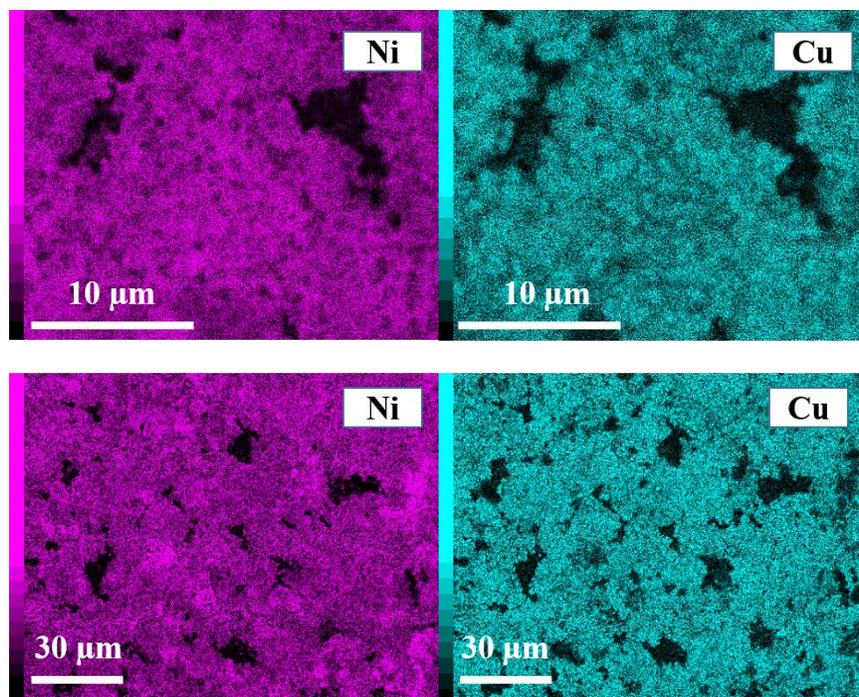
Figure 3-10: EDS elemental mapping plots on samples sintered in a vacuum furnace

The sintering in vacuum and inert atmosphere show no segregation of copper and nickel. However, the EDS elemental mapping shows a 2D image based on the elements present in the scanned area. It does not show the crystalline phases present in the alloy. To assess whether or not a CuNi alloy was formed and to understand the phases present, XRD analyses were carried out on the sintered sample.

Alloy ink (CuNi, 1:1) was drop casted on a single crystal quartz substrate (X-cut - 110) and sintered in a vacuum furnace at 230 °C for 30 min with ramp up rate of 10 °C/min. The final sintered film was characterized by a RIGAKU DMax-IIB X–ray diffractometer. The EDS elemental mapping (Figure 3-11 (A)) as seen in previous section shows no segregation of copper and nickel (within the measurement resolution). The X-ray diffraction pattern in Figure 3-10 (C) shows peaks for both a copper phase and a copper-nickel alloy phase. The lattice parameter obtained for the copper peak was 3.6143 Å, and for the copper-nickel alloy peak was 3.5318 Å.

Using Vegard's law, the composition of the alloy phase was estimated to be Cu_8Ni_{92}. The calculations to determine the lattice parameter and composition of alloy phase are presented in APPENDIX-A. The TEM of the drop casted film sintered at 2°C/min in a vacuum furnace was also studied and the results are presented in APPENDIX B.
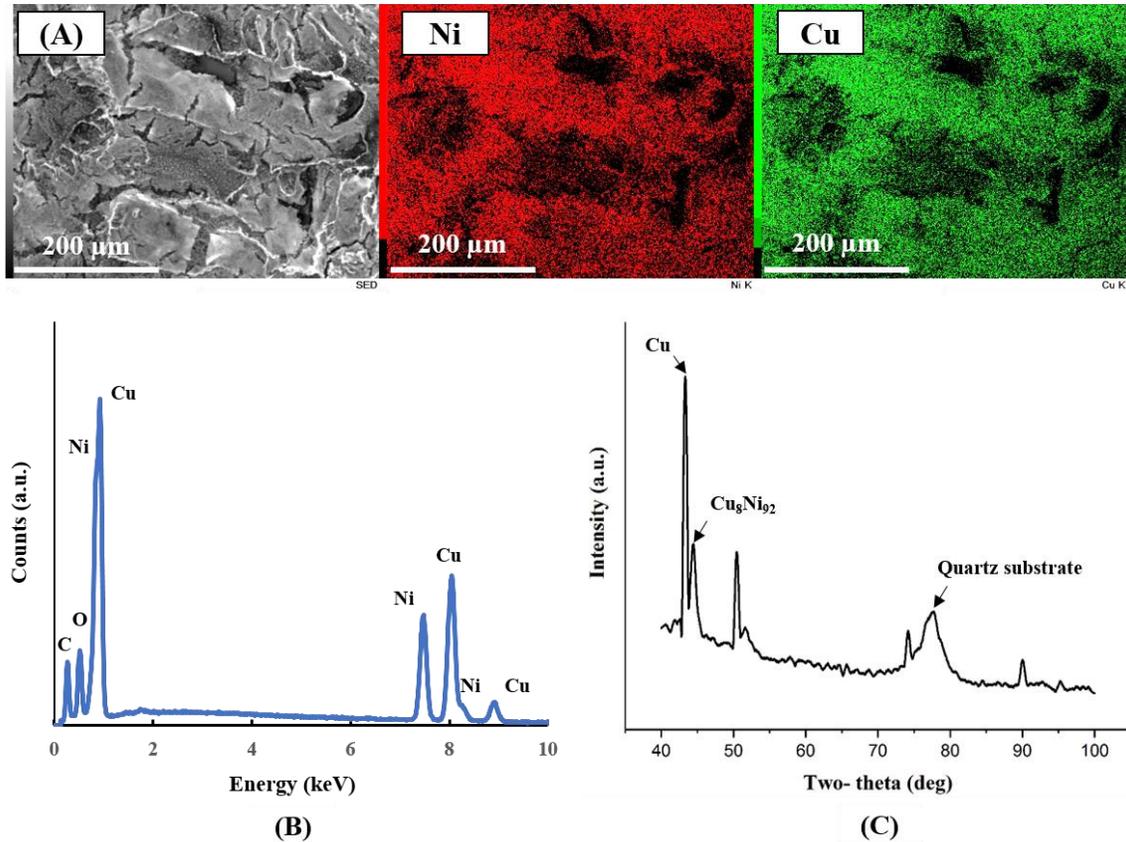
Figure 3-11: (A) EDS elemental maps on samples sintered in a vacuum furnace. (B) EDS spectrum of the sintered sample. (C) X-ray diffraction pattern for sintered film on quartz substrate. Reproduced from [22] licensed under CC by 4.0

The XRD shows the presence of two phases in the sintered film of copper and nickel rich CuNi alloy. This indicates the reduction of copper first followed by reduction of nickel. In order to observe the endothermic and exothermic events for the formation of bi-metallic film, DTA was carried out for Cu, Ni and CuNi MOD inks at 2 °C/min (Figure 3-12). As shown above for 10

64

°C/min, the reduction of the metal complex to elemental metal was observed in four stages (S1: solvent evaporation, S2: reduction of the complex, S3: Nucleation and S4: Growth). The first stage (S1) was the same for all inks. The copper complex reduces at a lower temperature than nickel due to its higher reduction potential. For the CuNi alloy ink, copper reduces first and provides nucleation sites for nickel which reduces later when the temperature is increased. The endothermic peak for the nickel reduction (in CuNi ink) takes place at a lower temperature than for the Ni ink suggesting that the presence of copper nanoparticles may catalyze the reaction. This corroborates the results obtained from the XRD where copper and the copper-nickel alloy phases were observed. The resulting alloy films have a layered structure with copper reducing first at the substrate and a non-uniform distribution of Cu and Ni atoms (CuNi) alloy on top of the reduced copper.
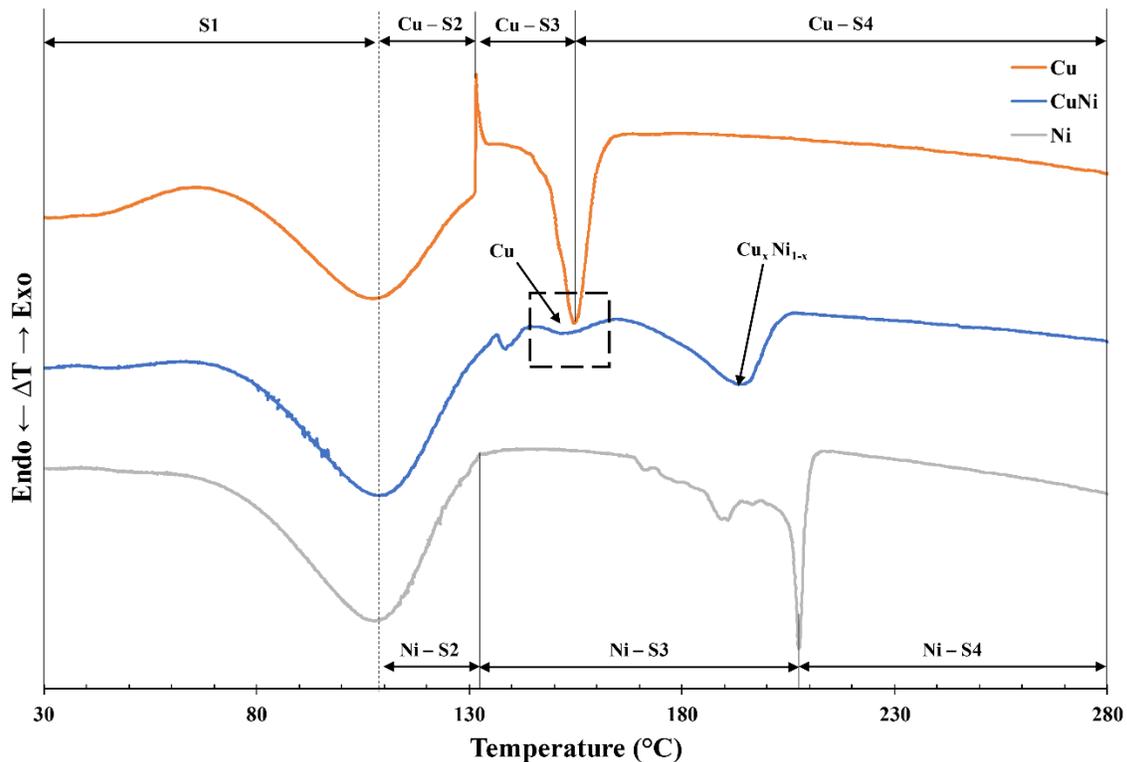
Figure 3-12: Differential thermal analysis for copper MOD ink, nickel MOD ink, and CuNi alloy MOD ink.

Reproduced from [22] licensed under CC by 4.0

65

The DTA and XRD analyses suggest the presence of two phases with copper as one phase and nickel rich alloy as the second phase. The theory behind the phase separation can be explained using the Eyring equation [27] which considers the temperature dependence and change in the Gibbs free energy (ΔG). The change in the Gibbs free energy is the driving force for the reduction of metal to its elemental state. The relation of ΔG with the reduction potential of a metal is measured using the cell potential (E_{cell}) under standard conditions and is given by

$$\Delta G = -nFE_{cell}$$

Eq. 3.5

where n (mol) is the number of electrons transferred in the reaction, and F is the Faraday constant (96500 C/mol). E_{cell} is the potential difference (J/C) which is given by

$$E_{cell} = E_{reduction} + E_{oxidation}$$

Eq. 3.6

where $E_{reduction}$ is the reduction potential and $E_{oxidation}$ is the oxidation potential of the ions.

For copper and nickel MOD precursor inks, copper and nickel ions are reduced by accepting two electrons. The standard reduction potential for copper and nickel is [28]

$$Cu^{2+} + 2e^- \rightarrow Cu^0 \ + 0.337\ V$$

$$Ni^{2+} + 2e^- \rightarrow Ni^0 \ - 0.24\ V$$
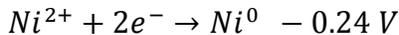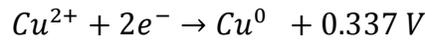
In this reaction, the formate ion is oxidized by losing electrons to form carbon dioxide. The standard oxidation potential for the formate ion is [29]

$$HCOO^- + OH^- \rightarrow CO_2 + H_2O + 2e^- + 0.43\ V$$
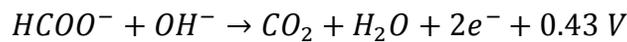
The cell potential can be calculated by substituting the reduction and oxidation potentials in Eq. 3.6

$$E_{Cu} = 0.337 + 0.43 = 0.767\ V$$

$$E_{Ni} = -0.24 + 0.43 = 0.19\ V$$

The change in the Gibbs free energy for the reduction of copper and nickel can be calculated by substituting the cell potential values in Eq. 3.5

$$\Delta G_{Cu} = -nFE_{Cu} = -(2 * 96500 * 0.767) = -148031\ J \approx -148\ kJ$$

$$\Delta G_{Ni} = -nFE_{Ni} = -(2 * 96500 * 0.19) = -36670\ J \approx -37\ kJ$$

As the change in Gibbs free energy for copper is much lower than that of nickel, the reduction of copper is thermodynamically favored over the reduction of the nickel. Also, the rate of reaction increases exponentially with the temperature and is determined using the Eyring equation [27]

$$k = \frac{k_B T}{h} e^{-\frac{\Delta G}{RT}} \qquad \text{Eq. 3.7}$$

where k is the rate constant, k_B is Boltzmann's constant, h is Planck's constant, R is the gas constant, T is the absolute temperature, and ΔG is the Gibbs free energy of activation. Since the change in Gibbs free energy for copper is lower than that of nickel, the reduction process is accelerated as the temperature is increased. Also, as the temperature is increasing, the nanoparticles nucleate and create an autocatalytic reaction which further affects the reduction rate of the MOD precursor inks.

The formation of layered nanostructures show potential in printed electronics applications. Copper is an excellent electrical conductor while nickel is highly resistant to rusting and corrosion. The two phased structure with copper at the bottom and nickel rich alloy at the surface could be

used as an electrode in oxidative environment. The electrical properties of the copper, nickel and copper nickel alloy were characterized by measuring the change in resistance of the sintered sample after exposing to oxygen rich atmospheric plasma.

A solid square film (1 cm × 1 cm) was printed with copper, nickel and alloy MOD ink on a glass substrate using a Fuji Dimatix inkjet printer (DMP 3000). The samples were sintered in a vacuum furnace at 230 °C for 30 min with a ramp up rate of 2 °C/min. The sintered film was exposed to an O_2 plasma using a Surfx Atomflo™ 400 atmospheric plasma system. This system generates plasma using a helium-oxygen gas mixture to create an oxidizing environment. The plasma head was mounted on a linear stage to move on command in the X and Y directions. The Z height between the sample and the head (i.e standoff distance) was kept constant at 10 mm. For each pass, the power of the plasma was set to 100 W. Helium and oxygen gas flow rates of 15.00 l/min and 0.30 l/min respectively were used. The resistance was measured across the sintered sample after every ten passes of the oxygen plasma. Figure 3-13 shows the change in relative resistance of the printed film with exposure to O_2 plasma. As expected, the relative resistance of the sintered copper increased due to oxidization as the number of passes was increased. In contrast, the relative resistance of the nickel and copper nickel alloy samples was not affected by the oxidizing environment. The nickel rich alloy encapsulating the copper prevents the copper from oxidation. This demonstrated ability of the nanoalloy structure to maintain conductivity in a strongly corrosive or oxidative environment suggests numerous potential applications in electronics.
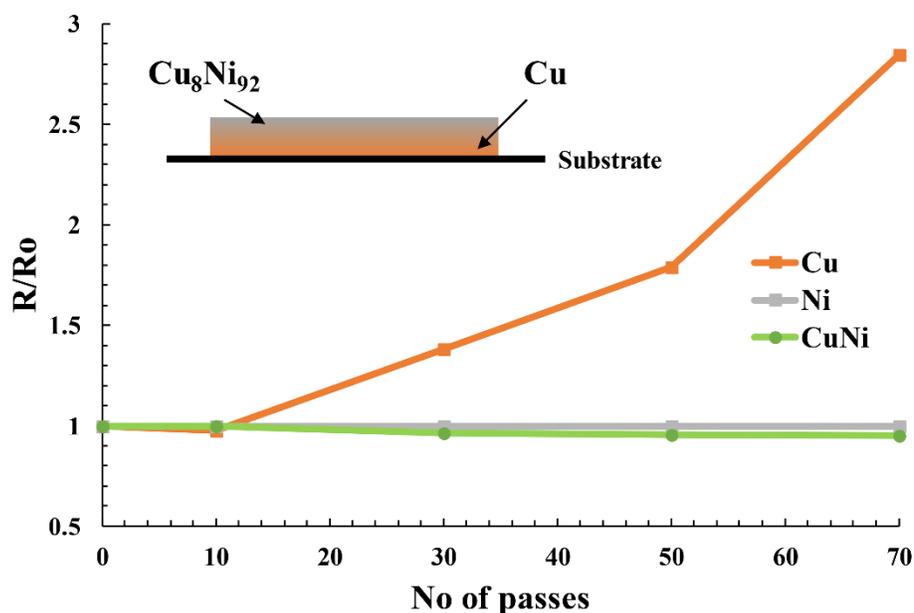
Figure 3-13: Measured change of resistance in printed film on exposure to oxygen plasma. Reproduced from [22] licensed under CC by 4.0

3.6. Summary

Copper and nickel precursor inks were formulated using metal formate salts, ethylenediamine, and ethylene glycol. The reduction process of copper, nickel and combined solutions was studied in detail. EDS elemental mapping shows the reduction of alloy ink with well mixed copper and nickel. Sintering on magnetic hotplate results in segregation since nickel particles are attracted to each other in presence of the magnetic field. No segregations were observed for samples sintered in vacuum and in inert atmosphere. XRD analysis of the sintered alloy in vacuum furnace shows the presence of two phases, copper and bimetallic copper-nickel. DTA analysis for the alloy MOD ink confirmed the reduction of copper first followed by reduction of nickel rich alloy on top of copper. Sintering of the alloy ink resulted in the formation of a copper film on the substrate that was encapsulated by nickel-rich alloy. The lattice parameter for the

69

sintered alloy was 3.5318 Å, indicating the average composition of the bimetallic alloy to be Cu_8Ni_{92}. In order to explore the electrical properties of the layered nanostructure, the relative resistance change in an oxidizing environment was observed for sintered copper, nickel and copper nickel alloy film. After several passes of oxygen plasma treatment, the nanoalloy film demonstrated no change in resistivity values, making the copper-nickel nanoalloy film suitable as an electrical conductor in oxidizing environments.

This study confirms the basic feasibility of mixing individual elemental MOD precursor inks to form a nanoalloy. The copper and nickel show uniform distribution along a 2D plane but XRD shows presence of two phases along the thickness. In order to make a 3D part with desired alloy composition, such structures are not preferred. To achieve homogenous alloy formation throughout the sample, the copper at the core needs to diffuse into the nickel rich alloy. The next chapter focuses on approaches to diffuse the copper from the core into the nickel rich alloy to achieve homogenous alloy formation. The formation of alloy by mixing of copper and nickel inks in desired proportions using inkjet printing technique and the degree of mixing following jetting from different nozzle is also described.

3.7. References

[1]   H. Reichenbach and P. McGinn, "Combinatorial synthesis of oxide powders," *Journal of Materials Research,* vol. 16, no. 4, pp. 967-974, 2001.

[2]   S. Okamura, R. Takeuchi, and T. Shiosaki, "Fabrication of ferroelectric Pb (Zr, Ti) O3 thin films with various Zr/Ti ratios by ink-jet printing," *Japanese journal of applied physics,* vol. 41, no. 11S, p. 6714, 2002.

[3]   W. A. Badawy, K. M. Ismail, and A. M. Fathi, "Effect of Ni content on the corrosion
        behavior of Cu–Ni alloys in neutral chloride solutions," *Electrochimica acta,* vol. 50, no.
        18, pp. 3603-3608, 2005.

[4]   H. Kim, C. Lu, W. Worrell, J. Vohs, and R. Gorte, "Cu-Ni cermet anodes for direct
        oxidation of methane in solid-oxide fuel cells," *Journal of the Electrochemical Society,*
        vol. 149, no. 3, pp. A247-A250, 2002.

[5]   R. Qiu, X. L. Zhang, R. Qiao, Y. Li, Y. I. Kim, and Y. S. Kang, "CuNi dendritic material:
        synthesis, mechanism discussion, and application as glucose sensor," *Chemistry of
        materials,* vol. 19, no. 17, pp. 4174-4180, 2007.

[6]   W. Qiwu, Y. Jianlong, R. Jingfang, H. Minming, and Y. Chunhua, "Structure and
        catalytic properties of Cu-Ni bimetallic catalysts for hydrogenation," *Catalysis letters,*
        vol. 4, no. 1, pp. 63-74, 1990.

[7]   S. A. Hashemizadeh and M. Biglari, "Cu: Ni bimetallic nanoparticles: facile synthesis,
        characterization and its application in photodegradation of organic dyes," *Journal of
        Materials Science: Materials in Electronics,* pp. 1-7, 2018.

[8]   A. A. Kuznetsov *et al.*, "Local radiofrequency-induced hyperthermia using CuNi
        nanoparticles with therapeutically suitable Curie temperature," *Journal of Magnetism and
        Magnetic Materials,* vol. 311, no. 1, pp. 197-203, 2007.

[9]   W. Songping, J. Li, N. Jing, Z. Zhenou, and L. Song, "Preparation of ultra fine copper–
        nickel bimetallic powders for conductive thick film," *Intermetallics,* vol. 15, no. 10, pp.
        1316-1321, 2007.

[10]   J. Ahmed *et al.*, "Bimetallic Cu–Ni nanoparticles of varying composition (CuNi3, CuNi, Cu3Ni)," *Colloids and Surfaces A: Physicochemical and Engineering Aspects,* vol. 331, no. 3, pp. 206-212, 2008.

[11]   J. Feng and C.-P. Zhang, "Preparation of Cu–Ni alloy nanocrystallites in water-in-oil microemulsions," *Journal of colloid and interface science,* vol. 293, no. 2, pp. 414-420, 2006.

[12]   S. Souilah, S. Alleg, M. Bououdina, J. Sunol, and E. Hlil, "Magnetic and structural properties of the nanostructured Cu50Ni50 powders," *Journal of Superconductivity and Novel Magnetism,* vol. 30, no. 7, pp. 1927-1935, 2017.

[13]   J. Chatterjee, M. Bettge, Y. Haik, and C. J. Chen, "Synthesis and characterization of polymer encapsulated Cu–Ni magnetic nanoparticles for hyperthermia applications," *Journal of magnetism and magnetic materials,* vol. 293, no. 1, pp. 303-309, 2005.

[14]   F. Bonet, S. Grugeon, L. Dupont, R. H. Urbina, C. Guery, and J. Tarascon, "Synthesis and characterization of bimetallic Ni–Cu particles," *Journal of Solid State Chemistry,* vol. 172, no. 1, pp. 111-115, 2003.

[15]   L. Chen, H. Xu, H. Cui, H. Zhou, H. Wan, and J. Chen, "Preparation of Cu–Ni bimetallic nanoparticles surface-capped with dodecanethiol and their tribological properties as lubricant additive," *Particuology,* vol. 34, pp. 89-96, 2017.

[16]   C.-H. Jung, H.-G. Lee, C.-J. Kim, and S. Bhaduri, "Synthesis of Cu–Ni alloy powder directly from metal salts solution," *Journal of nanoparticle research,* vol. 5, no. 3-4, pp. 383-388, 2003.

[17] E. Pál *et al.*, "Composition-dependent sintering behaviour of chemically synthesised CuNi nanoparticles and their application in aerosol printing for preparation of conductive microstructures," *Colloid and Polymer Science,* vol. 290, no. 10, pp. 941-952, 2012.

[18] E. Pál, V. Zöllmer, D. Lehmhus, and M. Busse, "Synthesis of Cu 0.55 Ni 0.44 Mn 0.01 alloy nanoparticles by solution combustion method and their application in aerosol printing," *Colloids and Surfaces A: Physicochemical and Engineering Aspects,* vol. 384, no. 1, pp. 661-667, 2011.

[19] D. S. Ginley, C. J. Curtis, A. Miedaner, M. F. A. M. Van Hest, and T. Kaydanova, "Metal inks," ed: Google Patents, 2014.

[20] Y. Farraj, M. Grouchko, and S. Magdassi, "Self-reduction of a copper complex MOD ink for inkjet printing conductive patterns on plastics," *Chemical Communications,* vol. 51, no. 9, pp. 1587-1590, 2015.

[21] T. Yamauchi *et al.*, "Magnetic Cu–Ni (core–shell) nanoparticles in a one-pot reaction under microwave irradiation," *Nanoscale,* vol. 2, no. 4, pp. 515-523, 2010.

[22] C. G. Mahajan *et al.*, "Formation of Copper Nickel Bimetallic Nanoalloy Film Using Precursor Inks," *Materials Sciences and Applications,* vol. 10, no. 4, 2019.

[23] E. V. Shevchenko *et al.*, "Study of nucleation and growth in the organometallic synthesis of magnetic alloy nanocrystals: the role of nucleation rate in size control of CoPt3 nanocrystals," *Journal of the American Chemical Society,* vol. 125, no. 30, pp. 9090-9101, 2003.

[24] R. Butera and D. Waldeck, "X-ray diffraction investigation of alloys," *J. Chem. Educ,* vol. 74, no. 1, p. 115, 1997.

[25]   S. Gupta, "Peak decomposition using Pearson type VII function," *Journal of applied crystallography,* vol. 31, no. 3, pp. 474-476, 1998.

[26]   B. D. Cullity, "Elements of X-ray Diffraction," 1978.

[27]   H. Eyring, "The activated complex and the absolute rate of chemical reactions," *Chemical Reviews,* vol. 17, no. 1, pp. 65-77, 1935.

[28]   L. F. Hamilton, S. G. Simpson, and D. W. Ellis, "Calculations of analytical chemistry-7," 1969.

[29]   W. Zhang *et al.*, "Progress and perspective of electrocatalytic CO2 reduction for renewable carbonaceous fuels and chemicals," *Advanced Science,* vol. 5, no. 1, p. 1700275, 2018.

Chapter 4 Digital Alloying Using Precursor Inks

4.1. Introduction

As described in the previous chapter, when the copper-nickel mixture ink was reduced at appropriate temperatures, a two phased structure formed within a copper-nickel alloy film. Although such copper nickel structures are useful as conductors in oxidizing environments, to achieve the desired homogenous alloy film, the copper phase needs to be diffused in the nickel rich alloy. The diffusion of atoms is dependent upon temperature, concentration, diffusion distance and time. This chapter describes a high-temperature diffusion process aimed at achieving the desired copper-nickel alloy composition.

4.2. Inkjet printing of copper and nickel inks

To study the degree of mixing following jetting of individual metal inks, the Cu and Ni MOD inks described in the previous chapter were printed onto a substrate using a Fuji Dimatix inkjet printer (DMP 3000). The printer uses a piezoelectric ink cartridge having a single row of 16 nozzles to dispense the ink with a drop volume of 10 pl onto a substrate. The print head temperature and the voltage were adjusted for individual inks before printing. The copper and nickel MOD precursor inks were filtered through a 0.2 µm syringe filter before loading into separate ink cartridges. Substrates were cleaned with IPA and treated with atmospheric plasma to increase the wettability of the inks. A 5 mm square was printing with drop spacing of 20 µm for each layer. The inks were dispensed onto a substrate in the desired layer ratios (Cu:Ni → 1:4, 2:3, 3:2, and 4:1). For e.g.: In layer ratio of Cu:Ni →1:4, one layer of copper ink was printed onto the substrate and then the nickel ink cartridge was loaded into the printer and four layers of nickel ink were

printed on top of the copper layer. The final printed film was reduced in a vacuum furnace at 230 °C at 10 °C/ min for 30 min as shown in Figure 4-1.
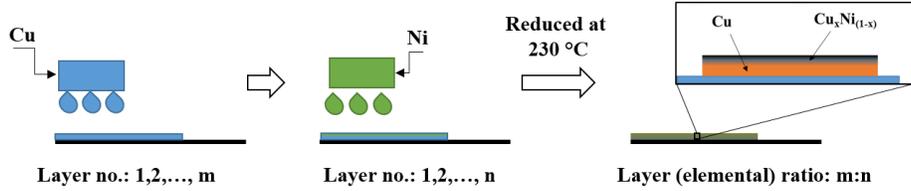
Figure 4-1: Inkjet printing of copper and nickel ink onto a substrate with desired layer ratio

To analyze the degree of mixing after the reduction of copper and nickel to their elemental states, EDS elemental mapping analysis was performed on the sintered samples. The EDS elemental mapping (Figure 4-2) shows a uniform distribution of the reduced copper and nickel. No segregation between reduced copper and nickel was observed in the reduced film. This confirmed the mixing of copper and nickel following the jetting and sintering processes along the two dimensions (X and Y). However as seen in the previous chapter, phases of copper and copper-nickel alloy can be present along the thickness of the film (Z dimension). To diffuse the copper phase into the nickel-rich copper nickel alloy, factors such as time and temperature must be considered. The following section highlights the equations governing elemental diffusion at high temperatures.
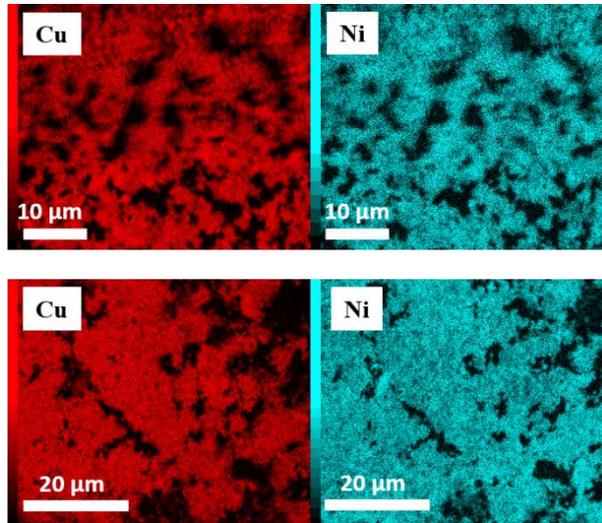
Figure 4-2: EDS elemental mapping of reduced films by printing individual metal precursor inks using inkjet printing

4.3. High temperature diffusion

Diffusion is a mass flow process by which species change their position relative to their neighbors. Diffusion in metals plays an important role in the formation of a homogeneous alloy (consisting of a single phase). The equations governing diffusion come from Fick's first and second laws. Adolf Fick [1] proposed the laws of diffusion in steady and unsteady state conditions. In steady state conditions, the concentration is independent of time whereas in unsteady state conditions, the concentration changes with time. Fick's first law states that in steady state conditions, the flux of particles (atoms, molecules, ions, etc.) in a one dimensional system is proportional to the concentration gradient and is expressed as

$$J = -D\frac{\partial C}{\partial x} \qquad \text{Eq. 4.1}$$

Where J is the flux (mol/m².s), D is the diffusivity or diffusion coefficient (m²/s), C is the concentration of the particles (mol/m³), and x is the position parameter (m). The negative sign indicates that the diffusion occurs in the direction opposite to the increasing concentration gradient.

The diffusivity is highly temperature dependent and has important consequences with regard to material behavior at elevated temperatures. Diffusivity in solids increases exponentially with the temperature and is given by

$$D = D_0 exp^{(\frac{-Q}{RT})}$$

Eq. 4.2

Where D_0 is the maximal diffusivity or maximal diffusion coefficient (m²/s), Q is the activation energy (J/mol), R is the universal gas constant ($R = 8.31$ J/ (mol-K)) and T is the absolute temperature (K). For the copper nickel alloy system, the maximal diffusion coefficient of Cu in Ni $= D_0 = 2.7*10^{-5}$ m²/sec, and the activation energy for diffusion of Cu in Ni $= Q = 256$ kJ/mol [2].

Fick's first law applies only in a steady state condition where the concentration does not change with time. However, under most experimental conditions, the concentration at a particular position changes with time. For such conditions, Fick's first law cannot be used to determine the diffusion coefficient because it does not have a time parameter. Fick's second law of diffusion is derived using the first law and mass conservation. It considers the change in concentration at a particular position with increasing time and is written as

$$\frac{\partial C}{\partial t} = D \frac{\partial^2 C}{\partial x^2}$$

Eq. 4.3

The solution of the above differential equation is the concentration at any point x in time t and it depends upon the initial and boundary conditions. One of the solutions for the above differential equation is the error function solution given by [3]

78

$$C(x,t) = A - B\left(erf\left(\frac{x}{2\sqrt{D*t}}\right)\right)$$

Eq. 4.4

Where constants A and B can be found out by based on the initial and boundary conditions. For maximum diffusion, the error function is equal to 1.

$$erf\left(\frac{x}{2\sqrt{D*t}}\right) = 1$$

Eq. 4.5

The values of $erf(z)$ as a function of z is available in the literature [3]. For $erf(z) = 1$, $z \approx 3$.

$$\left(\frac{x}{2\sqrt{D*t}}\right) \approx 3$$

Eq. 4.6

$$t \approx \frac{x^2}{36\,D}$$

Eq. 4.7

The diffusivity depends upon the chemistry of the sample as well as the microstructure [4]. The position parameter x can be considered as the thickness of the film assuming the film is dense enough to diffuse the atoms into each other. Factors such as dislocations and grain boundaries are not considered to calculate the time required for diffusion. Based on Eq. 4.2 and Eq. 4.7, the approximate time required to diffuse copper and nickel into each other at a specific temperature for a given thickness of the film can be calculated.

Table 4.1 shows the time require to diffuse the copper into nickel for diffusion distances of 0.1 µm, 1 µm and 10 µm at different temperatures. The diffusion time decreases as sintering temperature increases. Diffusion time obviously decreases as the diffusion distance decreases. It is important to emphasize that diffusion distance is not necessarily the same as the overall thickness of material. If each printing pass lays down 0.5 µm thickness, and many print passes are used to

build up thickness of perhaps 10 mm of material, then each printed layer has both Cu and Ni in the correct proportions. In the worst case, the diffusion distance needed to homogenously distribute the Cu and Ni atoms is equal to the layer thickness in the vertical direction and the drop spacing in the lateral (X-Y) direction. Assuming some mixing and drop overlap of Cu and Ni during printing, the diffusion distance will be less than the vertical layer thickness and the horizontal drop spacing.

Table 4-1: Time require to diffuse copper from the core into nickel at the surface

Temperature to diffuse Cu into Ni (°C)	Thickness of the film (μm)		
	0.1 μm	**1 μm**	**10 μm**
700 °C	~ 9.6 min	~ 964 min	~ 96477 min
750 °C	~ 2.1 min	~ 205 min	~ 20529 min
800 °C	~ 0.5 min	~ 50 min	~ 5046 min
850 °C	~ 0.1 min	~ 14 min	~ 1405 min

To form a homogeneous alloy of copper and nickel, high temperature diffusion was carried out on printed and reduced samples. The samples were printed on a silicon wafer (crystal orientation: 100) to withstand the high temperature sintering. A similar printing scheme was carried out as described in Figure 4-1. A layer of copper was printed followed by a layer of nickel. The samples were reduced first at 230 °C for 30 minutes in a vacuum furnace. Good film formation was observed on a silicon wafer. The samples were later placed in a vacuum furnace at 800 °C for 8 hours at 50 °C/min. The sintered samples show copper separating out to form nanowires on the substrate as seen in Figure 4-3. No such separations were observed at lower temperatures (230 °C) where the copper and nickel precursor inks reduce. It is hypothesized that the reduced copper

diffuses along crystal lattice lines at high temperatures (800 °C). To avoid such segregations of copper at high temperatures, a single crystal quartz substrate (X-cut - 110) was used.
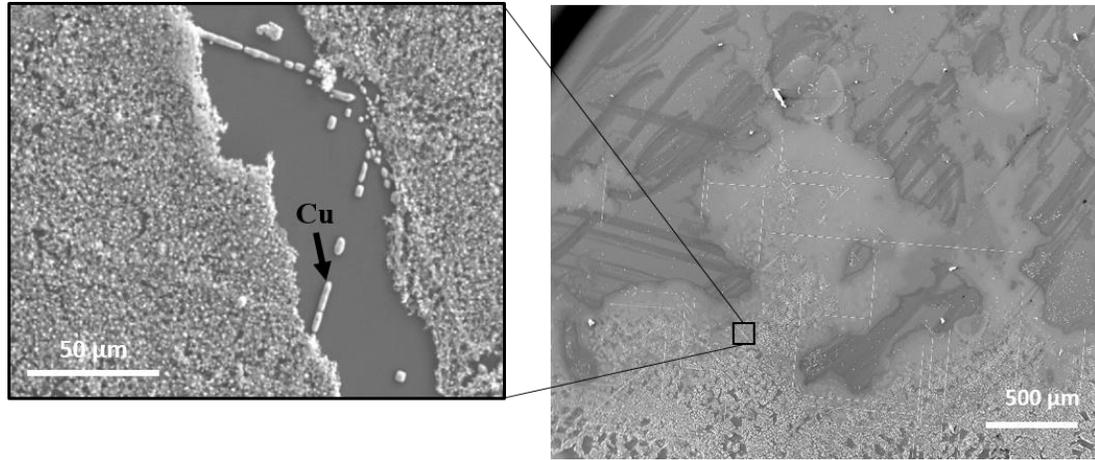
Figure 4-3: Diffusion of copper in silicon at high temperatures

The samples sintered on single crystal quartz didn't exhibit separation of the copper as observed on the Si wafer. The copper and nickel showed uniform distribution in the EDS elemental mapping. However, the sintered sample had a high degree of porosity as seen in Figure 4-4. Small cubic structures were formed on the substrate which suggests the formation of microstructures due to solid state dewetting at elevated temperature. Also, the pores generated during the reduction process are more apparent at high temperatures.
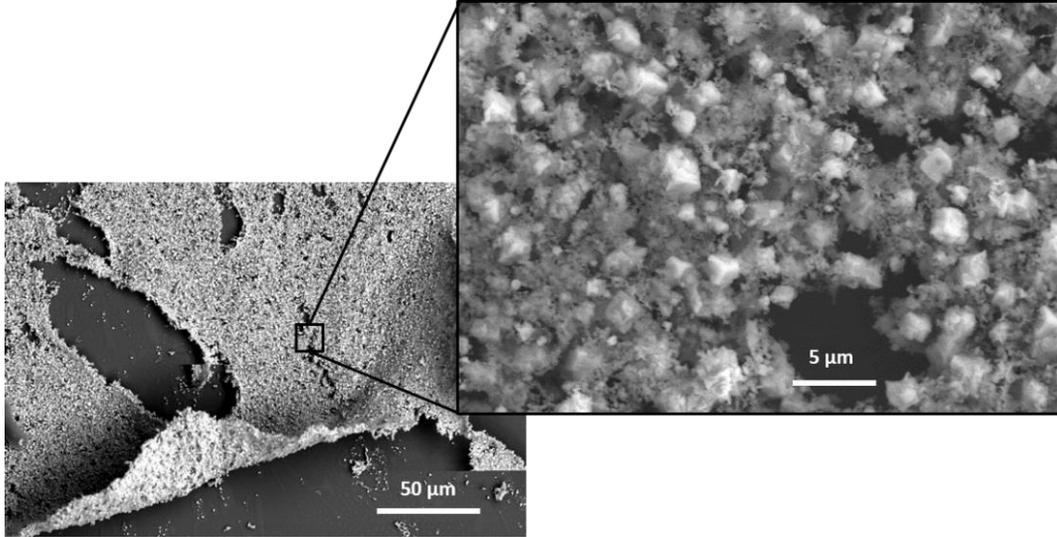
Figure 4-4: High temperate sintering on single crystal quartz substrate

To minimize the porosity in the film, the ink was reduced after printing each layer. The next layer was printed on top of the previously cured layer. This process helped in filling the pores generated during the reduction process at lower temperatures. The nickel layers were reduced at 230 °C while the copper layers were reduced at 170 °C. The schematic of the process is shown in Figure 4-5. Five layers (Ni → Cu → Ni → Cu → Ni) were printed and sintered at the appropriate reducing temperatures. This case generated a sandwich like pattern with alternate copper and nickel layers. The final film thickness of the pattern was around 3 μm. The alternate printing and reducing helped in generating a dense film of metallic copper and nickel as seen in Figure 4-6.
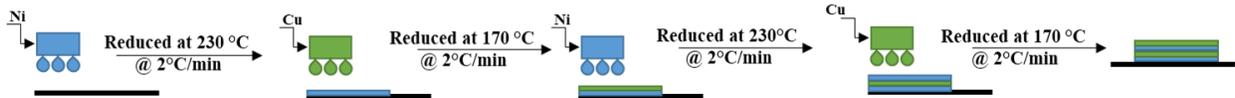
Figure 4-5: Schematic illustration of alternate printing and reducing of the metallic layers

The sample was placed in a vacuum furnace for 8 hours at 800 °C. Figure 4-6 shows the film before and after sintering at high temperature. Large numbers of small islands of copper nickel

alloy were formed on the substrate. The EDS elemental mapping confirms that the islands consist of both copper and nickel (Figure 4-7). Dewetting of the alloy film was observed where the film agglomerated to form microstructures. This phenomenon is called solid state dewetting where thin solid films on a substrate tend to agglomerate to form island when heated to high temperatures [5]. This process is driven by surface energy minimization and occurs while the film remains in a solid state. Although solid state dewetting is undesirable, there has been research to use such structures to make sensors [6] and to grow carbon nanotubes [7].
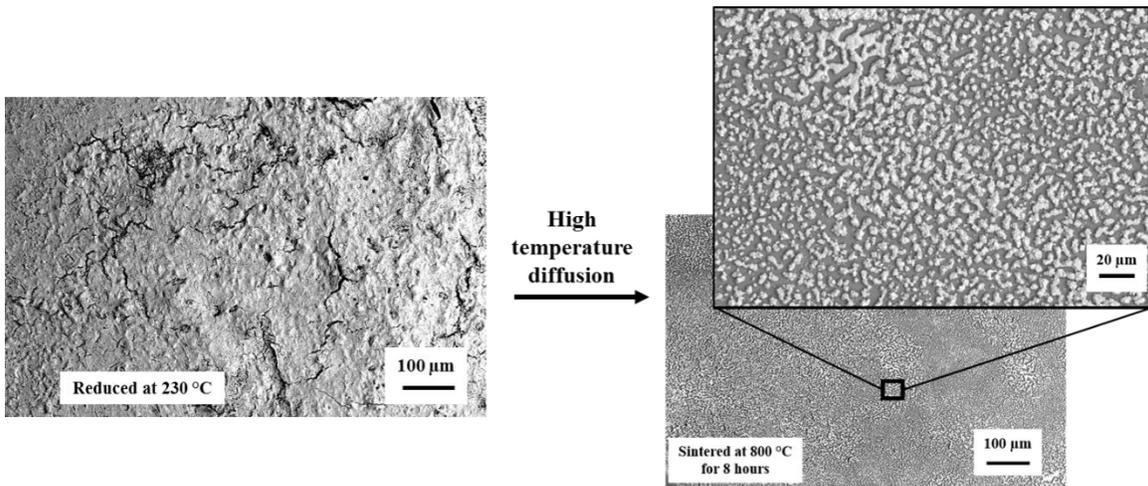
Figure 4-6: Sintered copper nickel alloy film at 230 °C and at 800 °C
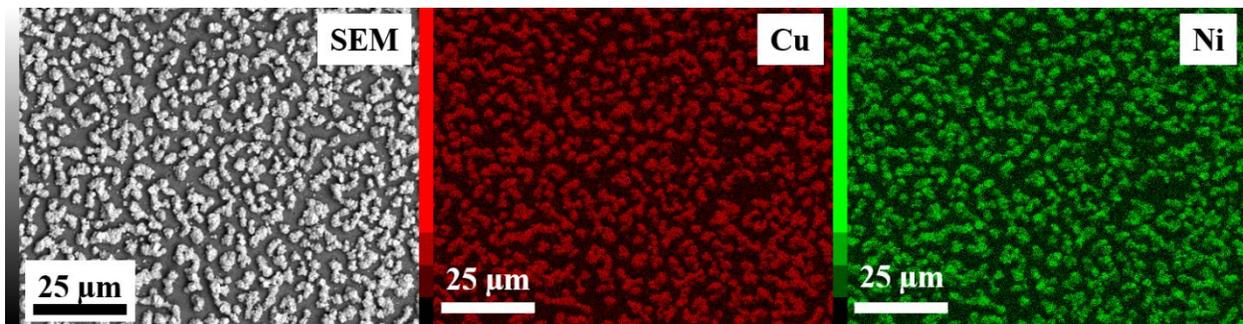
Figure 4-7: EDS elemental mapping of copper nickel film on quartz substrate sintered at high temperature

The solid state dewetting can be controlled by different techniques such as by increasing the film thickness, using a capping layer to suppress the effect, and depositing foreign materials on the substrate [8]. Since the solid state dewetting phenomenon cannot be avoided at high temperatures, the film before the diffusion should be sufficiently dense and thick. To verify this concept, an experiment was carried where copper nickel alloy inks were formulated with different ratios ($Cu_{30}Ni_{70}$, $Cu_{50}Ni_{50}$, and $Cu_{70}Ni_{30}$) and were drop cast onto glass substrates. The samples were heated at 230 °C with a ramp up rate of 10 °C/min in a vacuum furnace for 30 min to create a reduced nanoalloy film of copper-nickel. The film was scrapped off the substrates and collected in a crucible. The powder was pressed onto a quartz substrate to create a one-millimeter thick dense film. The samples were further sintered at 800 °C for 8 hours in a vacuum furnace to achieve high temperature diffusion. Figure 4-8 shows the schematic illustration of the process.
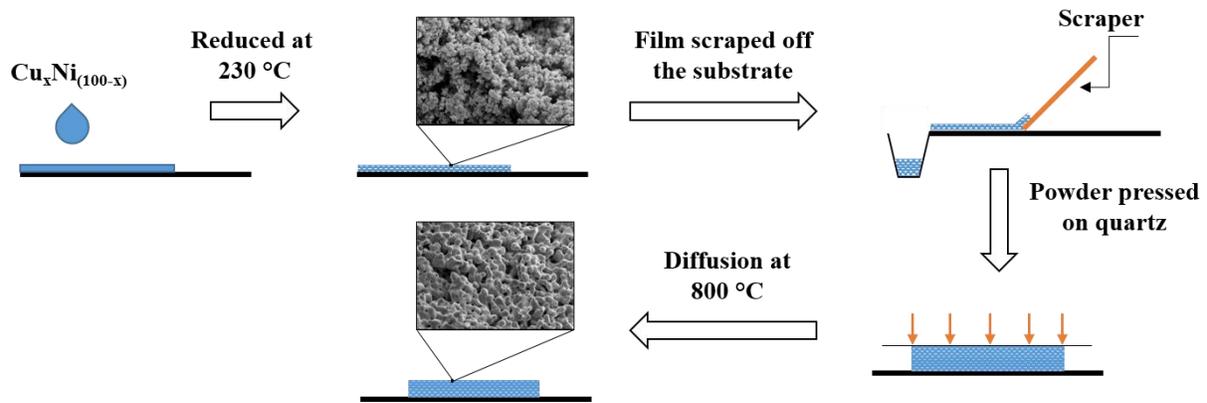
Figure 4-8: Process description to form copper nickel alloy powder and achieve diffusion between copper and nickel at high temperature

The final sintered film shows the particles are well connected to each other with less porosity compared to samples reduced at 230 °C. XRD diffraction patterns of the sintered sample show the crystalline phase of copper nickel alloy. Small peaks of CuO and NiO were observed in the diffraction pattern for samples with ratio $Cu_{30}Ni_{70}$ and $Cu_{70}Ni_{30}$. A small amount of pure copper

contaminant was present in the sample with ratio $Cu_{30}Ni_{70}$ as indicated by a single peak of Cu (111).
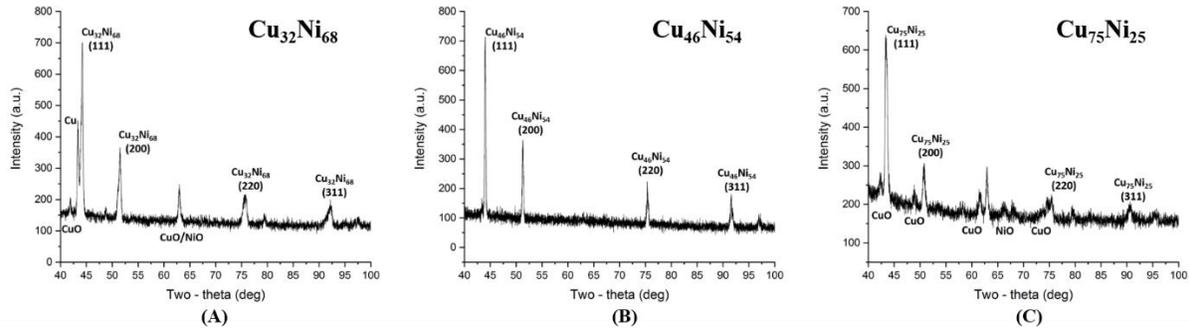
Figure 4-9: XRD diffraction patterns of the sintered sample with different compositions

The lattice parameter of the alloy phase for the inks with ratio $Cu_{30}Ni_{70}$ was 3.5533Å, $Cu_{50}Ni_{50}$ was 3.5658 Å, and $Cu_{70}Ni_{30}$ was 3.5921 Å. Using Vegard's law, the composition of the alloy phases for the three samples were estimated to be $Cu_{32}Ni_{68}$, $Cu_{46}Ni_{54}$, and $Cu_{75}Ni_{25}$. The calculations to determine the lattice parameter and compositions of alloy phase are presented in APPENDIX – A. These values were deemed to be reasonably close to the theoretical elemental composition of the MOD precursor inks used. There were different factors which may have affected the change in the alloy composition. The precursor ink ratio was determined using the weight percentage obtained using the TGA analysis. Small contaminate in the ink ingredients (salt, ethylenediamine, and ethylene glycol) may have affected the final weight percentage of elemental copper or nickel. The reduced film was scrapped from the substrate to obtain it in a powder form. Some of the metal particles may have not been completely transferred onto the final dense thick film. Also, the alloy ratio was determined using Vegard's law which is dependent on the peak position of the diffraction pattern in the XRD. The peaks could have shifted by a small degree due to strain in the sample which may have changed the calculation of alloy composition.

85

4.4. 3D printing workflow

The high temperature diffusion on the reduced film shows the potential of controlling alloy composition by dispensing known proportions of elemental inks. To print a part with desired alloy composition, each layer can be printed and reduced over and over to build up a 3D structure. The final printed 3D part can be placed in a high temperature furnace to achieve diffusion and form a homogenous alloy structure. As the weight percentage of copper and nickel in the precursor inks presented were 6.5% and 4.5 % respectively, the number of printing and reducing steps increases to print a 3D part. The printing time can be reduced by increasing the drop volume of the ink or by increasing the solid content of the ink.

4.5. Summary

The copper and nickel MOD precursor inks were inkjet printed onto a substrate to study the degree of mixing after jetting. The EDS analysis confirmed a uniform distribution of copper and nickel in the reduced film. To avoid a two phase structure in final sintered film, high temperature diffusion was carried out to create a homogenous alloy film. Challenges such as high porosity in the sintered film and solid state dewetting at high temperatures were encountered during the diffusion process. To resolve some of the challenges experienced from high temperature diffusion process, the thickness and density of the reduced film was increased. Copper nickel alloy inks with ratios $Cu_{30}Ni_{70}$, $Cu_{50}Ni_{50}$, and $Cu_{70}Ni_{30}$ were formulated and reduced at 230 °C and later high temperature diffusion was achieved at 800 °C. The XRD pattern confirmed the presence of a crystalline phase of copper nickel alloy in the sintered film. The lattice parameter of the alloy phase for the inks with ratio $Cu_{30}Ni_{70}$ was 3.5533Å, $Cu_{50}Ni_{50}$ was 3.5658 Å, and $Cu_{70}Ni_{30}$ was 3.5921 Å. Using Vegard's law, the composition of the alloy phases for the three samples were estimated to be $Cu_{32}Ni_{68}$, $Cu_{46}Ni_{54}$, and $Cu_{75}Ni_{25}$.

4.6. References

[1]   A. Fick, "Ueber diffusion," *Annalen der Physik,* vol. 170, no. 1, pp. 59-86, 1855.

[2]   E. A. Brandes and G. Brook, *Smithells metals reference book*. Elsevier, 2013.

[3]   A. Paul, T. Laurila, V. Vuorinen, and S. V. Divinski, *Thermodynamics, diffusion and the Kirkendall effect in solids*. Springer, 2014.

[4]   H. Mehrer, *Diffusion in solids: fundamentals, methods, materials, diffusion-controlled processes*. Springer Science & Business Media, 2007.

[5]   C. V. Thompson, "Solid-state dewetting of thin films," *Annual Review of Materials Research,* vol. 42, pp. 399-434, 2012.

[6]   J. Mizsei, "Activating technology of SnO2 layers by metal particles from ultrathin metal films," *Sensors and Actuators B: Chemical,* vol. 16, no. 1-3, pp. 328-333, 1993.

[7]   M. Chhowalla *et al.*, "Growth process conditions of vertically aligned carbon nanotubes using plasma enhanced chemical vapor deposition," *Journal of applied physics,* vol. 90, no. 10, pp. 5308-5317, 2001.

[8]   F. Leroy *et al.*, "How to control solid state dewetting: A short review," *Surface Science Reports,* vol. 71, no. 2, pp. 391-409, 2016.

Chapter 5 Nanowire Formation with Ni MOD Ink

5.1. Introduction

In functional printing, metallic inks are most commonly used to produce features intended to conduct electricity (e.g. printed electronics [1]) or heat (e.g. printed heaters [2]). For magnetic devices, transition metals such as Fe, Co and Ni are widely used due to their ferromagnetic properties. Despite the intense interest in printing metal containing inks, there have been very few examples of printing ferromagnetic metals. Among these, Ni is mainly used due to its corrosion resistance, good electrical conductivity, high magnetic permeability, high thermal coefficient of resistance, and relatively high saturation magnetization [3, 4]. As seen in Chapter 3, in the process of reduction, nickel particles were attracted to each other in the presence of a magnetic field. In this chapter, the ferromagnetism of nickel was used to align nickel nanoparticles in the direction of the magnetic field to create patterned nanowires on a substrate.

Ni nanoparticles and nanowires have been formulated with different techniques such as hydrothermal processing [3, 5, 6], chemical reduction [7-9] and electrochemical deposition [10]. However, the methods to fabricate, deposit, and/or align the nanowires onto desired substrates typically requires multiple steps, large quantities of electrically or functionally inactive materials (templates) and extreme conditions. For example, the reduction of Ni to its elemental state can be achieved in a stainless-steel autoclave and must be followed by washing and drying of the nanowires in an inert atmosphere to avoid oxidation [3, 5, 7, 9].

Deposited nanowires containing Ni have many applications including Surface Enhanced Raman Spectroscopy (SERS) [11, 12], magnetic data storage [13, 14] and giant magnetoresistive sensors [15-18]. These magnetic applications exploit the fact that the large shape anisotropy generated from the high aspect ratio of nanowires provides high intrinsic coercivity. Aligned

nanowires on surfaces can also be useful for optical applications such as nanowire polarizers [19, 20], and for many biological purposes, for example "lab on a chip" devices, as well as for the construction of tubular sensors which exploit geometrically induced circumferential magnetization [21], or for cell guidance using tissue or organ like structures in vitro [22]. Therefore, it is of great significance to develop a practical approach to fabricating nanowires having the desired orientation directly onto the preferred substrate.

In this chapter, a Ni precursor ink was synthesized in ambient conditions such that the ink can be thermally reduced to elemental nickel after printing. This homogeneous ink can be formulated for many different printing and deposition processes. The ink was printed on different substrates using an aerosol printing technique. The reduction of Ni was observed in the presence and absence of a magnetic field. Interestingly, reduction in the presence of a magnetic field produced pure, template free, aligned Ni nanowires. In this way, large areas of aligned Ni nanowires were produced, using only weak magnetic fields. It is believed that this novel method is the first example of aligned nanowire formation on a surface by a thermal reduction (curing/sintering) process. Moreover the reaction is simple and the byproducts are volatile, leaving quantitatively pure Ni nanowires, without the need for further purification. The electrical and magnetic properties are enhanced in the direction of the aligned Ni nanowires. The film morphology can be easily manipulated during the reduction process to produce a number of different novel structures having unique electronic and magnetic properties. Figure 5-1 shows a schematic illustration of printing a Ni precursor ink and reducing it in the presence of homogeneous magnetic field to produce aligned nanowires.
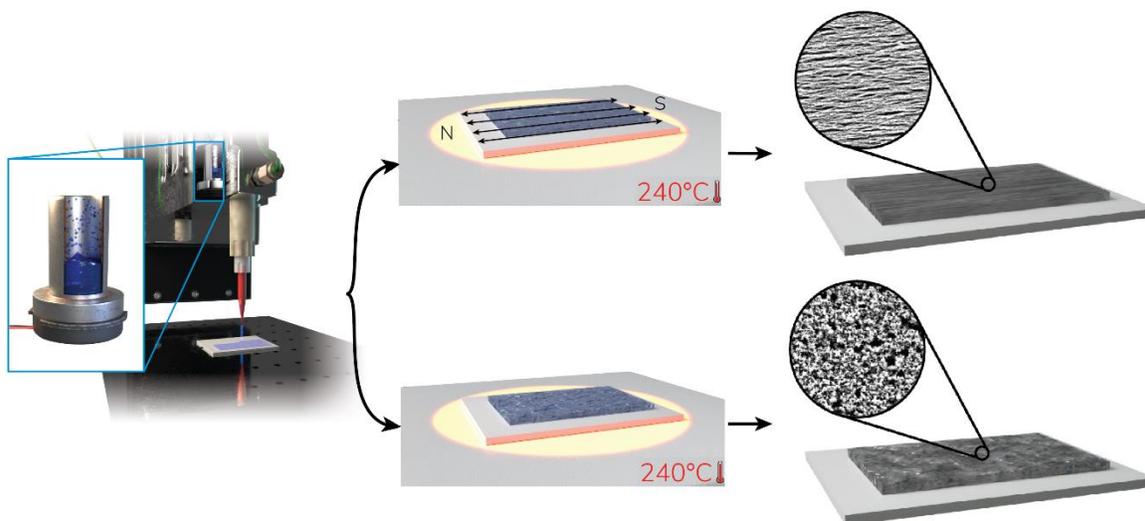
Figure 5-1: Schematic illustration of printing a Ni precursor ink and sintering it in presence of homogeneous magnetic field to reduce the nickel complex to aligned nanowires. Reproduced from [23] licensed under CC by 4.0

5.2. Ink formulation

To realize the formation of nanostructures during reduction of the Ni MOD ink, the ink formulation was modified from the one presented in Chapter 3. The same metal salt (nickel formate) and ligand (ethylenediamine) were used. The solvent was changed from ethylene glycol to water to reduce the viscosity of the ink. Ethylenediamine (0.72 ml, 10.77 mmol) was dissolved in 4 ml of distilled water. Nickel formate (0.8 g, 5.38 mmol) was added to this solvent mixture and stirred at room temperature for 15 minutes. The ink was filtered through a 0.2 µm syringe filter. Other additives such as 1% w/w of Polyvinylpyrrolidone (MW: 3500, K 12) and 20 µl of BYK 333 surfactant (10% v/v solution in distilled water) were added to the filtered mixture. Surface tension of the Ni ink was measured using a contact angle goniometer and tensiometer (Model 250, Ramé-Hart, USA) using the pendant drop method. The viscosity of the ink was measured using a microVISC viscometer (RheoSense, USA). The surface tension and viscosity of the ink were 44.01 mN/m and 3.2 cP, respectively.

5.3. Ink characterization

The Ni ink contains nickel formate complexed with ethylenediamine, which undergoes a thermal reduction process to generate metallic Ni on the desired substrate following printing and curing. The use of formate counter ions decreases the mass of the organic content of the complex, provides a relatively low decomposition temperature, and subsequently decreases the residue following decomposition [24]. Furthermore, as described in Chapter 3, the decomposition of nickel formate is accompanied by the release of carbon oxides and molecular hydrogen [25], which contribute to the reducing atmosphere thus preventing the oxidation of Ni. The bidentate ethylenediamine has been used in the formation of the metal complex to enhance the reduction efficiency, achieve complex stability and increase complex solubility in water [26].

Thermogravimetric analysis (TGA) and differential thermal analysis (DTA) (Shimadzu DTG -60, Japan) were performed by heating the ink sample in an aluminum pan from room temperature to 400 °C at 10 °C/ minute. The TGA of the Ni ink shows that the thermal decomposition occurs in two stages (Figure 5-2, dashed black line). The first stage includes the solvent evaporation up to 100 °C, and the second stage involves the reduction of Ni to its elemental state at 235 °C. The final amount of Ni in the ink was 5.7 % w/w. According to DTA data (Figure 5-2, solid red line), the first endothermic peak was observed around 80 °C with corresponding mass loss indicating the solvent evaporation while the last endothermic peak was observed around 235 °C, indicating the reduction of Ni to its elemental state. This temperature is the minimum necessary to reduce the ink to metallic Ni. For this reason, 240 °C was chosen as the curing temperature for subsequent processing. It is important to clarify that the metal formation process of these inks is mechanistically very different from that of conventional nanoparticle conductive inks. The initial step of the curing of these inks is a chemical (reduction) process, rather than a

physical process (as is observed in particle based inks). As such, the curing temperature is chosen based upon careful analysis and characterization of the chemical reduction process of Ni upon heating.
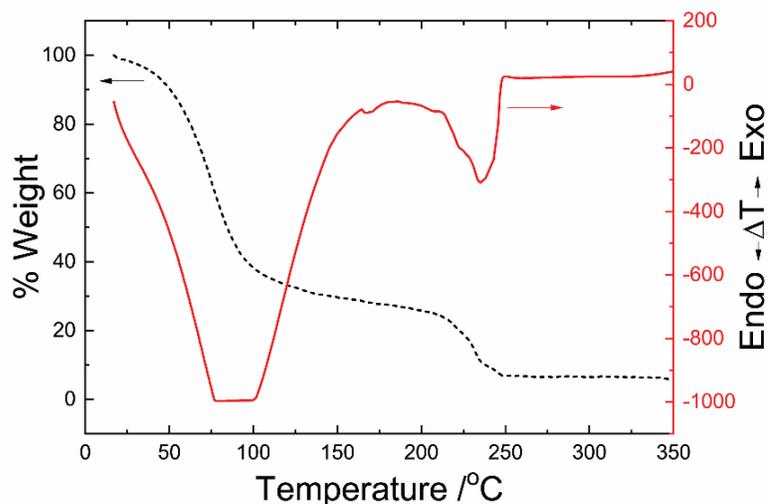
Figure 5-2: Thermogravimetric analysis (TGA) and differential thermal analysis (DTA) of the Ni MOD ink. Reproduced from [23] licensed under CC by 4.0

Surface morphology and elemental analysis of the sintered films were studied using a scanning electron microscope with energy-dispersive x-ray spectroscopy (EDS) (Jeol, JSM-IT100LA, USA). The EDS spectrum of reduced Ni ink (Figure 5-3) shows peaks for Ni at 0.851 keV and 7.471 keV. A small amount of carbon and oxygen was also detected in the EDS spectrum, which was either the byproduct of organic decomposition or contamination in the sintered sample.
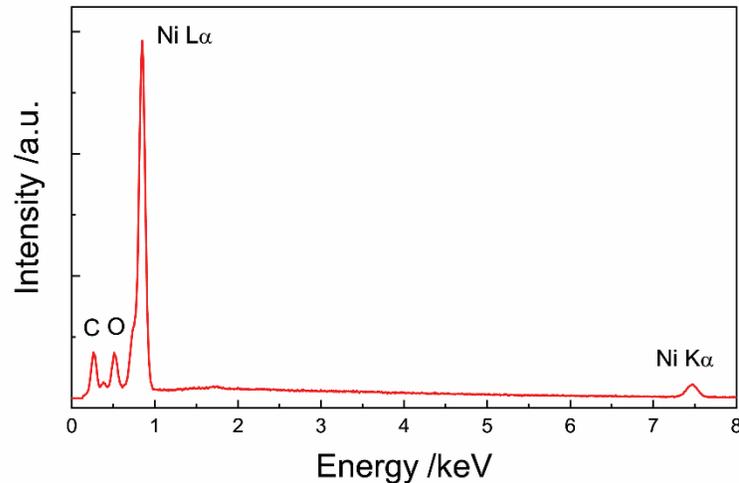
Figure 5-3: EDS spectrum of printed and sintered Ni MOD ink. Reproduced from [23] licensed under CC by 4.0

5.4. Aerosol printing

A Nanojet aerosol printer (Integrated Dispensing Solutions, Inc.) was used to dispense the Ni ink onto the substrate. Other printing processes like inkjet printing can also be used to deposit this ink [26]. The Nanojet printer uses ultrasonic energy to atomize the functional ink. A carrier gas delivers the aerosol to a series of aerodynamic focusing lenses that concentrate the aerosol as it exits the nozzle. The ultrasonic atomizer consists of a planar piezoelectric transducer having frequencies in the range of 1 to 2 MHz which is acoustically coupled with the ink. The atomizer produces a polydisperse distribution of droplets with a size distribution in the range of ~ 0.5 to 5 μm in diameter [27]. Air was used as a carrier gas to transport the aerosol to the focusing lenses. Ink passes through the focusing lens and into a tapered Luer lock dispensing tip. A sheath gas flow was used to avoid clogging of the nozzle and to focus the distribution of aerosol droplets onto the substrate. The sheath gas and aerosol flow rate were kept constant throughout the experiments to maintain consistency in the printed samples. The printer uses Aerotech PRO 165 mechanical-bearing linear stages to move the work table in the X and Y directions and an Aerotech PRO 115

mechanical-bearing linear stage to move the deposition head in the Z- axis direction. A solid 1 cm × 1 cm square pattern was printed using a 25-gauge dispensing tip. The distance between the substrate and nozzle tip was kept constant at 5 mm, and a translational speed of 2 mm/sec was used to print the samples. The thickness of the sintered films was measured using an optical profilometer (Nanovea ST400, USA) and a stylus profilometer (Tencor P2, USA). The printed pattern had a wet film thickness of ~ 4 μm and dried film thickness of ~ 1 μm for a single printed layer.

Glass slides were used as substrates and were cleaned with isopropyl alcohol before printing. To improve the wettability of the ink, the substrates were treated with atmospheric plasma (Surfx Atomflo, USA). Based on the results from the DTA discussed above, the final printed samples were cured at 240 ℃ for 15 minutes. Two different cases were explored to study the sintering behavior. In Case 1, the samples were sintered at 240 ℃ for 15 minutes in the absence of any magnetic field. In Case 2, the samples were sintered at 240 ℃ for 15 minutes in a homogeneous magnetic field of 250 Oe.

5.5. Results and discussion

After aerosol printing, each substrate with printed solid square pattern was heated on a benchtop hot plate. A location on a magnetic hotplate which had a homogenous magnetic field lines was chosen to reduce the sample. The cured Ni films were characterized by SEM imaging (Figure 5-4) to study morphology and the structure of the reduced Ni. The samples that were processed in the presence of a homogeneous magnetic field showed nanowires where the nanowire axis was aligned in the direction of the magnetic field. The SEM shows that each nanowire was composed of individual 100-250 nm nanoparticles that are fused together, resembling a "string of pearls". This suggests that the reduction forms nanoparticles, which are aligned in the presence of

the magnetic field, then sintered together at the processing temperature. The Ni particles follow the pattern of the magnetic field lines.
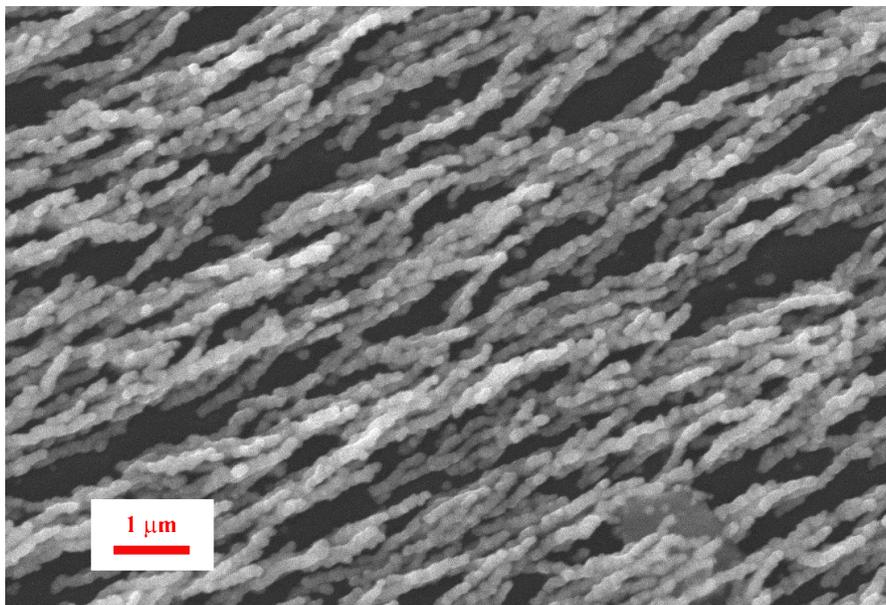
Figure 5-4: SEM image of aligned Ni nanowires (50 % dilution). Reproduced from [23] licensed under CC by 4.0

In the absence of a magnetic field, the particles are not aligned to form nanowires. Rather, the samples that were thermally processed in the absence of a magnetic field show the presence of a porous Ni film with particles ranging from 100 to 250 nm (Figure 5-5a). Significant necking between Ni particles was observed. The samples were cured after each printed layer. For printing of the second and third layers, the Ni ink was printed on top of the previously cured layer. In order to study the isotropy of the printed Ni, an extra case was investigated where a nanowire grid was printed by reducing the Ni in the presence of a magnetic field perpendicular to the previous layer (Figure 5-5c).

5.5.1. Alignment characterization

In order to quantitatively evaluate the orientation of reduced Ni nanowires, a method used by Ayres et al. [28] to measure the wire alignment in electrospun materials was adopted. A two dimensional (2D) Fast Fourier Transform (FFT) was used to measure the degree of alignment. Each image was cropped to 512x512 pixels and was saved as a grayscale image. ImageJ software supported by an oval profile plug-in was used to conduct the 2D-FFT analysis. The 2D-FFT function converts the spatial information in the image into a defined frequency domain. This frequency domain plots the rate at which pixel intensities change in the image and produces a frequency plot of grayscale pixels distributed in a pattern. The oval profile plug-in was then used to get the total pixel intensities for each radius. The total pixel intensities for each radius were used to generate the 2D FFT nanowire alignment plot. The peak shape and height determine the degree of alignment, while the peak position indicates the axis of orientation of the nanowires.
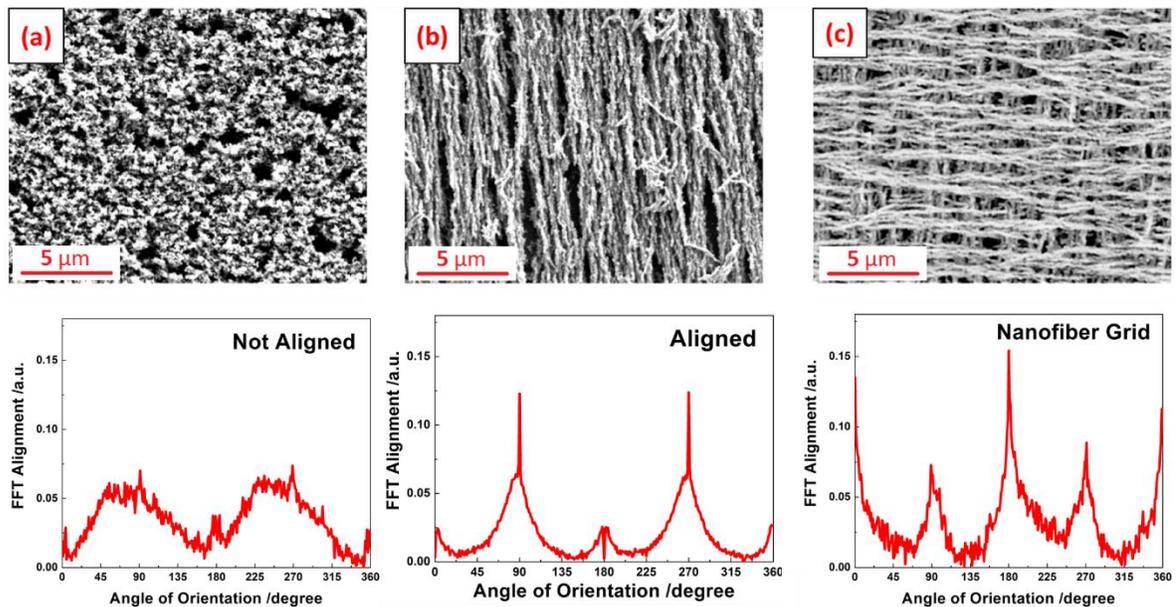

Figure 5-5: SEM images with corresponding 2D FFT alignment plots of two-nickel layers sintered in (a) no magnetic field, (b) homogeneous magnetic field of 250 Oe in the same direction for all layers, and (c)

The FFT alignment plot for Ni cured in the presence of magnetic field shows a fibrous structure with peaks at 90 and 270 degrees, while the Ni reduced in absence of magnetic field shows random particulate structure. The nanowire grid sample produced using alternating magnetic field orientations shows peaks at 0, 90, 180, 270 and 360 degrees. The intensities of the peaks at 0, 180 and 360 degrees were higher than that of 90 and 270 degrees because of the alignment of the top layer was more prominent in the SEM image than that of the bottom layer.

5.5.2. Electrical characterization

The electrical resistivity for the printed Ni ink was measured using a four-point probe (Jandel RM3000, UK). A significant difference in the electrical properties was observed for Ni cured in the presence of a magnetic field compared with that of Ni cured in the absence of a magnetic field. Figure 5-6 shows the resistivity values for the different cases. As expected, the resistivity decreased as the number of layers increased. The reason for the decrease was that the voids generated during the sintering of the previous layer were filled with additional Ni during the printing of subsequent layers. The electrical resistivity of the Ni cured in the presence of the magnetic field was lower (higher conductivity) than the Ni cured in the absence of a magnetic field. The resistivity was lower in the direction of the aligned Ni nanowires than perpendicular to the aligned Ni nanowires. For the nanowire grid samples produced using alternating magnetic field orientations, the resistivity was almost equal in both directions. The lowest resistivity of 560 $\mu\Omega\cdot$cm (80X bulk Ni) was observed in the nanowire grid samples, which is better than previously published studies [29, 30]. It should be noted that these nanowire arrays are not completely dense as there are spaces between nanowires. These resistivities are calculated assuming uniform

97

coverage of Ni with no pores, so they overestimate the actual resistivity based upon the amount of Ni actually present in the nanowires.
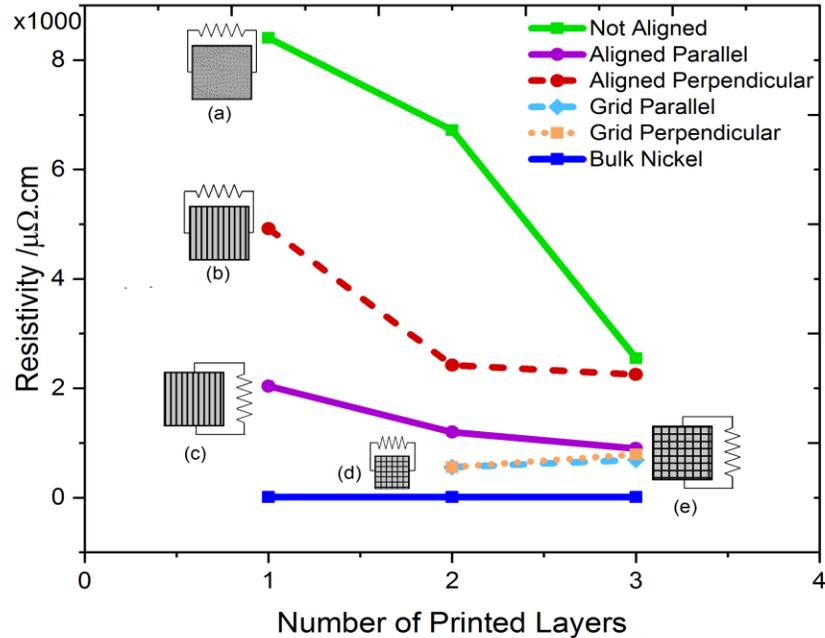
Figure 5-6: Electrical characterization of Ni for particles (a) not aligned, (b) & (c) aligned (nanowires) and (d) & (e) in grid orientation. Reproduced from [23] licensed under CC by 4.0

5.5.3. Magnetic characterization

Magnetic properties were studied by obtaining the hysteresis loops using a Princeton Applied Research (PAR 155) vibrating sample magnetometer (VSM) modified with Lakeshore Cryotronics 7300 electronics. The magnetic properties of two-layer Ni films reduced in the absence of a magnetic field (Figure 5-7a) and films reduced in the presence of a directional magnetic field (Figure 5-7b) were studied by measuring the hysteresis loops. The saturation magnetization for all samples was found to be 30 emu/g, which is comparable to the bulk Ni saturation magnetization [31]. Figure 5-7a shows hysteresis loops obtained in planar perpendicular directions where soft magnetic properties were observed with remanent magnetization (y intercept

of the loop) of 10 emu/g and coercive field (x intercept of the loop) of 120 Oe. By exposing the film to a directional magnetic field during the reduction process, a significant difference was obtained. The induced anisotropy parallel to the alignment direction showed a remanent magnetization of 20 emu/g, while the perpendicular direction shows a remanent magnetization of 7 emu/g. This is due to the obtained nanowire structure that has a shape anisotropy along the axis of the nanowire. By aligning the film layers in perpendicular directions to form a nanowire grid structure (Figure 5-7c), higher remanent magnetization than the unaligned film was obtained in the parallel and perpendicular directions due to the connected nanowire grid structure. These results show the possibility of tailoring the magnetic properties of the printed Ni films, which can be exploited for applications such as magnetic data storage or magnetoresistive sensors. The nanogrid structure on a wide range of substrates can also be explored for making skin attachable loudspeakers and microphones [32].
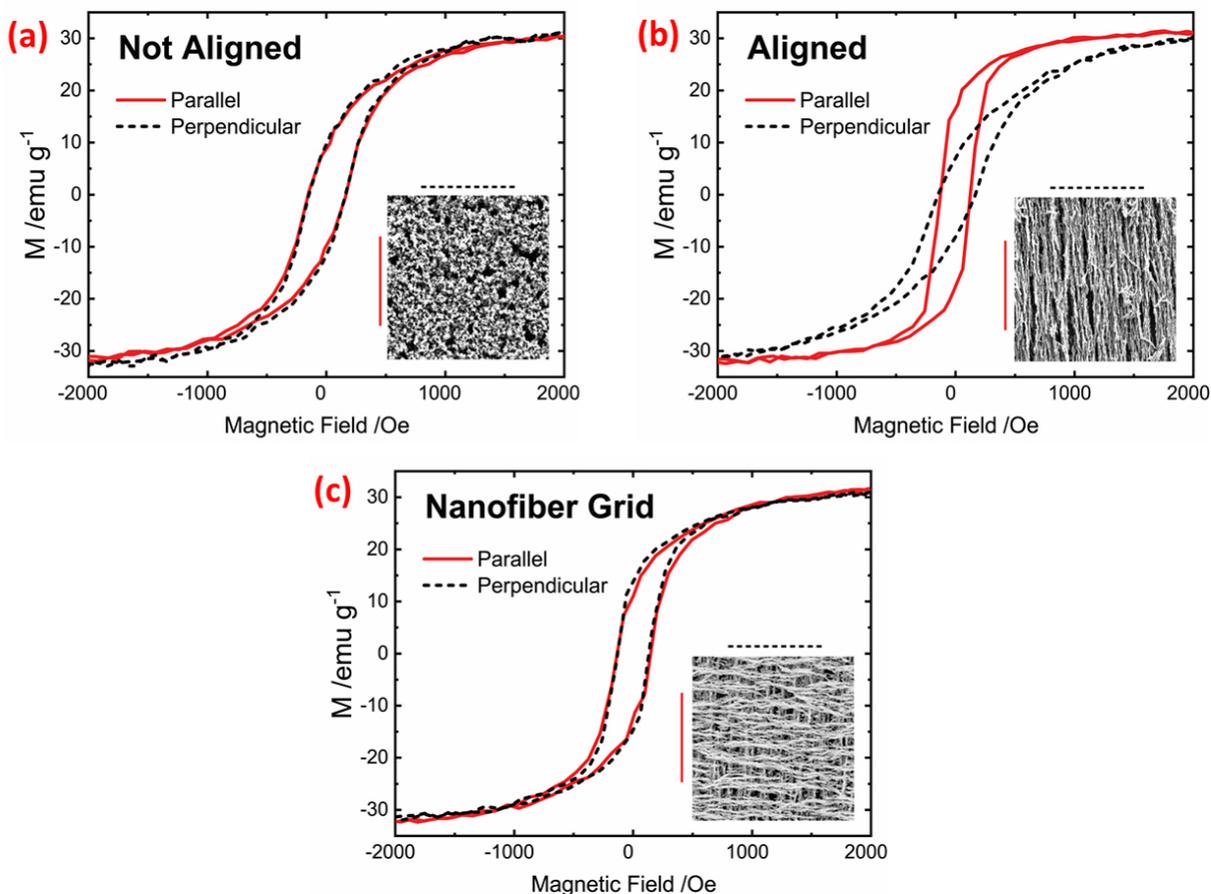
Figure 5-7: Magnetic characterization of Ni film with nanoparticles (a) not aligned, (b) aligned nanowires) and in (c) grid orientation. Reproduced from [23] licensed under CC by 4.0

To demonstrate the feasibility of printing on a flexible substrate, three layers of nickel MOD ink with fine traces were printed on Kapton® film using the Nanojet aerosol printer (Figure 5-8). The pattern was sintered on a hot plate at 240 °C for 15 minutes. A thickness of ~ 4 μm was obtained after thermal processing. This Ni MOD ink shows potential for applications such as antenna [33] and magnetic sensors [18] where the substrate flexibility is important.
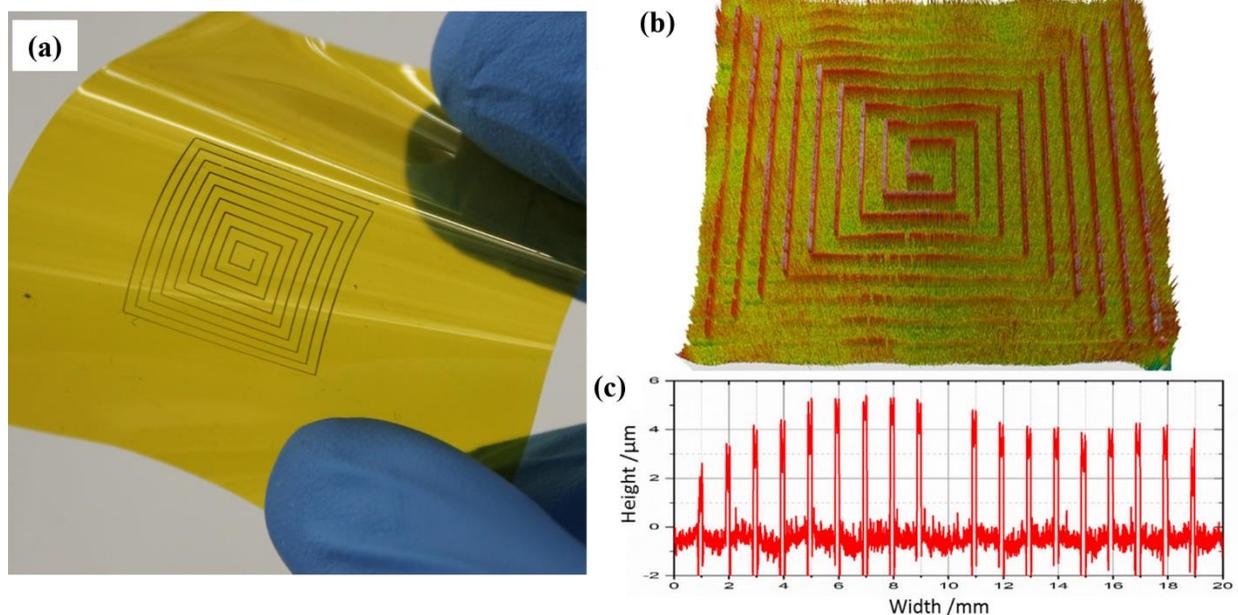
Figure 5-8: (a) Aerosol print of nickel with a square coil pattern on Kapton thin film. (b) Optical profile of printed structure (c) Cross sectional profile of printed structure

5.6. Summary

A novel template free method of producing aligned Ni nanowires in ambient conditions from a homogeneous solution was presented in this chapter. This was one of the few examples of printing ferromagnetic precursor inks. The ink can be printed using a variety of processes on different substrates, including flexible and thermally sensitive materials for applications such as antennas, magnetic sensors and optical polarizers. Aerosol printing of the ink on glass and Kapton® substrates were demonstrated in this study. Inks with different rheological properties can also be easily developed for other functional printing techniques such as flexography, screen-printing, and inkjet printing. Thermal reduction of the precursor ink in the presence of a weak magnetic field produced large areas of pure aligned Ni nanowires, requiring no further processing, which have enhanced anisotropic electrical and magnetic properties. This was the first example of

thermally induced nanowire formation on a substrate. The film structure and morphology can be easily manipulated, enabling the production of a variety of novel patterned structures having unique electronic and magnetic properties, as well as commercial applications. The lowest electrical resistivity (highest conductivity) was observed for nanowire grids.

5.7. References

[1]   J. Abu-Khalaf, L. Al-Ghussain, and A. a. Al-Halhouli, "Fabrication of Stretchable Circuits on Polydimethylsiloxane (PDMS) Pre-Stretched Substrates by Inkjet Printing Silver Nanoparticles," *Materials,* vol. 11, no. 12, p. 2377, 2018.

[2]   Q. Huang, K. N. Al-Milaji, and H. Zhao, "Inkjet printing of silver nanowires for stretchable heaters," *ACS Applied Nano Materials,* vol. 1, no. 9, pp. 4528-4536, 2018.

[3]   H. Niu, Q. Chen, M. Ning, Y. Jia, and X. Wang, "Synthesis and one-dimensional self-assembly of acicular nickel nanocrystallites under magnetic fields," *The Journal of Physical Chemistry B,* vol. 108, no. 13, pp. 3996-3999, 2004.

[4]   J. Everhart, *Engineering properties of nickel and nickel alloys*. Springer Science & Business Media, 2012.

[5]   M. ZHANG, D. Jia, M. ZHANG, and L. Wei, "Shape-controlled synthesis of nickel wires using an external magnetic field," *Chinese Journal of Catalysis,* vol. 30, no. 5, pp. 447-452, 2009.

[6]   J. Ye, Q. Chen, and Y. Zheng, "Magnetic properties of nickel film formed under magnetic fields," *Journal of Physics D: Applied Physics,* vol. 41, no. 20, p. 205011, 2008.

[7]   H. Wang, M. Li, X. Li, K. Xie, and L. Liao, "Preparation and thermal stability of nickel nanowires via self-assembly process under magnetic field," *Bulletin of Materials Science,* vol. 38, no. 5, pp. 1285-1289, 2015.

[8]   L. Sun, Q. Chen, Y. Tang, and Y. Xiong, "Formation of one-dimensional nickel wires by chemical reduction of nickel ions under magnetic fields," *Chemical Communications,* no. 27, pp. 2844-2846, 2007.

[9]   C. Gong, J. Tian, T. Zhao, Z. Wu, and Z. Zhang, "Formation of Ni chains induced by self-generated magnetic field," *Materials Research Bulletin,* vol. 44, no. 1, pp. 35-40, 2009.

[10]   T. Narayanan, M. Shaijumon, L. Ci, P. Ajayan, and M. Anantharaman, "On the growth mechanism of nickel and cobalt nanowires and comparison of their magnetic properties," *Nano Research,* vol. 1, no. 6, pp. 465-473, 2008.

[11]   G. Sauer *et al.*, "Surface-enhanced Raman spectroscopy employing monodisperse nickel nanowire arrays," *Applied physics letters,* vol. 88, no. 2, p. 023106, 2006.

[12]   K. Krishnadas, P. Sajanlal, and T. Pradeep, "Pristine and hybrid nickel nanowires: Template-, magnetic field-, and surfactant-free wet chemical synthesis and Raman studies," *The Journal of Physical Chemistry C,* vol. 115, no. 11, pp. 4483-4490, 2011.

[13]   Z. Wang *et al.*, "Spin-wave quantization in ferromagnetic nickel nanowires," *Physical review letters,* vol. 89, no. 2, p. 027201, 2002.

[14]   P. Grundy, "Thin film magnetic recording media," *Journal of Physics D: Applied Physics,* vol. 31, no. 21, p. 2975, 1998.

[15]   M. Melzer *et al.*, "Imperceptible magnetoelectronics," *Nature communications,* vol. 6, p. 6080, 2015.

[16]   Y. f. Chen *et al.*, "Towards Flexible Magnetoelectronics: Buffer-Enhanced and Mechanically Tunable GMR of Co/Cu Multilayers on Plastic Substrates," *Advanced Materials,* vol. 20, no. 17, pp. 3224-3228, 2008.

[17]   I. Mönch *et al.*, "Rolled-up magnetic sensor: nanomembrane architecture for in-flow detection of magnetic objects," *ACS nano,* vol. 5, no. 9, pp. 7436-7442, 2011.

[18]   K. Liu, K. Nagodawithana, P. Searson, and C. Chien, "Perpendicular giant magnetoresistance of multilayered Co/Cu nanowires," *Physical Review B,* vol. 51, no. 11, p. 7381, 1995.

[19]   W. Kang, J. Chu, X. Zeng, and Y. Fan, "Large-area flexible infrared nanowire grid polarizer fabricated using nanoimprint lithography," *Applied Optics,* vol. 57, no. 18, pp. 5230-5234, 2018.

[20]   J. J. Wang *et al.*, "High-performance nanowire-grid polarizers," *Optics letters,* vol. 30, no. 2, pp. 195-197, 2005.

[21]   D. Karnaushenko, D. D. Karnaushenko, D. Makarov, S. Baunack, R. Schäfer, and O. G. Schmidt, "Self-Assembled On-Chip-Integrated Giant Magneto-Impedance Sensorics," *Advanced Materials,* vol. 27, no. 42, pp. 6582-6589, 2015.

[22]   F. Johansson, M. Jonsson, K. Alm, and M. J. E. c. r. Kanje, "Cell guidance by magnetic nanowires," *Experimental Cell Research,* vol. 316, no. 5, pp. 688-694, 2010.

[23]   C. G. Mahajan *et al.*, "Magnetic Field Patterning of Nickel Nanowire Film Realized by Printed Precursor Inks," *Materials,* vol. 12, no. 6, p. 928, 2019.

[24]   Y. Farraj, M. Grouchko, and S. Magdassi, "Self-reduction of a copper complex MOD ink for inkjet printing conductive patterns on plastics," *Chemical Communications,* vol. 51, no. 9, pp. 1587-1590, 2015.

[25]   P. G. Fox, J. Ehretsmann, and C. E. Brown, "Development of internal structure during thermal decomposition: nickel formate dihydrate," *J. Catal.,* 10.1016/0021-9517(71)90007-8 vol. 20, no. 1, pp. 67-73, // 1971, doi: 10.1016/0021-9517(71)90007-8.

[26]   K. R. Zope, D. Cormier, and S. Williams, "Reactive Silver Oxalate Ink Composition with Enhanced Curing Conditions for Flexible Substrates," *ACS applied materials & interfaces,* 2018.

[27]   M. Essien, "Apparatuses and Methods for Stable Aerosol Deposition Using an Aerodynamic Lens System," ed: Google Patents, 2016.

[28]   C. E. Ayres *et al.*, "Measuring fiber alignment in electrospun scaffolds: a user's guide to the 2D fast Fourier transform approach," *Journal of Biomaterials Science, Polymer Edition,* vol. 19, no. 5, pp. 603-621, 2008.

[29]   D. Li, D. Sutton, A. Burgess, D. Graham, and P. D. Calvert, "Conductive copper and nickel lines via reactive inkjet printing," *Journal of Materials Chemistry,* vol. 19, no. 22, pp. 3719-3724, 2009.

[30]   D. I. Petukhov, M. N. Kirikova, A. A. Bessonov, and M. J. Bailey, "Nickel and copper conductive patterns fabricated by reactive inkjet printing combined with electroless plating," *Materials Letters,* vol. 132, pp. 302-306, 2014.

[31]   J. Crangle and G. Goodman, "The magnetization of pure iron and nickel," *Proc. R. Soc. Lond. A,* vol. 321, no. 1547, pp. 477-491, 1971.

[32]   S. Kang *et al.*, "Transparent and conductive nanomembranes with orthogonal silver nanowire arrays for skin-attachable loudspeakers and microphones," *Science advances,* vol. 4, no. 8, p. eaas8772, 2018.

[33]   V. Kyovtorov, I. Georgiev, S. Margenov, D. Stoychev, F. Oliveri, and D. Tarchi, "New antenna design approach–3D polymer printing and metallization. experimental test at 14–18 GHz," *AEU-International Journal of Electronics and Communications,* vol. 73, pp. 119-128, 2017.

Chapter 6 Summary and Recommendations for Future Work

6.1. Summary

In this chapter, an overall summary of the research work is presented with key contributions of the research. The main objective of this research was to present a new approach to form an alloy film by *ex-situ* mixing individual metal inks in desired proportions. Since the properties of alloys change with the elemental composition, a printing process which could digitally dispense alloy ink having specific desired compositions would enable different functionalities and be highly desirable. A wide range of digital printing techniques and different types of metal inks used with those techniques were presented in Chapter 2. Most of the printing processes use premixed alloy ink or nanoalloy particles of known composition. The current printing processes are not capable of printing different alloy composition within the printed part. Inkjet printing process shows potential of dispensing more than one ink at a time with huge arrays of nozzles to reduce the printing time.

Copper and nickel MOD precursor inks were formulated having rheological properties suitable for inkjet printing technique. The inks were characterized using thermal analysis, mass spectrometry and infrared spectroscopy. Sintering of metal and alloy inks were studied under various conditions. Nickel, a ferromagnetic metal, shows novel microstructures when sintered in the presence of a magnetic field. A template free method of producing aligned Ni nanowires with enhanced electrical and magnetic properties along the alignment was presented.

The reduced metal and alloy structures were characterized using energy-dispersive x-ray spectroscopy (EDS), transmission electron microscopy (TEM), and x-ray diffraction (XRD). The reduction of combined ink solutions (copper and nickel) at low temperature show formation of a

two phased structure having copper as one phase and a nickel rich alloy as other phase. Such nanoalloy structure showed strong resistance to oxidative environment demonstrating numerous potential applications in printed electronics.

To achieve homogeneous alloy formation, the diffusion of the copper into nickel rich alloy at high temperature was presented. The solid printed alloy film was unstable and agglomerated at high temperature to form small islands onto the substrate. To minimize the agglomeration at high temperatures, the reduced alloy ink was compressed onto a quartz plate to form a dense thick film. After sintering at high temperature, a solid alloy film with minimal agglomeration was obtained. The XRD on the final film confirmed one single phase of copper nickel alloy with elemental ratio of $Cu_{46}Ni_{54}$.

6.2. Key contributions

The following presents a summary of the contributions identified from this research:

- The reduction process of copper and nickel MOD precursor inks was studied in detail. The inks were characterized using thermal analysis, mass spectrometry, and infrared spectroscopy. The thermal events analyzed during the reduction of inks helped understand the decomposition of metal complex along with the nucleation and growth process of the reduced nanoparticles.

- A new method to easily form copper-nickel nanoalloy directly onto a substrate was presented. The nanoalloy film had copper on the substrate encapsulated with nickel rich nanoalloy. The film demonstrated no change in resistivity values on exposure to oxygen plasma treatment making it suitable for conductive applications in oxidizing environments.

- The findings from this research confirmed the formation of desired alloy composition for a model CuNi system by printing individual elemental inks in known proportions. High temperature diffusion process was presented to achieve homogeneous CuNi alloy formation within a printed part. A printing workflow was proposed to fabricate a 3D part with desired alloy composition.

- A novel method to produce template free aligned nickel nanowires in ambient conditions directly onto a substrate was presented. This is one of the few examples of printing a ferromagnetic MOD precursor ink. The film structure and morphology can be easily manipulated to produce structures having unique electrical, magnetic, and optical properties.

6.3. Recommendations for future research

The work presented in this dissertation focused on forming an alloy film with a known elemental ratio by using individual copper and nickel MOD precursor inks. Some possible directions for future research are presented below.

This research confirms the formation of desired alloy composition for a model Cu-Ni system within a layer by printing individual elemental inks in desired proportions. The next step would be to print multiple layers in order to get a macroscopic part. A Xerox® M4 Industrial inkjet print head could be used to dispense individual elemental inks. The print head can dispense up to four materials with a drop volume of 15-30 pl onto the substrate. Different print conditions such as drop spacing, time delayed depositions and waveform optimization could be studied and optimized for each elemental ink. Since solid state dewetting is an issue to achieve diffusion at high temperatures, each printed layer could be reduced to its elemental state at lower temperatures.

Once the part is printed to a desired thickness, high temperature diffusion can be achieved with minimal dewetting.

The ink formulation could be improved to increase the solid content in the final reduced film. Increasing the solid content would increase the final film thickness of each printed layers. This will also help in reducing the print time as well as minimize the solid state dewetting phenomenon. A mixture of nano/micro metal particles with MOD precursor ink could be used to increase the metal loading. During the reduction process, the particles provide nucleation sites for the metal complex. The surface morphology obtained with such inks after sintering has minimal cracks and pores [1].

MOD precursor inks of Au and Ag have been formulated in the literature. The formation of nanoalloy by mixing these inks with Cu or Ni can be studied. As mentioned in Chapter 1, wide range of nanoalloys such as FePt, CoPt, and CuAg have been synthesized using the bottom up approach. The metal precursors used in literature could be to create a MOD precursor ink with rheological properties to suit inkjet printing technique. Other elemental inks such as Co, Fe, Pt, and Ti could be formulated which are often used to create a wide range of alloy families. Different properties of these inks can be explored which can serve as a great tool to print and sinter individual metal ink for other functional applications.

Formation of an alloy film using photonic sintering systems (Novacentrix Pulseforge) will be useful in fabricating functional devices on temperature sensitive substrates. The main advantage of using photonic sintering method is that the sintering process can be carried out at room temperature at very high speed. A two-step photonic sintering process has been reported in the literature to improve quality of the printed pattern and minimize damages to the substrate [2, 3].

The two steps consist of a preheating step of low energy pulses to dry and preheat the sample followed by the main sintering step of high energy to achieve reduction and complete necking between the particles. Since the Pulseforge uses a flash lamp to achieve high temperatures in a short amount of time, the process of dewetting could be studied with this tool. The pulse shaping feature in the photonic sintering tool can also be explored to combine the reduction and diffusion processes. In pulse shaping, a custom sintering profile can be designed with pulses having different durations and amplitudes. Farraj *et al.* [4] analyzed the drying process on a copper precursor ink before the main sintering process. It was observed that the excessive drying of the ink causes crystallization of the copper complex which led to the formation of many islands upon sintering. Therefore, optimization of overall sintering energy is important to reduce the formation of crystallization during the drying stage and induce decomposition of the metal complexes in the main sintering stage. SimPulse® software can be used to simulate these pulses to achieve the desired temperatures to achieve decomposition of the metal complex and diffusion to minimize the island formation in the sintered sample.

The MOD precursor inks can be used as a binder to 3D print metal or alloy parts using binder jetting additive manufacturing technique. In a metal binder jet printing technique, a liquid polymer binding agent is selectively inkjet printed into a layer of metal powder bed. Once a layer is printed, it is dried and a new layer of powder is spread on top of the previous layer. The layer by layer process is repeated to create a 3D part. The printed part is removed from the unbound loose powder in the bed. To achieve necking between the particles, the printed 3D part is placed in a furnace at high temperatures. Copper MOD precursor ink has been used as a binder on a copper powder bed to print a 3D part [5]. By dispensing a known volume of metal ink into the powder bed and reducing it to its elemental state at low temperatures, the alloy composition can be

110

controlled in each layer. The final printed part can later be placed in a vacuum furnace to achieve diffusion and necking between the particles.

6.4. References

[1]   W. Li, S. Cong, J. Jiu, S. Nagao, and K. Suganuma, "Self-reducible copper inks composed of copper–amino complexes and preset submicron copper seeds for thick conductive patterns on a flexible substrate," *Journal of Materials Chemistry C,* vol. 4, no. 37, pp. 8802-8809, 2016.

[2]   S.-H. Park, S. Jang, D.-J. Lee, J. Oh, and H.-S. Kim, "Two-step flash light sintering process for crack-free inkjet-printed Ag films," *Journal of Micromechanics and Microengineering,* vol. 23, no. 1, p. 015013, 2012.

[3]   E.-B. Jeon, S.-J. Joo, H. Ahn, and H.-S. Kim, "Two-step flash light sintering process for enhanced adhesion between copper complex ion/silane ink and a flexible substrate," *Thin Solid Films,* vol. 603, pp. 382-390, 2016.

[4]   Y. Farraj, A. Smooha, A. Kamyshny, and S. Magdassi, "Plasma-Induced Decomposition of Copper Complex Ink for the Formation of Highly Conductive Copper Tracks on Heat-Sensitive Substrates," *ACS Applied Materials & Interfaces,* vol. 9, no. 10, pp. 8766-8773, 2017.

[5]   Y. Bai and C. B. Williams, "Binder jetting additive manufacturing with a particle-free metal ink as a binder precursor," *Materials & Design,* vol. 147, pp. 146-156, 2018.

Appendix - A

Lattice parameter calculations

To calculate the experimental lattice parameter values, the wavelength for Cu (Kα1) radiation was taken as λ= 1.540562 Å. The Cu (Kα) radiation used to record the diffraction peaks has two wavelength components Kα1 and Kα2 which overlap heavily at low angles [1]. The intensity of Kα1 is approximately twice that of Kα2. Therefore, spearing out the $K\alpha_1$ component from the diffraction peaks using peak decomposition Pearson type VII [2] function gives a more accurate 2θ value of the peak. The calculated lattice parameter was then extrapolated against $\cos^2\theta/\sin\theta$ to get the precise lattice parameter for the sample [3].

Copper MOD ink

Table A- 1: X-ray diffraction peak values and corresponding lattice parameter values for reduced copper

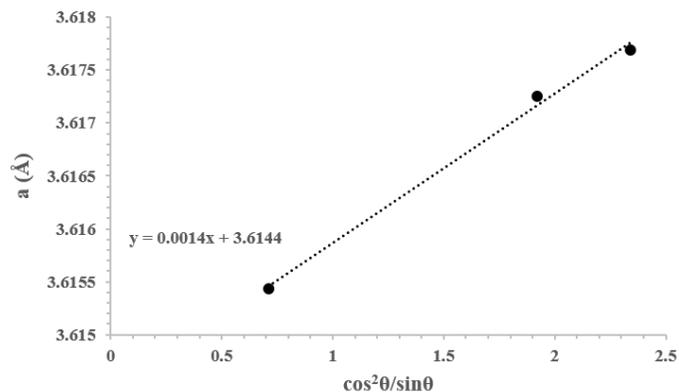| $2\theta_{peak}$ (deg)	θ_{peak} (rad)	d (Å)	hkl	$\cos^2\theta/\sin\theta$	a (Å)
43.282	0.37771	2.08868	111	2.34	3.61769
50.414	0.43995	1.80863	200	1.92	3.61725
89.921	0.78471	1.09009	311	0.71	3.61543

Figure A- 1: Precise lattice parameter determination for reduced copper

The equation y = 0.0014x + 3.6144 at x = 0 gives the lattice parameter value for reduced copper as 3.6144 Å.

Nickel MOD ink

Table A- 2: X-ray diffraction peak values and corresponding lattice parameter values for reduced nickel

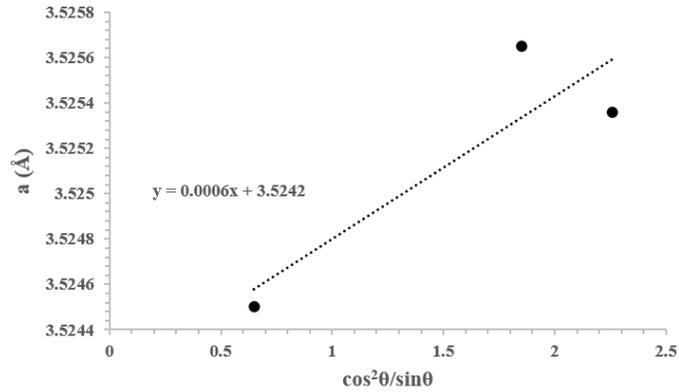| $2\theta_{peak}$ (deg)	θ_{peak} (rad)	d (Å)	hkl	$\cos^2\theta/\sin\theta$	a (Å)
44.475	0.38812	2.03536	111	2.26	3.52536
51.820	0.45221	1.76283	200	1.85	3.52565
92.913	0.81082	1.06268	311	0.65	3.52450

Figure A- 2: Precise lattice parameter determination for reduced nickel

The equation y = 0.0006x + 3.5242 at x = 0 gives the lattice parameter value for reduced nickel as 3.5242 Å.

CuNi MOD ink sintered at 230 °C

Table A- 3: X-ray diffraction peak values and corresponding lattice parameter values for CuNi MOD ink reduced at 230 °C

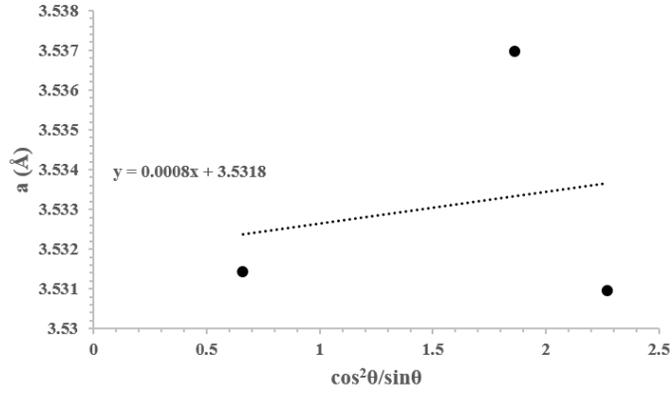| $2\theta_{peak}$ (deg)	θ_{peak} (rad)	d (Å)	hkl	$\cos^2\theta/\sin\theta$	a (Å)
44.401	0.38747	2.03859	111	2.27	3.53095
51.642	0.45066	1.76849	200	1.86	3.53698
92.676	0.80875	1.06477	311	0.66	3.53144

Figure A- 3: Precise lattice parameter determination for CuNi MOD ink reduced at 230 °C

The equation $y = 0.0008x + 3.5318$ at $x = 0$ gives the lattice parameter value for reduced copper nickel alloy as 3.5318 Å. Vegard's law was used to determine the alloy composition using the values obtained from the lattice parameter. The lattice parameter of a binary alloy is a linear function of lattice parameters of the two elements present and is given by [4]

$$x = \frac{a_{alloy} - a_{Ni}}{a_{Cu} - a_{Ni}} \qquad \text{Eq. A1}$$

Where 'x' is the mole fraction of the Cu phase in the alloy. The lattice parameters for copper and nickel was 3.6144 Å and 3.5242 Å. Substituting these value in Eq. A1

$$x = \frac{3.5318 - 3.5242}{3.6144 - 3.5242} = 0.08$$

Therefore, the elemental composition of the alloy phase was Cu_8Ni_{92}.

$Cu_{30}Ni_{70}$ MOD ink sintered at 800 °C

Table A- 4: X-ray diffraction peak values and corresponding lattice parameter values for $Cu_{30}Ni_{70}$ MOD ink sintered at 800 °C

$2\theta_{peak}$ (deg)	θ_{peak} (rad)	d (Å)	hkl	$\cos^2\theta/\sin\theta$	a (Å)
44.158	0.38535	2.04924	111	2.28	3.54939
51.403	0.44857	1.77613	200	1.87	3.55226
75.586	0.65961	1.25695	220	1.01	3.55521

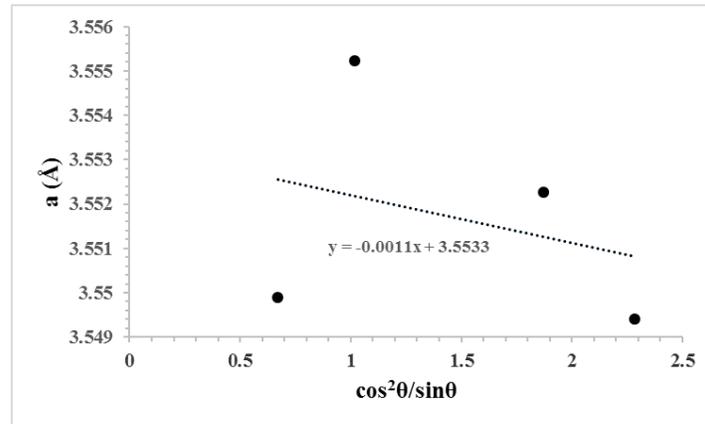| 92.053 | 0.80331 | 1.07033 | 311 | 0.66 | 3.54990 |

Figure A- 4: Precise lattice parameter determination for $Cu_{30}Ni_{70}$ MOD ink sintered at 800 °C

The equation y = -0.0011x + 3.5533 at x = 0 gives the lattice parameter value for reduced

copper nickel alloy as 3.5533 Å. Substituting the lattice parameter value in Eq. A1,

$$x = \frac{3.5533 - 3.5242}{3.6144 - 3.5242} = 0.32$$

The elemental composition of the alloy phase was $Cu_{32}Ni_{68}$.

$Cu_{50}Ni_{50}$ MOD ink sintered at 800 °C

Table A- 5: X-ray diffraction peak values and corresponding lattice parameter values for $Cu_{50}Ni_{50}$ MOD ink sintered at 800 °C

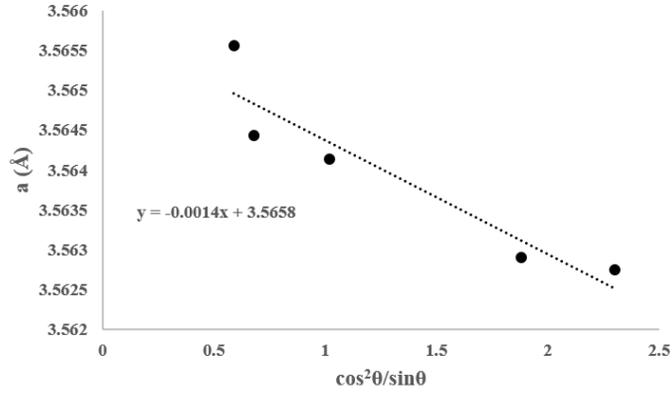| $2\theta_{peak}$ (deg)	θ_{peak} (rad)	d (Å)	hkl	$\cos^2 \theta/\sin \theta$	a (Å)
43.984	0.38383	2.05696	111	2.30	3.56275
51.239	0.44714	1.78145	200	1.88	3.56290
75.364	0.65768	1.26011	220	1.02	3.56413
91.570	0.79910	1.07472	311	0.68	3.56443
96.898	0.84559	1.02929	222	0.59	3.56556

Figure A- 5: Precise lattice parameter determination for Cu₅₀Ni₅₀ MOD ink sintered at 800 °C

The equation y = -0.0014x + 3.5658 at x = 0 gives the lattice parameter value for reduced

copper nickel alloy as 3.5658 Å. Substituting the lattice parameter value in Eq. A1,

$$x = \frac{3.5658 - 3.5242}{3.6144 - 3.5242} = 0.46$$

The elemental composition of the alloy phase was $Cu_{46}Ni_{54}$.

Cu₇₀Ni₃₀ MOD ink sintered at 800 °C

Table A- 6: X-ray diffraction peak values and corresponding lattice parameter values for Cu₇₀Ni₃₀ MOD ink sintered at 800 °C

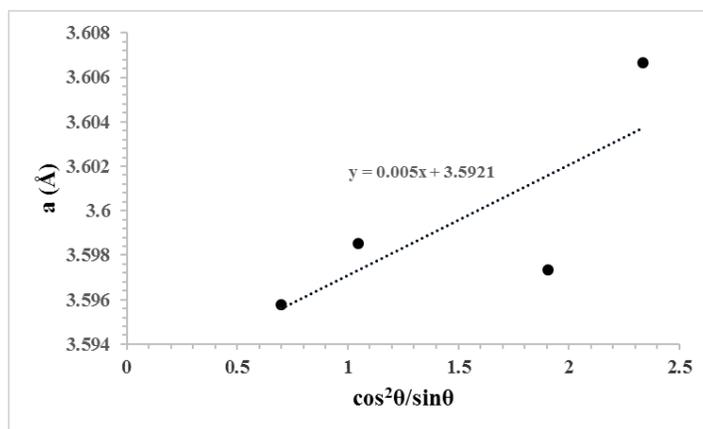| $2\theta_{peak}$ (deg)	θ_{peak} (rad)	d (Å)	hkl	$\cos^2\theta/\sin\theta$	a (Å)
43.421	0.37892	2.08229	111	2.33	3.60663
50.713	0.44255	1.79866	200	1.90	3.59733
74.520	0.65031	1.27226	220	1.04	3.59852
90.548	0.79018	1.08416	311	0.69	3.59576

Figure A- 6: Precise lattice parameter determination for Cu₇₀Ni₃₀ MOD ink sintered at 800 °C

The equation $y = 0.005x + 3.5921$ at $x = 0$ gives the lattice parameter value for reduced copper nickel alloy as 3.5921 Å. Substituting the lattice parameter value in Eq. A1,

$$x = \frac{3.5921 - 3.5242}{3.6144 - 3.5242} = 0.75$$

The elemental composition of the alloy phase was $Cu_{75}Ni_{25}$.

References

[1]   A. C. Fischer-Cripps, *The materials physics companion*. CRC Press, 2014.

[2]   S. Gupta, "Peak decomposition using Pearson type VII function," *Journal of applied crystallography,* vol. 31, no. 3, pp. 474-476, 1998.

[3]   B. D. Cullity, "Elements of X-ray Diffraction," 1978.

[4]   R. J. Tilley and R. Tilley, *Understanding solids: the science of materials*. Wiley Online Library, 2004.

Appendix – B

Transmission electron microscopy (TEM) (Jeol 2010, USA) was used at 200 kV to obtain the selected area electron diffraction (SAED) pattern for the sintered alloy film. Figure B- 1 (a) shows the TEM image of drop casted CuNi film sintered at 2 °C /min in a vacuum furnace. The film was removed from the substrate and placed on the TEM grid for analysis. The nanoparticles and grain boundaries are easily seen. Figure B- 1 (b) shows the electron diffraction pattern obtained from the same area shown in Figure B- 1 (a). The d spacing from electron diffraction data was used to calculate the lattice parameter and then was averaged over all four lattice constants. The lattice parameter obtained from the TEM analysis were not consistent with either a pure copper or pure nickel phase, indicating an alloy formation. Other unresolved ring patterns may be due to impurities, amorphous materials, or formation of small amounts of metal oxides (NiO, CuO or NiCuO).
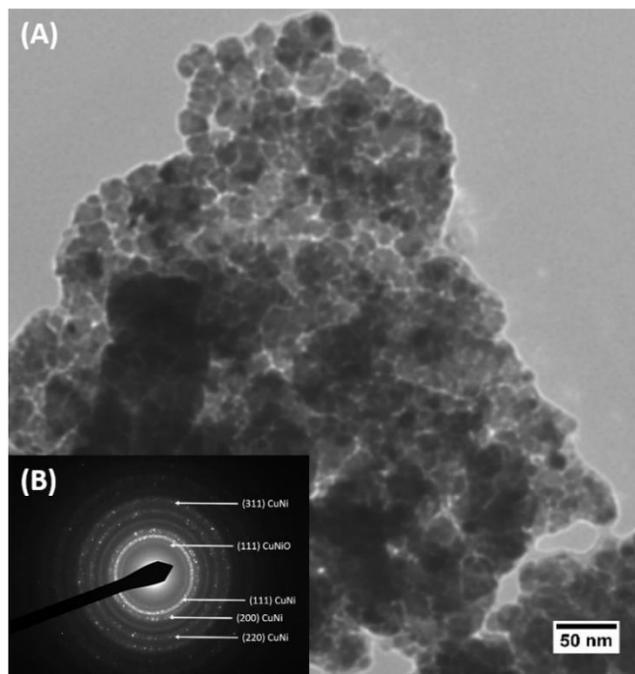

Figure B- 1: (a) TEM micrograph and (b) electron diffraction pattern of the alloy film